Preparation, Spectroscopy, and Lasing Performance of Cr^{2+}:ZnSe

by

Umit Demirbas

A Thesis Submitted to the
Graduate School of Sciences and Engineering
in Partial Fulfillment of the Requirements for
the Degree of

Master of Science

in

Materials Science and Engineering

Koç University

June 2006

Koç University

Graduate School of Sciences and Engineering

This is to certify that I have examined this copy of a master's thesis by

Umit Demirbas

and have found that it is complete and satisfactory in all respects,
and that any and all revisions required by the final
examining committee have been made.

Committee Members:

_____

Alphan Sennaroğlu, Ph. D. (Advisor)

_____

Mehmet Somer, Ph. D.

_____

Alper Kiraz, Ph. D.

Date: _____

ABSTRACT

This thesis provides a detailed description of the preparation, characterization and laser performance of diffusion-doped polycrystalline Cr^{2+}:ZnSe. Cr^{2+}:ZnSe lasers operate between 1880 and 3100 nm, above the tuning range of already existing tunable solid-state media such as Co^{2+}:MgF_2 and Tm^{3+}:YLF, and have important potential applications in vibrational spectroscopy, trace gas detection, medicine and optical excitation of mid-infrared lasers and optical parametric oscillators.

In the initial experiments, using thermal diffusion doping, thirty-three polycrystalline Cr^{2+}:ZnSe samples with fairly good spatial uniformity were prepared. By varying the diffusion time and/or the diffusion temperature, Cr^{2+}:ZnSe samples with different chromium concentration were obtained. A 3-dimensional analytical diffusion model was further developed to determine the diffusion coefficient D from absorption data between 800 and 1100 °C.

In the second set of experiments, we investigated the spectroscopic properties of the Cr^{2+}:ZnSe samples. Absorption measurements of samples showed that passive losses of the samples increase linearly with increasing chromium concentration. Due to concentration quenching fluorescence lifetime and fluorescence efficiency of the Cr^{2+}:ZnSe samples were also observed to decrease with concentration.

In gain-switched laser experiments, we used the 1570-nm output of a home-built KTP optical parametric oscillator as the pump source. Using intracavity configuration, record tuning range between 1880 and 3100 nm was demonstrated, with output energies as high as 145 μJ. In continuous-wave lasing experiments, 1800-nm output of a commercial Tm-fiber laser was used as the pump source. As high as 640 mW of output power was obtained and broad tunability between 2240 and 2900 nm was demonstrated. The optimum chromium concentration for lasing was determined from laser power measurements and the results were in good agreement with the value predicted from the fluorescence efficiency experiments.

ÖZET

Bu tez ısıl difüzyon yöntemiyle hazırlanmış Cr^{2+}:ZnSe malzemesinin hazırlanışı, spektroskopik karakterizasyonu ve laser performansının incelenmesi üzerine yapılmış ayrıntılı çalışmaları içermektedir. 1880-3100 nm dalgaboyu aralığında çalıştırılabilen Cr^{2+}:ZnSe laserleri, şu anda mevcut olan Co^{2+}:MgF_2 ve Tm^{3+}:YLF gibi laser malzemelerinden daha uzun dalgaboylarında çalışabilmekte, ve titreşim spektroskopisi ile diğer orta kızılaltı laser malzemeleri veya optik salınıcıların pompalanmasında kullanılmaktadır. İlk aşamada, ısıl difüzyon yöntemiyle krom malzemesinin oldukça homojen dağıldığı otuz üç Cr^{2+}:ZnSe örneği hazırlandı. Farklı difüzyon süreleri ve/veya difüzyon sıcaklıkları kullanılarak, değişik miktarlarda krom içeren örnekler elde edildi. Geliştirilen 3 boyutlu analitik model kullanılarak, difüzyon katsayısının 800-1100 °C aralığında değişimi incelendi. Daha sonraki deneylerde hazırlanan Cr^{2+}:ZnSe örneklerinin spektroskopik özellikleri incelendi. Yapılan optik soğurma ölçümleri, hazırlanan örneklerdeki pasif optik kayıplarının örneklerin içerdikleri krom miktarıyla lineer olarak arttığını gösterdi. Bunun yanında örneklerin yaşam sürelerinin ve ışınım veriminin krom miktarıyla artan ışımasız geçişlerin etkisinden dolayı azaldığı gözlendi. Darbeli laser çalışmalarında, kurulan KTP optik parametrik osilatörünün (OPO) 1570 nm'deki çıkışı pompa olarak kullanıldı. Cr^{2+}:ZnSe laseri KTP OPO kavitesi içerisine kurularak dalgaboyu 1880-3100 nm aralığında değiştirilebilen ve 145 μJ' a varan çıkış enerjileri veren darbeli laser sistemi elde edildi. Elde edilen dalga boyu aralığı bu malzeme için gösterilmiş en geniş dalga boyu değiştirilebilirlik aralığıdır. Sürekli dalga Cr^{2+}:ZnSe laser deneylerinde, 1800 nm'de çıkışı olan bir Tm-fiber laseri kullanıldı. Kurulan sürekli dalga laserinden 640 mW'a varan güçler elde edildi ve laserin dalgaboyu 2240-2900 nm aralığında değiştirilebildi. Bunun yanında en iyi laser performansını verecek krom konsantrasyon miktarı laser güç ölçümleri ile belirlendi. Bu ölçüm sonucunda elde edilen değerin ışınım verimi ölçümleri ile uyumlu olduğu gözlendi.

ACKNOWLEDGEMENTS

This thesis will be on "Cr^{2+}:ZnSe lasers", and it is the result of part of my work as an undergraduate and graduate research assistant at the Laser Research Laboratory (LRL) of Koc University (KU) in the years 2000-2006. Of course, it would have been impossible without the help of several collaborators and sponsors. As my work for a MS degree at Koc University ends, I would like to thank all the people that made this work possible.

First and foremost, I would like to thank my research advisor Dr. Alphan Sennaroglu for establishing the LRL, and for all the support and guidance he has provided throughout these years. I would also like to thank Adnan Kurt for his constant involvement with my research at LRL. My interaction with Dr. Sennaroglu and Adnan Kurt has provided me a great opportunity to gain experience in experimental research, learning a lot from their numerous technical skills. I hope to have learned from their non-technical skills as well.

Dr. Mehmet Somer & Muharrem Guler from the KU Chemistry Department, Huseyin Cankaya from KU LRL and Nathalie Vermeulen, Dr. Heidi Ottevaere & Dr. Hugo Thienpont from Vrije Universiteit of Brussels have also contributed significantly to "Cr^{2+}:ZnSe lasers" project and I would like to thank for their continuing support during this work. Especially, this project would not have been possible without the continuing effort and excitement of Dr. Mehmet Somer.

I would also like to thank Dr. Alper Kiraz for taking his valuable time to serve on my thesis committee.

Besides the project on "Cr^{2+}:ZnSe lasers", I also have the chance of taking part in several other exciting projects. In these projects, it was a great pleasure to work with Dr. Iskender Yilgor & Emel Yilgor from the KU Chemistry Department, Idris Kabalci & Dr. Gonul Ozen from Istanbul Technical University, and Sarper Ozharar and Fatih Yaman from KU LRL.

During these years, I have enjoyed interacting with other past and present student members of KU LRL group. I especially would like to thank Hamit Kalaycioglu for his continuing support during the last two years. I would also like to thank Ahmet K. Erdamar, Serhat Tozburun, Ahmet F. Coskun, Dogan Efe, Natali Cizmeciyan, and Nuray Dindar for their friendship and support during the experiments. I thank my colleagues M. Yavuz Yuce and Umut Aydemir from the KU

Chemistry Department for their friendship and their technical help in the experiments. I would also like to thank my friends outside of the LRL group for their friendship. I am fortunate to have them around; and I would like to thank them for their company outside the research environment.

I am grateful to the engineering and science faculty of the KU for providing me with the education a MS endeavor requires. I thank the staff of the department: Nesrin Atag, Beyza Morgan and several others for their technical assistance through these years. Their assistance made my life at KU easier and my stay at KU more pleasant.

The primary support for my studies was provided by KU and TÜBITAK (The Scientific and Technical Research Council of Turkey, project TBAG-2030 and BAYG program), with additional funding from Network of Excellence in Micro-Optics (NEMO) funded by the European Union 6th Framework program, SPIE (Society for Optical Engineering), and OSA (Optical Society of America (OSA). I am grateful for their support without which this work would not have been possible. I especially would like to thank KU Student Support Fund for providing me financial aid and in particular to Dr. Iskender Yilgor for his confidence and support.

Finally, I wish to thank my family, for their continuing support, love and patience during my entire time at KU. It is to them, I wish to dedicate this thesis.

TABLE OF CONTENTS

LIST OF TABLES

LIST OF FIGURES

NOMENCLATURE

A	a constant
c	speed of light
D	diffusion coefficient
D_0	value of the diffusion coefficient at very high temperatures
e_{VB}	valance band electron
E	Energy
E_{ad}	activation energy
E_g	bandgap energy
f_p	normalized strength of excited-state absorption at λ_p
h	Planck constant
hυ	photon energy
$\hbar\omega$	phonon energy
h_{VB}	valance band hole
I_p	pump laser intensity
I_L	laser intensity
I_{sa}	absorption saturation intensity
$J_0(x)$	Bessel function of the first kind of order zero
$J_1(x)$	Bessel function of the first kind of order one
L	thickness
n_0	constant chromium vapor concentration on all sides of the ZnSe during diffusion
N(r,z,t)	chromium ion concentration
$N(\vec{r},t)$	chromium ion concentration
N_{Cr}	chromium ion concentration

p	number of phonons necessary to bridge the energy gap between the levels
P_L	laser power
P_p	pump power
R	radius
$R\alpha_m$	m^{th} positive root of $J_0(x)=0$
$\vec{r}$	position vector
r	cylindrical position coordinates
t	time
v_g	group velocity of the pump beam
W_{rad}	radiative decay rate
W_m	multiphonon relaxation rate
W(T=0)	nonradiative decay rate at low temperature
$W_{non\text{-}rad}$	nonradiative decay rate
z	cylindrical position coordinates
τ_f	fluorescence lifetime
τ_{rad}	radiative lifetime
$\tau_{non\text{-}rad}$	inverse of the non-radiative decay rate ($W_{non\text{-}rad}$)
λ	wavelength
λ_o	central wavelength of the absorption band
λ_P	pump laser wavelength
λ_L	laser wavelength
$\Delta\lambda$	full-width at half-maximum (FWHM) of the absorption band
ΔE	bandgap energy between ground and excited state energy levels
σ_o	peak absorption cross section
$\sigma_a(\lambda)$	absorption cross section at λ
σ_e	stimulated emission cross-section

σ_{esa}	excited-state absorption cross section
α	absorption coefficient
$\alpha(r,z,t)$	absorption coefficient
α_{loss}	differential loss coefficient
α_{p0}	pump absorption coefficient
θ	cylindrical position coordinates
ν_p	pump laser frequency
ν_L	laser frequency

Chapter 1

INTRODUCTION

1.1 Overview of Cr^{2+}:ZnSe Lasers

Undoped bulk II-VI semiconductors (also referred to as chalcogenides) such as CdSe, ZnSe, and ZnTe have a wide transparency window in the near infrared and mid infrared regions of the electromagnetic spectrum. If divalent transition metal ions (TM^{2+}) such as Co^{2+}, Cr^{2+}, and Fe^{2+} are introduced into these materials, crystal field splitting and strong electron-phonon coupling lead to the formation of broad absorption and emission bands in the mid infrared. As an example, let us consider the ZnSe medium which has a bandgap of 2.67 eV [1] and phonon energy of 250 cm^{-1} [2]. In contrast to pure bulk ZnSe whose transparency window extends from 0.5 to 22 μm [3], chromium-doped ZnSe (Cr^{2+}:ZnSe) possesses a strong absorption band centered near 1800 nm. Furthermore, optical excitation of the substitutional Cr^{2+} ions with a pump emitting in the 1500-2100 nm region produces a broad, strong emission band in the mid-infrared between 2 and 3 μm. As a matter of fact, these spectroscopic properties of Cr^{2+}:ZnSe in particular and of other TM^{2+}-doped chalcogenides in general have long been known [4-9]. For example, infrared absorption spectra of chromium-containing II-VI compounds were studied in detail by researchers since early 1960s [9-11]. In addition, absorption and emission characteristics of other TM^{2+} ions such as Fe^{2+} were thoroughly investigated [6-8, 12, 13]. Interestingly, despite this considerable interest in the spectroscopy of TM^{2+}-doped II-VI compounds, lasing action was not reported until mid 1990s. In the pioneering work reported by De Loach et al., absorption and emission characteristics of various zinc chalcogenides doped with Cr^{2+}, Co^{2+}, Ni^{2+}, and Fe^{2+} were studied to evaluate their potential as active media in the mid infrared, and room-temperature lasing was demonstrated with Cr^{2+}:ZnSe and Cr^{2+}:ZnS near 2.4 μm [14, 15]. Since then, tunable room-temperature laser action has also been successfully demonstrated with other chalcogenide hosts doped with Cr^{2+}, including CdSe [16-18], CdTe [19], ZnS_xSe_{1-x} [20], $Cd_xMn_{1-x}Te$ [21-25], CdZnTe [26], and others.

Cr^{2+}:ZnSe remains as the most extensively studied member of this class of lasers and, over the last decade, has emerged as a versatile source of broadly tunable laser radiation in the mid-infrared region between 2 and 3 μm. This gain medium possesses many favorable spectroscopic characteristics that enable efficient lasing. These include a 4-level energy structure and absence of excited-state absorption which allow low-threshold continuous-wave (cw) operation, a broad absorption band that overlaps with the operating wavelength of many laser systems for optical pumping, a phonon-broadened emission band that gives rise to wide tunability, and near-unity fluorescence quantum efficiency at room temperature. To date, gain-switched [14, 15], cw [27], diode-pumped [28], mode-locked [29], random-lasing [30], and single-frequency [31] operations have been demonstrated. Broad tunability in the 2000-3100 nm wavelength range in cw operation and in the 1880-3100 nm wavelength range in pulsed operation was also reported [2, 32]. Among the potential applications of Cr^{2+}:ZnSe lasers, we can list atmospheric imaging [33-35], vibrational spectroscopy [36-41], self-difference frequency mixing [42], and optical pumping of mid-infrared lasers as well as optical parametric oscillators [43].

In this thesis, we provide an extensive review of the recent studies aimed at the development of Cr^{2+}:ZnSe lasers. Since Cr^{2+}:ZnSe belongs to the family of tunable solid-state lasers, we start with a brief historical review of this field in Section 1.2. The key milestones are outlined and various examples of tunable solid-state lasers are mentioned. In Section 2, we describe various techniques that are commonly used for the synthesis and spectroscopic characterization of Cr^{2+}:ZnSe. In particular, we concentrate on diffusion doping and discuss how the diffusion time and diffusion temperature influence the strength of the absorption bands. Different techniques for the determination of the diffusion constant are then described. In Section 3, we discuss the fluorescence properties of Cr^{2+}:ZnSe. Experimental data showing the dependence of the fluorescence efficiency and fluorescence lifetime on chromium ion concentration are presented. The temperature dependence of the fluorescence lifetime is discussed. In Section 3.4, we further describe techniques with which the absorption cross section can be determined from cw and pulsed absorption saturation data. Pulsed operation of Cr^{2+}:ZnSe lasers is covered in Section 4. After a review of the earlier work, the dependence of the power performance on active ion concentration is discussed. In tuning experiments, we describe a pulsed, intracavity-pumped Cr^{2+}:ZnSe laser with an ultrabroad

tuning range extending from 1880 to 3100 nm. Continuous-wave operation of Cr^{2+}:ZnSe lasers is next discussed in Section 5. Here, after a review of the work on cw Cr^{2+}:ZnSe lasers, we describe the operation of a cw 1800-nm-pumped Cr^{2+}:ZnSe laser. The power performance of several Cr^{2+}:ZnSe samples were also investigated in order to determine the optimum chromium concentration for cw operation.

1.2 Historical Review of Tunable Solid-State Lasers

The Cr^{2+}:ZnSe laser belongs to the family of tunable solid-state lasers, also referred to as vibronic lasers due to the role of electron-phonon coupling in the broadening of the absorption and emission bands. In tunable solid-state lasers, the output wavelength can be tuned over a substantial fraction of the central emission wavelength. As such, the fractional tuning range, defined as $\Delta\lambda/\lambda_0$ ($\Delta\lambda$=full width of the tuning range and λ_0=the central emission wavelength) can be several tens of percent. Table 1.1 shows some examples of tunable solid-state gain media and their reported fractional tuning range at room temperature. Tunable solid-state lasers have a long history dating back to the early days of lasers. In this Section, we briefly outline some of the important historical developments in this field. For a comprehensive review on their physical properties and operational characteristics, we refer the reader to several excellent review articles on this subject [2, 30, 44-50].

Gain Medium	Tuning Range (nm)	$\Delta\lambda/\lambda_0$	Reference
$Ti^{3+}:Al_2O_3$	660-1180	0.57	[51]
$Cr^{3+}:BeAl_2O_4$	701-818	0.15	[49]
$Cr^{4+}:Mg_2SiO_4$	1130-1367	0.19	[52]
$Cr^{4+}:Y_3Al_5O_{12}$	1309-1596	0.20	[53]
$Co^{2+}:MgF_2$	1750-2500	0.35	[54]
Fe^{2+}:ZnSe	3900-4800	0.21	[55]
Cr^{2+}:ZnS	2110-2840	0.29	[56]
Cr^{2+}:CdSe	2300-2900	0.23	[17]
Cr^{2+}:ZnSe	1880-3100	0.49	this work

Table 1.1 Room-temperature tuning range of several transition metal ion-doped solid state gain media.

Work on tunable solid-state lasers started shortly after the invention of the ruby laser in 1960 [57]. First experimental demonstration of tunable laser action was reported by Johnson *et al*. in

flashlamp-pumped Ni^{2+}-doped magnesium fluoride (MgF_2) [58]. This was followed by the development of other tunable sources based on several crystal hosts doped with divalent ions such as Ni^{2+}, Co^{2+}, and V^{2+} [59-61]. These lasers could produce radiation in the near infrared between 1.1 and 1.8 μm but due to their low luminescence efficiency at elevated temperatures, they needed to be operated at cryogenic temperatures. In the meantime, a rigorous theoretical treatment of phonon-terminated lasers was also given by McCumber [62-65]. For over a decade between mid 1960s and late 1970s, limited activity continued in search for new tunable solid-state gain media and dye and color-center lasers were instead used widely as tunable sources. Toward the end of 1970's, interest in tunable solid-state lasers was revived. This was driven by two important developments. First, laser end pumping was introduced by Moulton *et al*. for the optical excitation of solid-state lasers [66]. Since the nearly diffraction-limited output of already existing commercial lasers could be focused to small volumes, lasing thresholds were considerably lowered. Second, as a result of improvements in crystal growth techniques, new high-quality tunable laser crystals became commercially available. One of the early examples of tunable solid-state media that emerged at this time was the alexandrite laser (Cr^{3+}:$BeAl_2O_4$). Since its invention in 1979 [67], there has been an ever growing interest in the spectroscopic characterization and development of new tunable solid-state lasers. To date, lasing action has been reported from many vibronic gain media including Ti^{3+}:sapphire [68], various chromium-doped lasers [37-45], Fe^{2+}:ZnSe [46], and others. By using different ion-host combinations, the wavelength range between 665 and 4500 nm can now be covered.

In the search for new tunable gain media, one of the most extensively explored transition metal ions has been chromium. This is primarily due to the chemical stability of the different ionic charge states in the lattice and the existence of broad pump bands. Depending on the charge state of the substitutional chromium ion introduced into the host, chromium-doped laser sources can be classified into three categories. The first group consists of Cr^{3+}-doped solid-state lasers such as alexandrite[67], Cr^{3+}-doped garnets [69, 70], Cr^{3+}:LiCAF [71], Cr^{3+}:LiSAF [72], and others. Some of these such as alexandrite and Cr^{3+}-doped garnets are among the earliest room-temperature tunable solid-state lasers. The tuning range is host-dependent and extends approximately from 700 nm to 1000 nm. The second category consists of the near-infrared Cr^{4+}-lasers such as Cr^{4+}:forsterite

and Cr^{4+}:YAG which have been extensively reviewed in Ref [45]. The third and the most recently explored group consists of divalent chromium-doped hosts such as Cr^{2+}:ZnSe which is the main theme of this thesis.

We note in passing that another important TM^{2+}-doped chalcogenide laser is Fe^{2+}:ZnSe in which lasing action was reported in the 4-5 μm wavelength range [73]. There is a lot of ongoing activity in the investigation of solid-state lasers and saturable absorbers based on Fe^{2+}:ZnSe. We refer the reader to Refs. [55, 73-79] for further discussion on these studies.

Chapter 2

SYNTHESIS AND ABSORPTION SPECTROSCOPY OF Cr^{2+}:ZnSe

In this chapter, we first provide a brief comparative review on different methods of preparing TM^{2+}-doped chalcogenide laser materials. In Section 2.2, thermal diffusion doping is discussed in detail. A theoretical model for thermal diffusion doping is described in Section 2.3. In Section 2.4, we presented the absorption spectra of pure and chromium doped ZnSe samples and discuss the modifications in the absorption spectra of ZnSe upon chromium doping. Dependence of passive losses on chromium concentration will be discussed in Section 2.5. Finally, in Section 2.6, we present our detailed work on the determination of diffusion coefficient for Cr^{2+}:ZnSe.

2.1 Synthesis Methods for Cr^{2+}:ZnSe

Various methods can be used to introduce the laser-active TM^{2+} ions into the chalcogenide hosts either during the growth of the host or after the growth process. Techniques that incorporate chromium ions during the growth of the host include melt growing [10], vapor growing [80, 81], pulsed laser deposition [82], molecular beam epitaxy [83], and temperature solution growth [84]. The most widely used post-growth technique is thermal diffusion [85].

Melt-growing (solidification from melt [86]) of chromium doped II-VI materials has been one of the extensively used methods [10, 14, 19, 21, 23, 25, 85, 87-90]. Here, a given amount of the dopant is first mixed with the host, and doped samples are then pulled from the molten mixture by using a modified vertical Bridgman growth technique. Previous studies showed that melt-grown samples suffer from being coarsely polycrystalline and contain defects such as inclusions and voids [14, 87]. Besides, controlling the dopant concentration is difficult since the actual dopant concentration in the sample is not necessarily the same as the starting concentration [23]. Hence, concentration gradients were observed in samples prepared with this method [14, 87]. Possibility of

uncontrolled contamination during the melting process, leading to unwanted passive losses, has also been pointed out [85, 88].

Vapor growth of Cr^{2+}:ZnSe using physical vapor transport (PVT) has been shown to produce samples with higher crystal and optical quality [15, 80]. However, with the PVT technique, obtaining samples with uniform chromium concentration is difficult [80, 85, 87, 91, 92]. Besides, previous studies also showed that chromium diffusion efficiency in this technique is relatively low for CdSe [93, 94] and CdS_xSe_{1-x} [95]. In a comparative study, it was shown that post-growth thermal diffusion doping is more effective in introducing chromium in CdS_xSe_{1-x} in comparison with the PVT technique [95].

Pulsed laser deposition of Cr^{2+}:ZnS thin films on silicon substrate has also been demonstrated [82]. In this technique, precise control of chromium dopant concentration was possible [82], but there is very little work in the literature on the optical quality of the samples prepared with this method. In some studies, pulsed laser deposition was also used to coat the host surfaces with chromium films, and then, thermal diffusion doping was employed in the second step to add the chromium ions into the host [96, 97]. This is discussed further in Section 2.2.

Another alternative method for introducing chromium into the chalcogenide host during the growth is molecular beam epitaxy [83]. This method allows for the fabrication of complex heterostructures and the adjustment of chromium concentration within the sample, enabling the growth of integrated structures [83]. On the other hand, the growth rates in this technique are very slow (~1μm/hour) for obtaining millimeter-sized bulk samples [98]. In addition, surface segregation of chromium during crystal growth may degrade the optical quality of the samples [83].

Thermal diffusion doping is the widely used post-growth technique for the preparation of Cr^{2+}:ZnSe samples [99]. In comparison with the above techniques which require sophisticated instrumentation, thermal diffusion doping offers a simple, efficient, and cost-effective alternative. This method has been known for decades, and in the earliest studies on chromium doped II-VI semiconductors, samples prepared with this technique were used [9]. Chromium doping level of the samples can be adjusted easily by varying the diffusion temperature and/or the diffusion time. However, spatial inhomogeneities in chromium concentration may result due to the nature of the

diffusion process. Furthermore, slightly higher passive losses have been observed in diffusion-doped samples in comparison with those obtained by using other methods such as PVT [100].

2.2 Thermal Diffusion Doping

The thermal diffusion doping method uses commercially available ZnSe samples in crystalline, polycrystalline or ceramic [101] form as the starting host material. Polycrystalline samples have been widely used since their laser and spectroscopic properties are comparable with those of single-crystal Cr^{2+}:ZnSe samples [102]. As the dopant, sputtered film of metallic chromium deposited on the ZnSe host surface [9, 10, 85, 88, 103] or powders of CrSe (or Cr) [81, 86, 104, 105] can be used. Our experimental work showed that thermal diffusion doping is faster using CrSe powder in comparison with Cr powder. The deposition of metallic chromium on ZnSe surface was accomplished by using magnetron sputtering systems [103] or pulsed laser deposition [96, 97]. One important issue that needs to be addressed is that both the dopant and host must be extremely pure in order to obtain laser-quality samples (purity better than 99.99%). Sometimes, this may require additional purification steps before diffusion. Even trace amounts of impurities will cause unwanted losses in the doped material. As an example, Fe^{2+} in ZnSe has a strong absorption band between 2.2 and 5 μm, overlapping with the emission band of Cr^{2+}:ZnSe [73, 99]. Hence, the presence of Fe^{2+} may greatly reduce the lasing efficiency [3, 74, 94].

Figure 2.1 Schematic of the silica ampoule used in the preparation of Cr^{2+}:ZnSe by thermal diffusion doping.

In our studies, polycrystalline ZnSe samples were used for diffusion doping (10 mm dia x 2.0 mm tablets from Crystran Ltd, and 9.5 mm dia x 3.0 mm tablets from Lambda Research Optics, Inc.). The samples were microcrystalline in structure and were grown by chemical vapor deposition from zinc vapor and H_2Se gas [106]. Highly pure powders of CrSe or Cr were used as dopant (Cr

and CrSe powders, from Aldrich). Figure 2.1 shows a sketch of the silica ampoules used for diffusion doping. The dopant (Cr or CrSe powder) and the host (ZnSe) are placed in different compartments so that the deposition of the dopant on the ZnSe occurs only via gas phase. As a result, contamination due to less volatile impurities such as metal oxides could be minimized. Besides, preventing a direct contact between the CrSe powder and ZnSe gives rise to a more uniform distribution of the dopant inside the sample and prevents the formation of hot spots on the sample surface [85]. The ampoule is then evacuated and sealed under high-vacuum ($P < 10^{-5}$ mbar). The evacuation of the tube is essential for diffusion to occur. Besides it also prevents oxygen from reacting with the Zn metal and forming oxides [100].

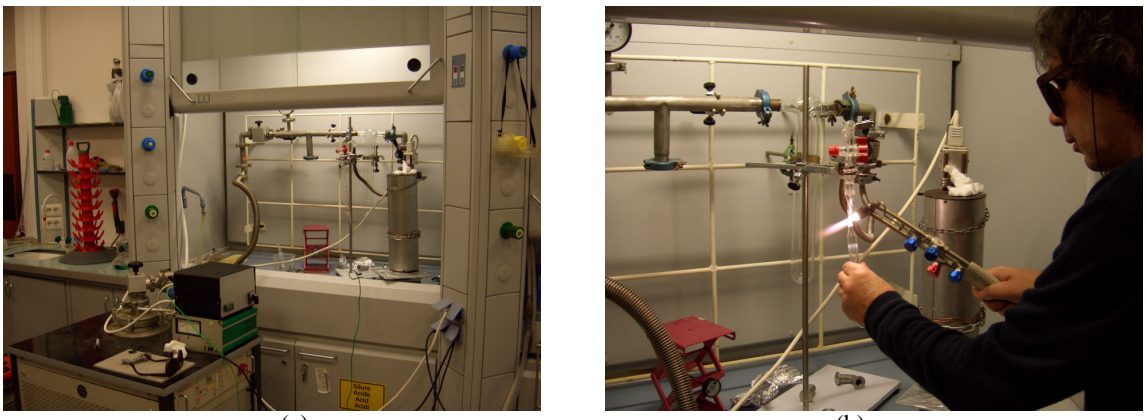

(a) (b)

Figure 2.2: (a) Photograph of the vacuum line, (b) Prof. Mehmet Somer while closing the silica ampoule under high vacuum.

Figure 2.2 (a) shows the vacuum line that we have been using in thermal diffusion doping experiments. In Figure 2.2 (b) Prof. Somer is seen while closing the opening of the silica ampoule. Here, we note that heating of the silica ampoules before closing them under high vacuum is also an essential step in the preparation of silica ampoules. This heating vaporizes any water containing molecules etc., and enables a better evacuation of the ampoule. Figure 2.3 shows the prepared silica ampoules containing CrSe powder and pure ZnSe tablets. The silica ampoule length was about 20 cm.

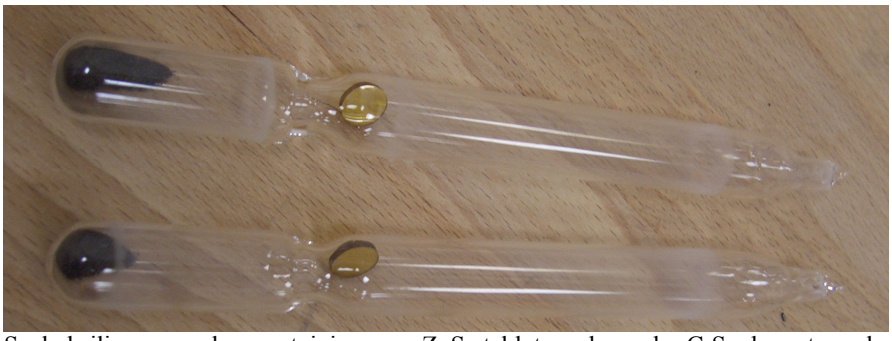

Figure 2.3: Sealed silica ampoules, containing pure ZnSe tablets and powder CrSe dopant, ready for thermal diffusion doping.

Diffusion was activated thermally by heating the system to temperatures between 800 and 1100 °C using the tube furnace shown in Figure 2.4 (Carbolite GMBH, Model: STF 15/--/610) [107]. The tube furnace has a tube length of 120 cm, and the maximum temperature that the furnace can be operated is 1500 °C. The heated length of the silicon carbide tube is 60 cm, and the length over which temperature uniformity (± 5 °C) can be obtained was 40 cm. Special care was taken to place the silica ampoule at this uniformly heated region at the center of the tube (See Fig. 2.5).

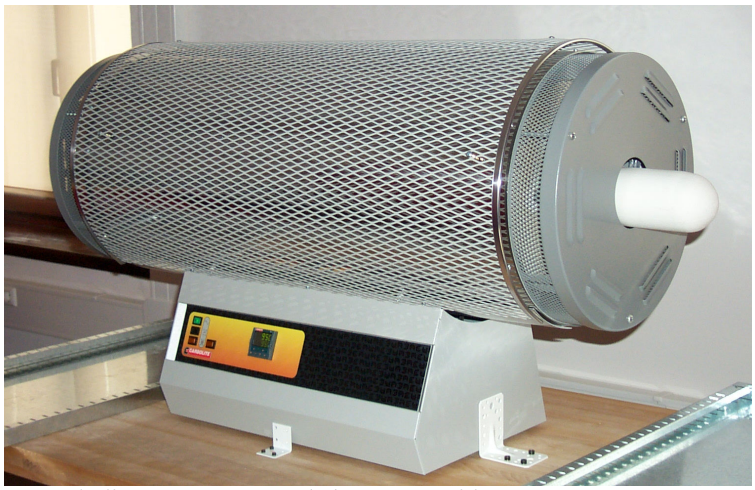

Figure 2.4. Carbolite GMBH STF 15/--/610 oven with a 2416CG temperature controller.

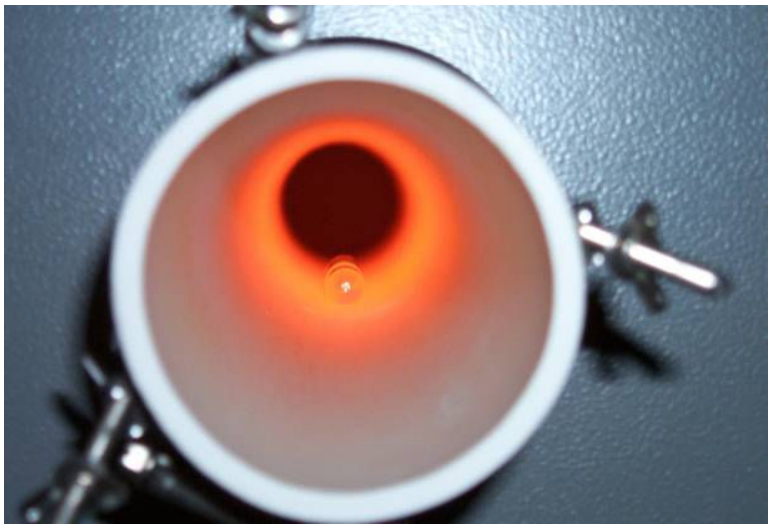

Figure 2.5 Silica ampoule seen inside the tube furnace during thermal diffusion doping.

Throughout the thermal diffusion process CrSe will vaporize and CrSe vapor pressure on the surface of ZnSe will rise. Then an equilibrium process will start and some of the Cr^{2+} ions will replace the Zn^{2+} ions in ZnSe, and chromium diffusion into ZnSe will occur [100]. The applied diffusion times varied from several hours to tens of days. By adjusting the diffusion temperature and/or the diffusion time, one can control the average chromium concentration in the host as will be delineated in Section 2.3.

Different heating/cooling rates of the silica ampoule might be used. In our studies the heating rate was ~1000 °C/hour. Figure 2.6 shows the temperature of the oven with respect to time in simple control mode when the temperature is set to 1000 °C. As a cooling rate we tried both 200 °C/hour and 10°C/hour; however, we did not observe any significant variation in the optical properties of the prepared samples. Figure 2.7 shows the temperature of the oven with respect to time in simple control mode when the temperature is set to 0 °C. Here we note that the oven could also be operated in "control with ramp-to-setpoint" mode where in such a case the cooling and heating rates are constant with time. Some studies used rapid cooling by dropping the ampoules into water to ensure maximum concentration of doping inside the host [9], where other studies used slow cooling rates probably aiming to prevent the formation of defects (~5°C/hour, [26]).

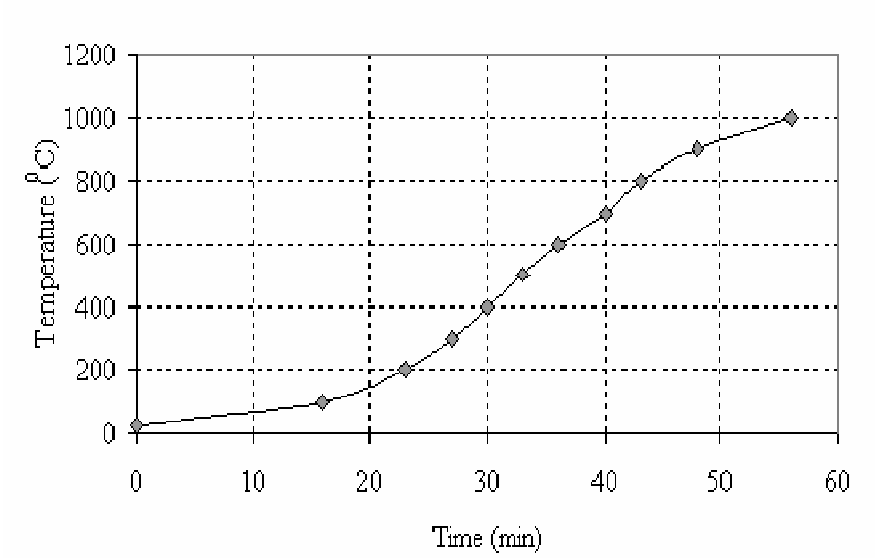

Figure 2.6. Typical heating curve for the oven in simple control mode when the temperature is set to 1000 °C.

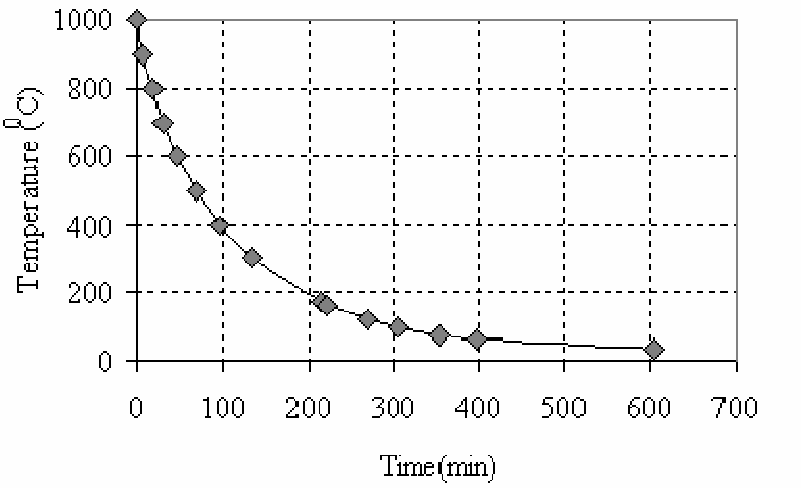

Figure 2.7. Typical cooling curve for the oven in simple control mode when the temperature is set to 20 °C.

Cr^{2+}:ZnSe samples prepared by thermal diffusion doping require polishing after the synthesis process due to two reasons. First, the surface roughness increases during diffusion and polishing improves the optical quality of the doped samples. Second, polishing also removes the heavily chromium-doped layer near the surface. As will be further noted in the following sections, high

chromium concentration causes several unwanted effects such as enhanced non-radiative decay and increased passive losses. Hence, removal of the highly-doped layer can improve the laser performance of the samples.

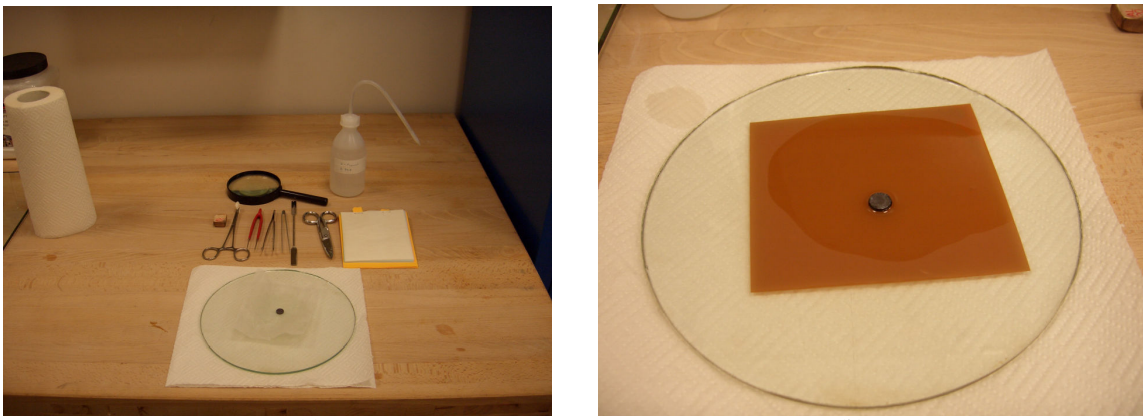

(a) (b)

Figure 2.8 (a) Setup for the first step of polishing, (b) polishing with 5µm lapping film.

In our studies, we used manual mechanical polishing. As the initial step, 5- and 3-µm polishing/lapping films bought from Thorlabs were used successively to quickly remove the excess rough layer from the sample surface (See Fig. 2.8). This step took approximately 30 minutes and ends when only a very little roughness remains on the surface of the sample. This generally requires the removal of several tens of micrometers of material from each surface.

(a) (b)

Figure 2.9 (a) Setup for the last step of polishing, (b) polishing with 1µm alumina powder.

As a second step 1 μm alumina powders and a suitable polishing cloth bought from Allied were used (See Fig. 2.9). This last fine polishing step is essential for obtaining laser-quality samples with very low Fresnel losses, and it took approximately 1 hour to complete this step. ZnSe material is soft, and vulnerable to scratches. Thus, throughout all the polishing steps, to prevent scratches on the surfaces of the sample and to obtain sufficient smoothness on the lapping film and clothes, samples were wetted with isopropyl alcohol.

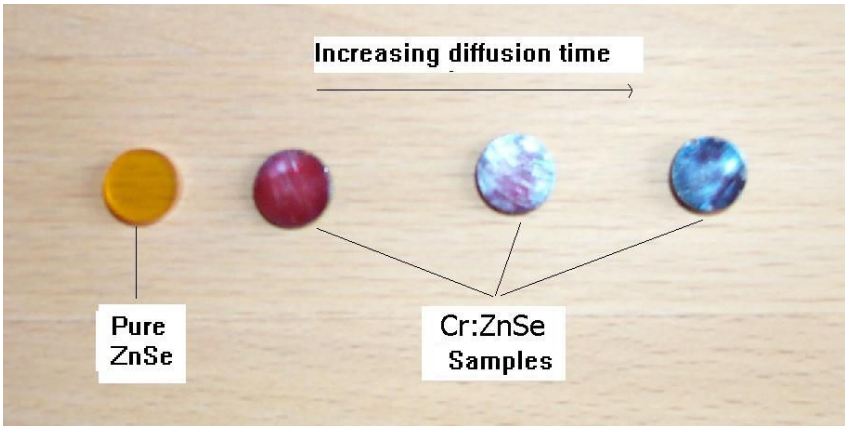

Figure 2.10 Pure and chromium doped ZnSe samples.

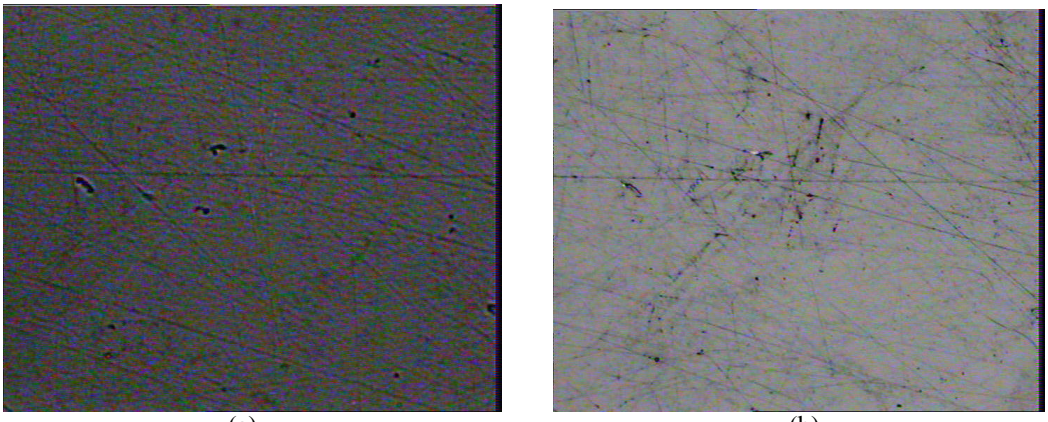

(a) (b)

Figure 2.11 Hundred times magnified black and white photograph of the Cr:ZnSe (a) transmission (b) reflection.

Figure 2.10 above shows pure and chromium-doped ZnSe samples. As more and more chromium is incorporated into ZnSe the color of the samples change from orange to dark red due to

the shift of the low wavelength absorption edge with increasing chromium concentration (see Section 2.4.4). Figure 2.11 shows the black and white photograph of one of the Cr^{2+}:ZnSe samples taken with a microscope. The magnification of the microscope was 100. Both the transmission (a) and reflection (b) images are shown.

2.3 Modeling of Thermal Diffusion Doping

The concentration of the chromium ions inside the host varies with position, diffusion time, and diffusion temperature. Here, we discuss a fairly accurate model of the thermal diffusion doping process based on the solution of the diffusion equation in cylindrical coordinates [99]. In this model, a constant dopant vapor concentration is assumed on all sides of the sample during diffusion. The concentration $N(\vec{r},t)$ of the chromium ions inside the host can be calculated by using the well-known diffusion equation

$$\frac{\partial N(\vec{r},t)}{\partial t} = D\nabla^2 N(\vec{r},t), \tag{2.1}$$

where t is the diffusion time, $\vec{r}$ gives the position inside the ZnSe sample, and D is the diffusion coefficient. In our case, the samples were cylindrical in shape, with radius R and thickness L. In this case Eq. 2.1 can be solved exactly in cylindrical coordinates by using the following set of initial/boundary conditions:

. (2.2)

Above, n_0 is the constant chromium ion vapor concentration on all sides of the ZnSe sample. The solution of the above boundary-value problem can be expressed as

$$N(r,z,\mathrm{t}) = n_0 - \frac{8n_0}{\pi R}\sum_{m=1}^{\infty}\sum_{n=0}^{\infty}\frac{(-1)^n \mathrm{J}_0(\mathrm{r}\alpha_m)}{(2n+1)\alpha_m \mathrm{J}_1(R\alpha_m)} Cos\left(\frac{(2n+1)\pi}{L}z\right) e^{\left(-\left(\frac{(2n+1)^2\pi^2}{L}+\alpha_{\mathrm{n}}^2\right)Dt\right)}, \tag{2.3}$$

where n and m are summation indices, $\mathrm{J}_0(x)$ is the Bessel function of the first kind of order zero, $\mathrm{R}\alpha_m$ is the m^{th} positive root of $\mathrm{J}_0(x)=0$ and $\mathrm{J}_1(x)$ is the Bessel function of the first kind of order one [108]. A detailed description of the solution of the diffusion equation in cylindrical coordinates is presented in Appendix A. Using Eq. 2.3 one can calculate the chromium concentration variation

inside ZnSe samples. As an example Fig. 2.12 shows the calculated variation of chromium concentration with radial position. Darker regions correspond to higher chromium concentration levels. The hypothetical sample is assumed to have a radius of 5 mm. Note that the concentration peaks near the boundaries as expected. Also note that at the center of the sample there is a large region where the concentration is almost constant. This point will be further discussed in Section 2.6.

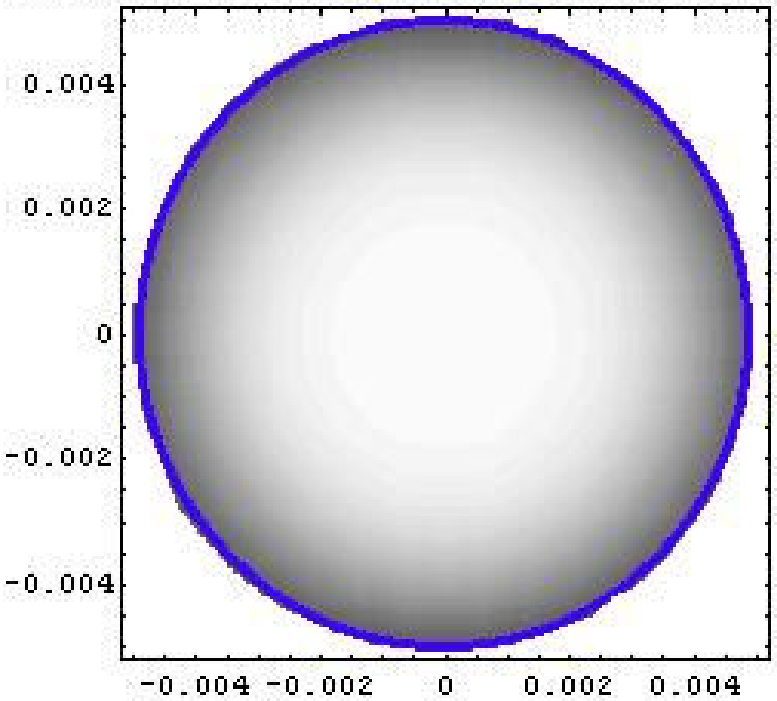

Figure 2.12. Calculated variation of chromium concentration with position inside a ZnSe with radius 5 mm.

2.4 Room-Temperature Absorption Spectra

2.4.1 Absorption Spectrometer

Absorption and transmission spectra of the samples were measured using a commercial spectrophotometer (Shimadzu, UV-3101PC) in the wavelength range of 300-3200 nm [109]. Figure 2.13 shows the spectrophotometer that was used. During most of the measurements, the following

measurement parameters were used: (scan speed=slow, scan step=0.5 nm, wavelength resolution=1 nm). Choosing a wavelength resolution below 1 nm decreased the signal to noise ratio in the mid infrared so wavelength resolution was taken as 1 nm.

Figure 2.13: Shimadzu spectrophotometer that was used in the optical transmission and absorption measurements.

2.4.2 Absorption Spectra of ZnSe

Figure 2.14 shows the absorption spectrum of a 2-mm-thick pure ZnSe crystal, between 300 and 3200 nm, measured at room temperature. The following observations could be made from this graph.

Observation 1: When we look at lower-wavelength part of the spectrum, we see that there is a strong absorption band due to the transition from the valance band to the conduction band of ZnSe (See Fig. 2.16). The short wavelength absorption edge for pure ZnSe is about 472 nm (this wavelength is somewhat arbitrary, it is the wavelength where the absorption coefficient reaches half of the maximum absorption coefficient that the spectrophotometer can measure). Now if we calculate the energy of the photon that has a wavelength of 472 nm, using Planck's relation we find that:

$$E = \frac{hc}{\lambda} = \frac{\left(6.626x10^{-34}\right)x\left(2.998x10^{8}\right)}{472x10^{-9}} \approx 4.208x10^{-19}\,Joule \approx 2.627eV$$

This energy corresponds to the minimum energy of the photon which can excite an electron from the valance band to the conduction band in the ZnSe semiconductor. Also this is the band-gap energy of ZnSe at room temperature, (2.627 eV).

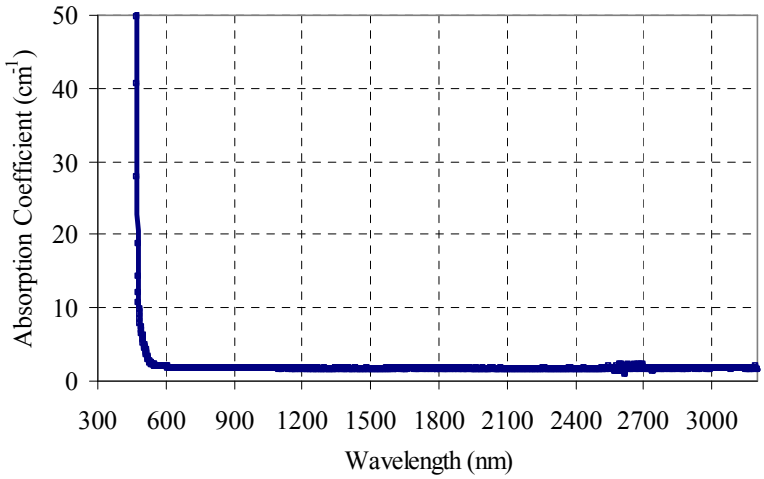

Figure 2.14. Absorption spectra of 2-mm thick pure ZnSe.

There exists a more accurate way of determining band gap energy of semiconductors. Band gaps of semiconductors can be determined by studying the dependence of the absorption coefficient α on the photon energy hν [110]. For direct and indirect allowed transitions, the theory of fundamental absorption leads to the following photon energy dependence near the absorption edge

$$\alpha \propto (h\upsilon - E_g)^m \tag{2.4}$$

where hυ and E_g are the photon and the bandgap energy, respectively. In this relation, the values of m are ½ and 2 for direct allowed and indirect allowed transitions, respectively. In our case, the variation of the absorption coefficient with the photon energy followed the relation

$$\alpha h\upsilon = A(h\upsilon - E_g)^{1/2} \tag{2.5}$$

where A is a constant.

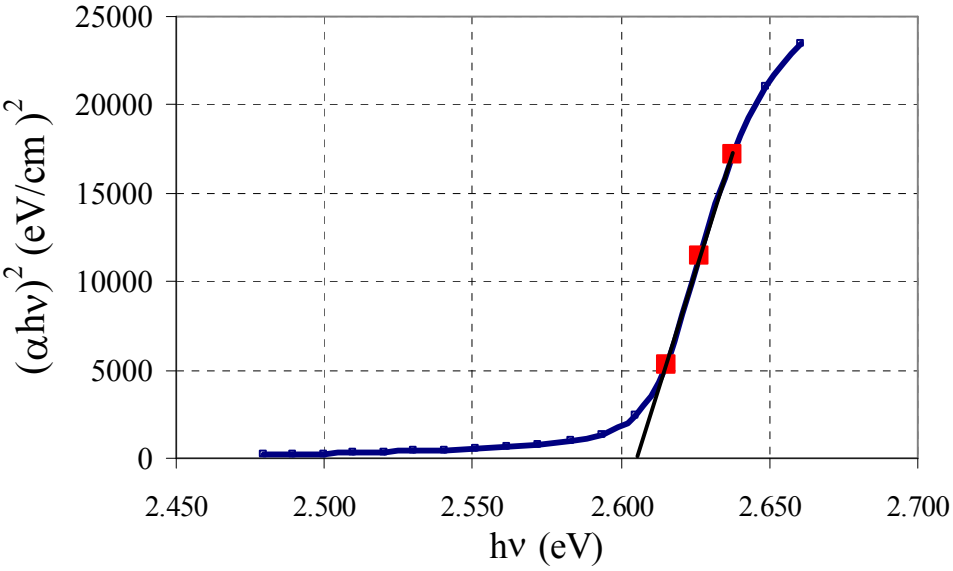

Figure 2.15 Determination of the bandgap energy of ZnSe material from absorption spectra.

Figure 2.15 shows the plot of $(\alpha h\upsilon)^2$ versus $h\upsilon$. The plot indicated straight-line behavior, indicating direct optical absorption in our polycrystalline ZnSe samples (m=1/2). Extrapolation of the linear portion of the plot onto the $h\upsilon$ axis gave the energy band gap of the sample, as 2.606 eV, which is in good agreement with the values reported in the literature [110].

Observation 2: Pure ZnSe has a clear yellow color. When we look at Figure 2.14, we see that pure ZnSe absorbs below 500 nm, so it absorbs violet and blue, but transmits green, yellow, orange and red light. So, it transmits between 500 nm and 700 nm in the visible spectrum, and 600 nm is in the middle.

Observation 3: All materials are bounded by limiting regions of absorption caused by atomic vibrations in the far-infrared (>10μm), and motions of electrons and/or holes in the short-wave visible regions [111]. In the interband region, the frequency of the incident radiation has insufficient energy ($E=hf$) to transfer electrons to the conduction band and cause absorption; here the material is essentially loss-free [111]. We looked at pure ZnSe's absorption spectra from Figure 2.14, and observed the short wavelength absorption edge due to electronic absorption around 2.6

eV. We could not observe the long wavelength transparency limit of ZnSe from Figure 2.14 (due to lattice absorption), because the long wavelength absorption edge of ZnSe was around 20 μm [106],beyond the operating range of the spectrometer.

2.4.3 Energy Level Diagram of Cr^{2+}:ZnSe

In a laser material, the active ion should ideally match the size and valence state of the host-lattice ion it replaces. To a very good approximation, the Cr^{2+} ion in ZnSe does meet these requirements. Chromium ions enter the ZnSe host as substitutional impurities and occupy the Zn^{2+} cation sites in the lattice [11]. The ionic radius of the Cr^{2+} ion in tetrahedral coordination in ZnSe is r_{Cr}^{2+} =0.905 Angstrom, slightly larger than that of the Zn ion it replaces, which has r_{Zn}^{2+}= 0.880. During this process, chromium atoms join the bond with their two electrons, and their charge state become Cr^{2+}. However, as a general chemical property, transition metal ion doped semiconductors can have different charge states. In our case, although the neutral charge state of the chromium ion in ZnSe crystal is Cr^{2+}, electron spin resonance experiments revealed both Cr^{1+} ($3d^5$) and Cr^{3+} ($3d^3$) charge states in the material [10, 81]. However, it was shown that Cr^{2+} is the stable charge state in ZnSe, and more than 95 % of the chromium have a valence of two [10]. In support of this, recent deep-level spectra in Cr^{2+}:ZnTe have shown that the concentration of Cr^{1+} ions is about 10^{-5} of the total added chromium [98].

Figure 2.16 shows a simplified energy level diagram of the Cr^{2+} ($3d^4$) ion in the ZnSe host [2, 112]. The ground level of the Cr^{2+} ($3d^4$) ion splits into the $^5T_2$ and ^5E energy levels inside ZnSe host. This splitting of the ($3d^4$) energy levels of the Cr^{+2} ions can be explained using crystal field theory. Briefly, when a Cr^{+2} ion in free space is placed in a crystal lattice (ZnSe), the electrons in the outermost orbits of the Cr^{+2} ion will experience an extra spherically non-symmetric electric force due the other ions inside the crystal. The electric field which causes these forces is called the "crystal field". In a free ion all the d-shell electrons have the same energy (the level is degenerate). However; inside ZnSe the degeneracy is lifted, since the spherically non-symmetric electric force effect on the d-shell electrons with different angular momentum is not the same. Further splitting of these energy levels occurs as a result of the Jahn-Teller effect. The energy levels all lie within the forbidden bandgap of the ZnSe semiconductor.

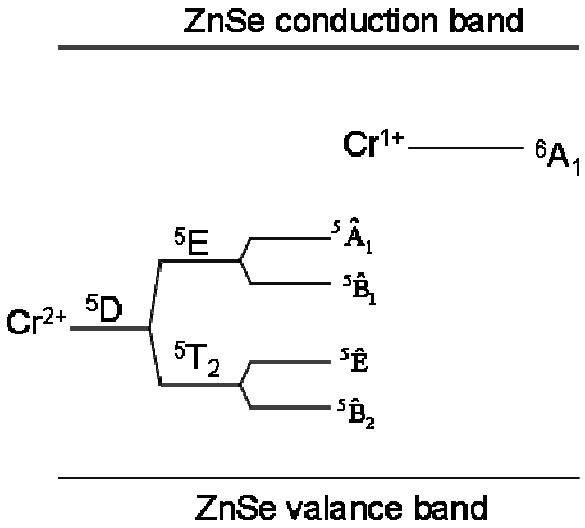

Figure 2.16. Energy level diagram of Cr^{2+} in ZnSe. ^5D energy level of the Cr^{2+} ion splits into ^5E and $^5T_2$ energy levels under the influence of the crystal field. These levels are further split due to the Jahn Teller effect. All these energy levels lie inside the forbidden bandgap of ZnSe.

2.4.4 Absorption Spectra of Cr^{2+}:ZnSe

Figure 2.17 shows the room-temperature absorption spectra of undoped and chromium-doped ZnSe samples in the 300-3100 nm spectral range. The three chromium doped samples shown in the figure (Samples 1-3) were prepared using thermal diffusion doping at 1000 °C with diffusion times of 1 (s1), 4 (s2), and 5 (s3) days, respectively. The undoped material is transparent at wavelengths above 470 nm, corresponding to the band-gap energy of 2.67 eV for ZnSe [1]. Diffusion doping of chromium modifies the absorption spectra of ZnSe in several ways. First, a strong absorption band of the laser-active Cr^{2+} ion forms in the near-infrared region centered at 1775 nm. This absorption band is due to the optical transitions between the $^5T_2$ and ^5E levels of the Cr^{2+} ions (Fig. 2.16). The differential absorption coefficient $\alpha(r,z,t)$ of this band can be expressed in terms of the chromium ion concentration N(r,z,t) and the absorption cross section $\sigma_a(\lambda)$ as

$$\alpha(r,z,t) = \sigma_a(\lambda) N(r,z,t) . \qquad (2.6)$$

Here note that absorption coefficient is a function of position and varies inside the sample.

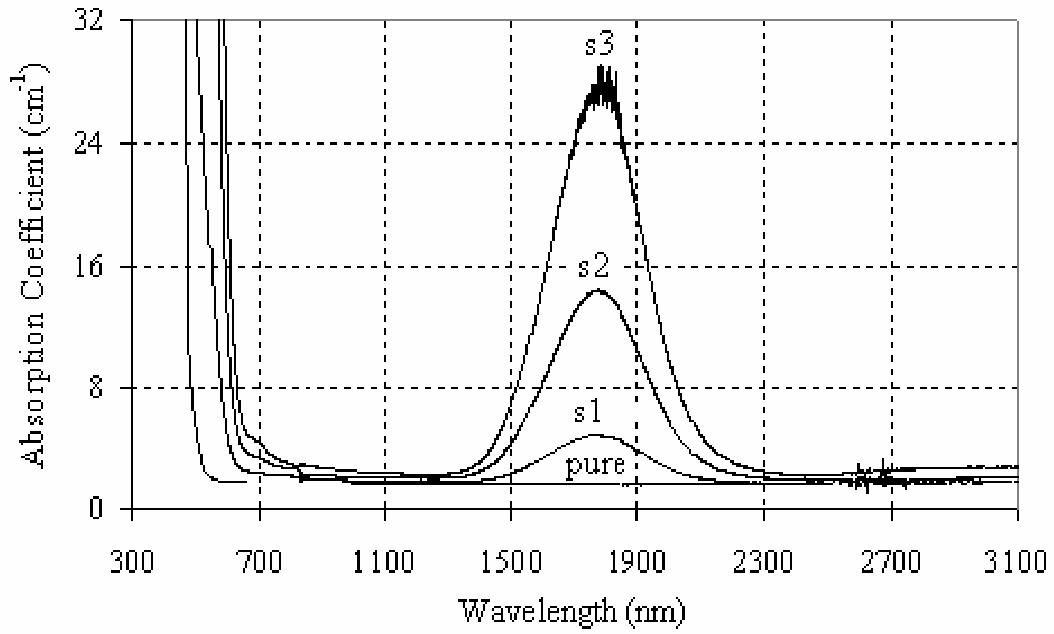

Figure 2.17. Room-temperature absorption spectra of pure and chromium-doped ZnSe samples. Cr^{2+}:ZnSe Samples 1-3 (s1 through s3 in the figure) were subjected to diffusion at 1000 °C for a period of 1, 4, and 5 days, respectively. Each sample had a thickness of about 2 mm.

In our measurements, we measured the transmission and absorbance of the samples along their Z-axis. Figure 2.18 above shows the calculated variation of chromium concentration inside a sample with thickness L. In this kind of a measurement, the transmission T of the samples can then be expressed in terms of absorption cross section as

$$T = \exp\left(- \int_{-L/2}^{L/2} \alpha(r,z,t)dz \right). \tag{2.7}$$

The absorbance (A) is related to the transmission through A = -Log (T). After determining the background losses A_b due to surface imperfections and Fresnel reflections, the average absorption coefficient α_{av} was determined by using

$$\alpha_{av} = \frac{1}{L}\frac{A - A_b}{\ln 10}. \tag{2.8}$$

Here we stress again that the value obtained from Eq. 2.8 gives the average value of the absorption coefficient due to the concentration variation shown in Fig. 2.18.

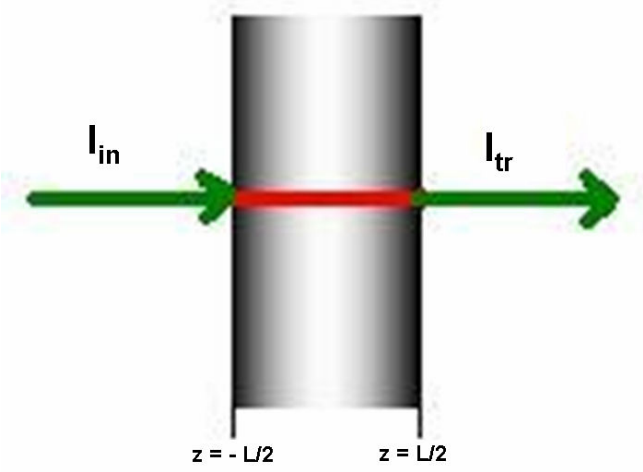

Figure 2.18. Transmission measurement along the z axis of a Cr^{2+}:ZnSe sample. Darker regions correspond to higher chromium concentration.

The absorption band around 1.8 μm has a Gaussian shape, and the wavelength dependence of absorption cross section can be accurately represented by the following empirical formula:

$$\sigma_a(\lambda) = \sigma_o \mathrm{Exp}\left[-4\left(\frac{\lambda-\lambda_o}{\Delta\lambda/\sqrt{\ln(2)}}\right)^2\right]. \qquad (2.9)$$

In equation 2.9, σ_o is the peak absorption cross section, λ is the wavelength, λ_o and $\Delta\lambda$ are the central wavelength and the full-width at half-maximum (FWHM) of the absorption band, respectively [85]. Experimental absorption measurements taken with Cr^{2+}:ZnSe samples show that λ_o and $\Delta\lambda$ do not vary significantly with concentration. Best fit between experimental data and Eq. 2.9, gave λ_o=1775 nm and $\Delta\lambda$=365 nm for Cr^{2+}:ZnSe. Equations 2.8 and 2.9 can be used to determine the Cr^{2+} concentration from absorption measurements. Most studies have used the σ_o-value of 11.5×10^{-19} cm^2 reported by Vallin et al. [10].

Finally, note that this absorption band around 1.8 μm is very wide (Δλ=365 nm), mainly due to vibronic coupling [2]. At room temperature, the ions that constitute the ZnSe crystal are in oscillation around a equilibrium point, thus the energy difference between the split level is constantly varying (since the crystal field strength, which splits the energy levels, varies with oscillation). During an optical measurement, the ZnSe ions that forms the crystal field on the Cr^{2+} dopant ion, will be on an arbitrary position on their periodic vibration. Thus, for each Cr^{2+} ion, the energy difference between the $^5T_2$ and ^5E energy levels are different. Due to the differences between the energy levels, in optical absorption measurements made at room temperature, instead of a central sharp wavelength, a wide absorption band around this position is seen. For Cr^{2+}: ZnSe at room temperature this central wavelength is approximately 1775 nm (0.7 eV), going from 1600 to 2100 nm, this enables the use of numerous different pump sources to excite the Cr^{2+}:ZnSe gain medium.

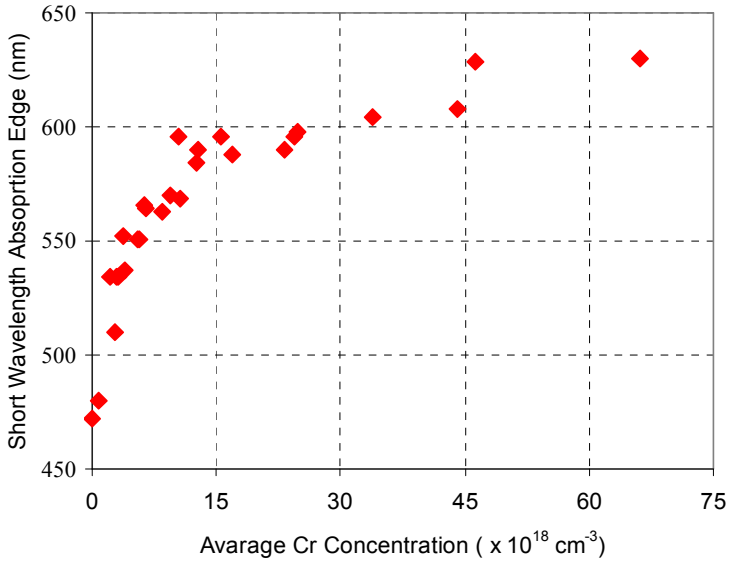

Figure 2.19 Measured variation of the short-wavelength absorption edge for Cr^{2+}: ZnSe as a function of the average Cr^{2+} concentration.

The second effect of chromium ion on the ZnSe absorption spectra is the shift of the short-wavelength absorption edge of ZnSe (~470 nm) to longer wavelengths. This shift is due to an absorption band around 500 nm originating from the $Cr^{2+} + e_{VB} \rightarrow Cr^{1+} + h_{VB}$ transition (where e_{VB}

is a valance band electron and h_{VB} is a valance band hole) [113-115]. This transition is one of the ways of generating rarely found Cr^{1+} charge state of chromium in ZnSe [10]. Previous studies showed that the strength of this band scales with the Cr^{2+} ion concentration. The amount of the short wavelength absorption edge shift is also related to the dopant concentration. Figure 2.19 shows the measured variation of the shift in the absorption edge as a function of average chromium concentration. In our studies, we observed a maximum shift of 160 nm (band edge ~ 640 nm) for a sample with an active Cr^{2+} ion concentration of $66x10^{18}$ ions/cm^3. As noted earlier, this shift is the reason for the change of sample color with chromium concentration. There are two more transitions near the band gap edge of ZnSe, one at 610 nm and another at 680 nm which are hardly visible in the room-temperature absorption spectra shown in Fig. 2.17 [86]. The origin of these transitions is not clear and more detailed information can be found in Ref. [86].

Another important band of Cr^{2+} ion in ZnSe is centered around 6.5 μm, extending up to 14 μm on the long wavelength side [86]. The importance of this band lies in the fact that its short wavelength side also overlaps with the lasing wavelength range of Cr^{2+}:ZnSe, causing unwanted absorption losses [86]. This band is due to the $^5\hat{B}_2 \rightarrow {}^5\hat{E}$ transition within the Jahn-Teller split ground state $^5T_2$ level (see Fig. 2.16) [86]. Sorokina et al. investigated the effect of residual ground-state absorption loses on lasing performance in detail, and stated that these losses are due to the overlap between the $^5T_2 \rightarrow {}^5E$ and the $^5\hat{B}_2 \rightarrow {}^5\hat{E}$ transitions of Cr^{2+} ion [116]. The effect of this band on lasing performance will be discussed more in the following sections.

2.5 Dependence of Passive Laser Losses on Chromium Concentration

Earlier studies with Cr^{2+}:ZnSe gain medium showed that increasing chromium concentration leads to increased passive losses at the lasing wavelengths [28]. We used the measured absorption spectra of Cr^{2+}:ZnSe samples with different chromium concentrations to investigate this effect in detail. Comparison of the measured absorption spectra of the Cr^{2+}:ZnSe samples with those of the undoped ZnSe allows the estimation of the passive losses at the lasing wavelengths (around 2500 nm, see Fig. 2.17). Our measurements showed that, despite slight variations from sample to sample, passive losses of Cr^{2+}:ZnSe increase linearly with increasing Cr^{2+} concentration. This can be clearly seen in

the absorption spectra of the three Cr^{2+}:ZnSe samples shown in Fig. 2.17. For example, whereas sample 1 with a Cr^{2+} concentration of $2.7x10^{18}$ ions/cm^3 has an estimated single-pass loss of about 2 % at 2500 nm, the loss increases to above 10 % for sample 3 which has a concentration of $23.2x10^{18}$ ions/cm^3. Based on the absorption spectra of more than 10 polycrystalline Cr^{2+}:ZnSe samples, we obtained the following empirical equation for the differential loss coefficient at 2500 nm (α_{loss}, in the units of cm^{-1}) as a function of the average Cr^{2+} concentration N_{Cr} (cm^{-3}):

$$\alpha_{loss} \approx (0.04 \pm 0.02) + \{(0.02 \pm 0.01) x 10^{-18}\} N_{Cr} . \quad (2.10)$$

Please note that Eq. 2.10 gives only a rough estimate and variation is observed in some cases. The constant part of the loss in Eq. 2.10 (0.04±0.02 cm^{-1}) is probably due to the scattering losses from the roughly polished surfaces of the samples, and could be minimized via better polishing. However, the second contribution to the loss, which scales with the Cr^{2+} concentration, is the main problem for Cr^{2+}:ZnSe samples.

The reason for this concentration dependent passive loss might be several. Firstly the diffusion process itself might be causing it, by generating defects in ZnSe, as observed in the preparation of n or p type ZnSe [117]. For example, Ivanov et al. recently suggested the application of the post growth annealing of Cr^{2+}:ZnSe samples in zinc vapor at 940 °C for 10 to 40 days as an essential step to improve optical quality of samples [118]. They proposed that such annealing process in zinc vapor eliminates losses in the ZnSe host due to the zinc vacancies [118]. Besides that, it is well known that trace amounts of impurities such as Fe in the dopant (CrSe powder) may cause substantial losses at the emission wavelengths of Cr^{2+}:ZnSe [104]. Moreover, as previously noted in Section 2.4.3, detailed previous work suggested that some part of this loss is probably due to a second absorption band with a peak centered around 6.6 μm, extending up to 14 μm (at 300 K) [44, 86, 112, 116, 119]. Losses due to defects or impurities could be eliminated; however, self absorption losses observed at the lasing wavelengths appears as one of the unavoidable properties of Cr^{2+}:ZnSe gain medium, which degrades laser performance. The effects of losses on laser performance will be discussed in more detail in the following sections.

2.6 Determination of the Diffusion Coefficient

Knowledge of the diffusion coefficient for Cr^{2+} ions in the ZnSe host facilitates the preparation of Cr^{2+}:ZnSe samples with a desired active ion concentration. In previous studies, Ndap et al. studied the preparation of Cr^{2+}:ZnSe samples by thermal diffusion doping between 800 and 950 °C to determine the diffusion coefficient. Both single-crystal and polycrystalline hosts were used. It was shown that diffusion is faster in polycrystalline samples than in single crystals below 910 °C probably due to the enhancement of diffusion along grain boundaries [85]. For temperatures above 910 °C, diffusion speed was similar in both cases due to the grain growth process observed in polycrystalline samples at temperatures above ~900 °C [85]. Both sputtered films and CrSe powders were used as the dopant source, and diffusion was observed to be faster with CrSe powder than with sputtered metallic chromium for temperatures higher than 850 °C [85]. In a recent work, thermal diffusion process in ZnSe single crystals was studied between 800 and 1000 °C by using sputtered metallic chromium layers [120].

In our work, we used the model discussed in Section 2.3, to determine the diffusion coefficient for Cr^{2+} ions (from CrSe powder source) in the polycrystalline ZnSe host between 900 and 1100 °C [99]. We used the model to investigate the time and position dependence of the absorption coefficient in the diffusion-doped samples. As an example, Fig. 2.20 shows the calculated variation of α_{av} as a function of the radial coordinate r, for three different values of the diffusion coefficient ($5x10^{-11}$, $9x10^{-10}$, and $3x10^{-9}$ cm^2/s). Here the crystal was assumed to have a cylindrical shape with L=2.1 mm, and R=5 mm, and $n_o\sigma_o$ was chosen to be 10000 cm^{-1}. The diffusion time was 10 days. Figure 2.20 clearly shows how the strength of thermal diffusion influences the transverse homogeneity of the samples. In particular, we see that an increase in D reduces the size of the central homogeneously doped section of the samples.

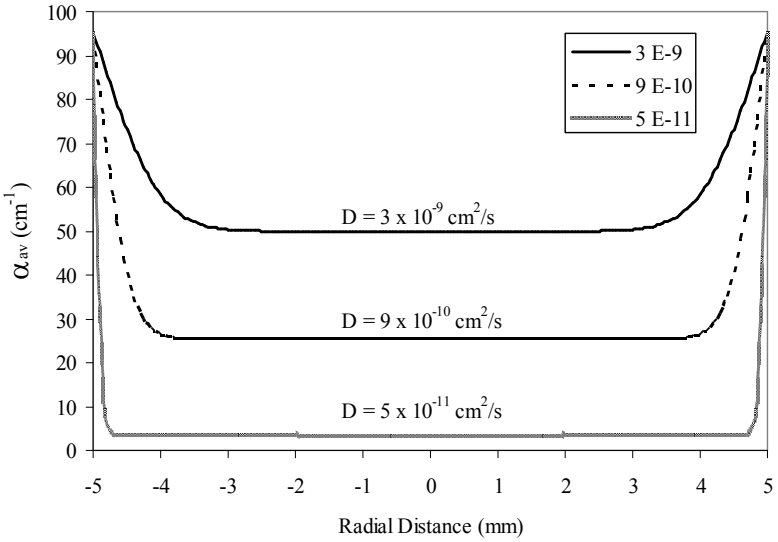

Figure 2.20. Calculated variation of the average absorption coefficient α_{av} as a function of the radial coordinate r, for three different values of the diffusion coefficient ($5x10^{-11}$, $9x10^{-10}$, and $3x10^{-9}$ cm^2/s). The crystal was assumed to have a cylindrical shape with L=2.1 mm, and R=5 mm, and $n_o\sigma_o$ was chosen to be 10000 cm^{-1}. The diffusion time was 10 days.

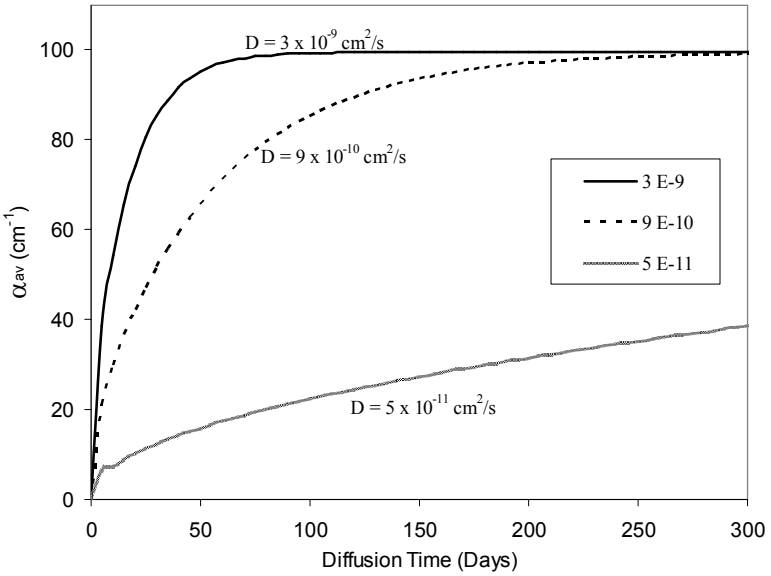

Figure 2.21. Calculated variation of the average absorption coefficient α_{av} at the center of samples as a function of the diffusion time, for three different values of the diffusion coefficient ($5x10^{-11}$, $9x10^{-10}$, and $3x10^{-9}$ cm^2/s). The crystal was assumed to have a cylindrical shape with L=2.1 mm, and R=5 mm, and $n_o\sigma_o$ was chosen to be 10000 cm^{-1}.

Fig. 2.21 further shows the calculated variation of α_{av} at the center of samples as a function of diffusion time, for the same values of diffusion coefficient and crystal dimensions. As the value of D increases the diffusion time required to reach the maximum attainable absorption coefficient decreases. The trends displayed in Fig. 2.20 and 2.21 suggest two alternative methods for the determination of diffusion coefficients from experimental absorption data. One method involves the measurement of the absorption coefficient at the center of the crystals subjected to different diffusion times at the same temperature. Or, alternatively, position-dependent absorption measurements can be performed by using a single sample. Both of these methods were employed to determine D.

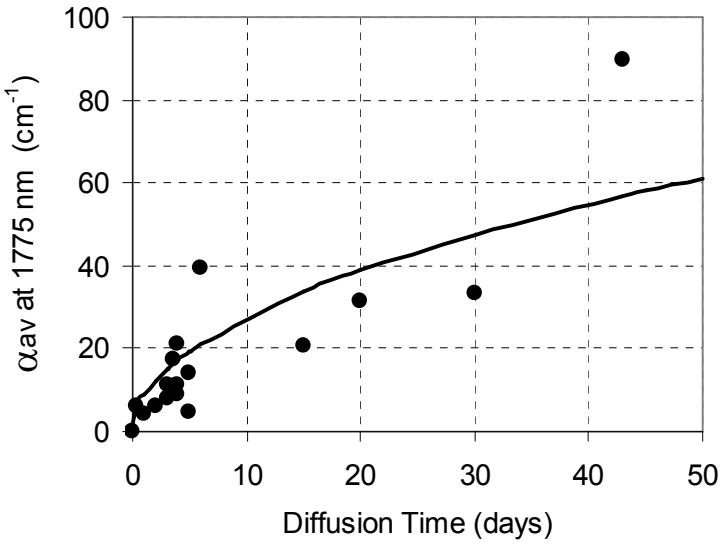

Figure 2.22. Measured variation of the peak absorption coefficient at the sample center as a function of the diffusion time for several Cr^{2+}:ZnSe samples. All the samples were prepared at 1000 °C. The solid curve is the best theoretical fit based on the diffusion model.

In the first method, the average absorption coefficient at the center of the cylindrical Cr^{2+}:ZnSe samples was measured as a function of the diffusion time. Sixteen samples prepared at 1000 °C for different diffusion times were used. Figure 2.22 shows the measured variation of the average absorption coefficient (α_{av}) at 1775 nm as a function of the diffusion time. Least-squares fit between the experimental data and the diffusion model gave the best value of $6x10^{-10}$ cm^2/s for D.

The diffusion coefficient determined in our study is lower than the previously reported values [85], possibly due the variation in the quality of the host samples.

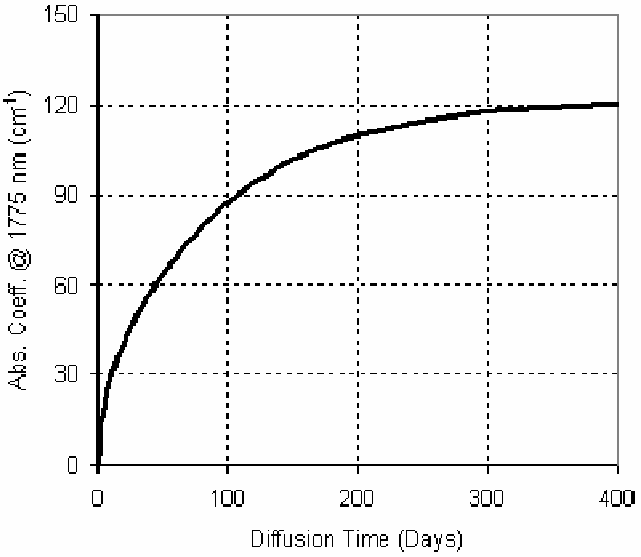

Figure 2.23 Predicted variation of the average absorption coefficient as a function of diffusion time based on the best-fit values (1775 nm).

Best-fit values of n_o and D can be used to predict the maximum possible absorption coefficient that can be obtained by diffusion doping of chromium. As can be seen from Fig. 2.23, our calculations predict that at a diffusion temperature of 1000 ºC, samples with absorption coefficient of up to 115 cm^{-1} (1775 nm) can be obtained, corresponding to an average chromium concentration of 8 x 10^{19} ions/cm^3.

We also used a second method which allows the determination of the diffusion coefficient with one sample only. In this case, a Cr:YAG laser operating at 1510 nm was used to measure the spatial variation of the absorption coefficient inside the sample. In these experiments, the output beam of the Cr:YAG laser was focused to a 20-µm spot and scanned across the sample cross section. Figure 2.24 shows the measured and calculated variation of the average absorption coefficient (α_{av}) as a function of the radial distance for a Cr^{2+}:ZnSe sample subjected to diffusion at 1000 ºC for 10 days. Note that this measurement also gives information on the spatial uniformity of the Cr^{2+}:ZnSe

samples prepared by thermal diffusion doping. For the specific sample in Fig. 2.24, spatially uniform section of the sample extends over 65 % of the total sample cross section. Using this method, best-fit between experiment and theory was obtained for a D value of 5.45x 10^{-10} cm^2/s, in good agreement with the result of 6x10^{-10} cm^2/s obtained above. The average diffusion coefficient determined at 1000 °C (5.7x10^{-10} cm^2/s) in our study is lower than the previously reported values [85, 120], possibly due the variation in the properties of the host samples.

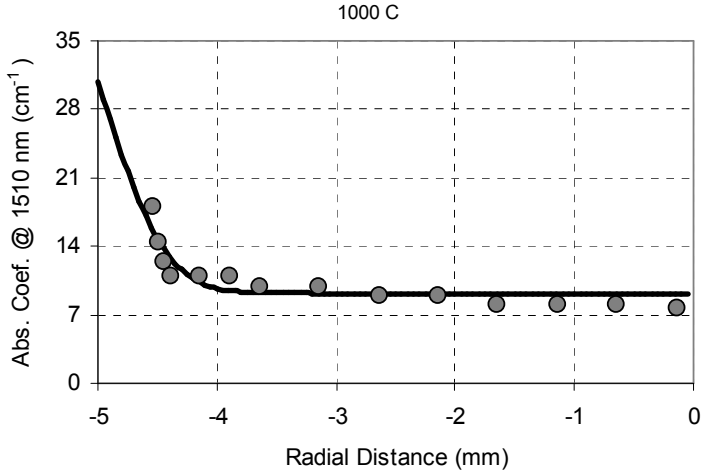

Figure 2.24. Measured and calculated variation of the absorption coefficient as a function of the radial distance in the Cr^{2+}:ZnSe sample. The sample was subjected to diffusion for 10 days at 1000 °C. The thickness and radius are 2 mm and 5 mm, respectively.

We also used Cr^{2+}:ZnSe samples prepared at 800 and 1100 °C to investigate the temperature dependence of the diffusion coefficient. Figures 2.25 to 2.27 shows the measured and calculated variation of the average absorption coefficient (α_{av}) as a function of the radial distance for the three Cr^{2+}:ZnSe sample subjected to diffusion at 800, 900 and 1100 ºC for 5 days, respectively. Figure 2.28 shows the variation of the best-fit value of the diffusion coefficient as a function of diffusion temperature between 800 and 1100 ºC. As expected the diffusion rate increases with increasing diffusion temperature. The variation of diffusion coefficient with temperature can be modeled by using the Arrhenius equation

$$D(T) = D_0 Exp\left(-\frac{E_{ad}}{k_b T}\right) \tag{2.11}$$

where D_0 is the value of the diffusion coefficient at very high temperatures and E_{ad} is the activation energy [85, 120]. Best fit between the experimentally determined diffusion coefficient values and Eq. 2.11 gave a value of 1.9×10^{-6} cm^2/s for D_0 and 0.9 eV for the activation energy. Note that there are large variations in the D_0 and E_{ad} values reported in literature [85, 120].

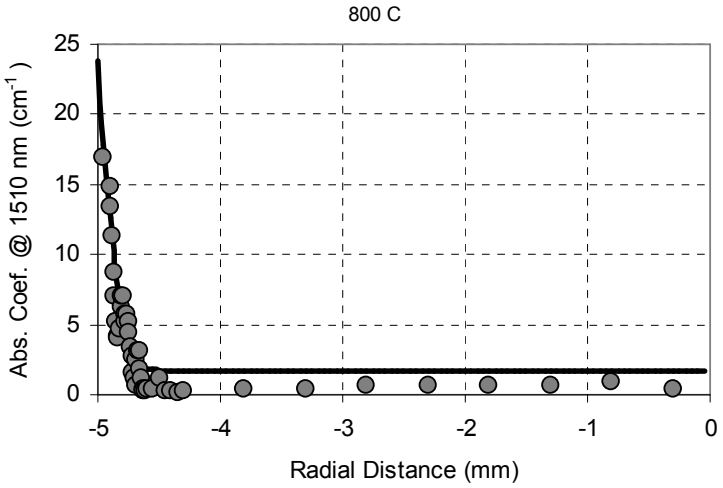

Figure 2.25. Measured and calculated variation of the absorption coefficient as a function of the radial distance in the Cr^{2+}:ZnSe sample. The sample was subjected to diffusion for 5 days at 800 °C. The thickness and radius are 2 mm and 5 mm, respectively.

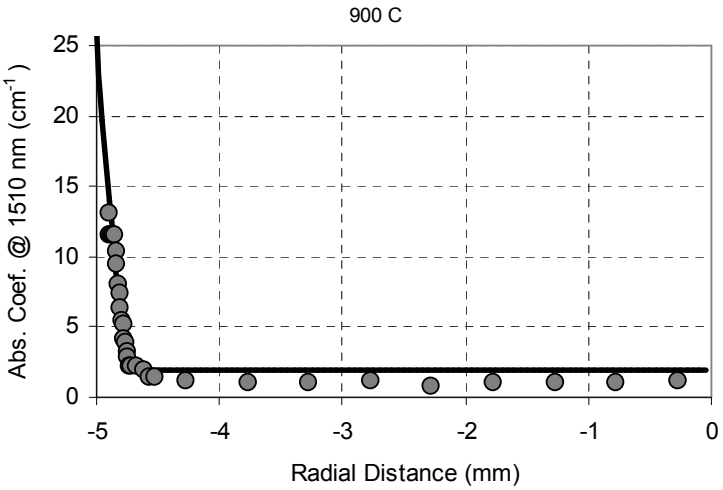

Figure 2.26. Measured and calculated variation of the absorption coefficient as a function of the radial distance in the Cr^{2+}:ZnSe sample. The sample was subjected to diffusion for 5 days at 900 °C. The thickness and radius are 2 mm and 5 mm, respectively.

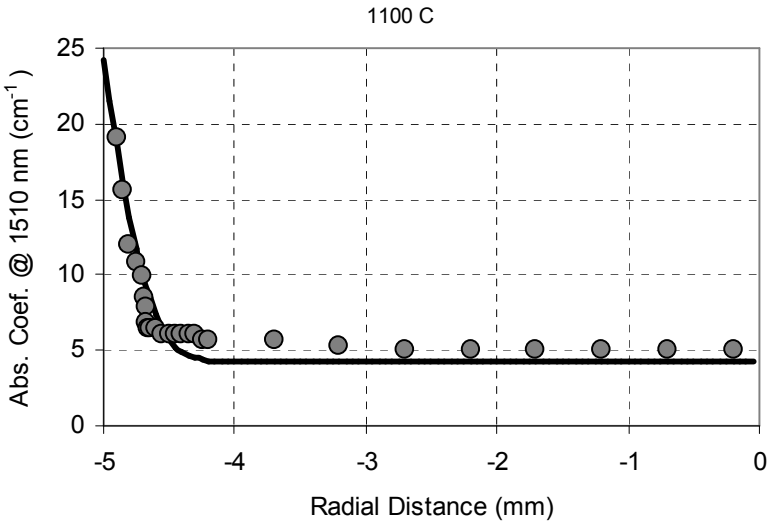

Figure 2.27. Measured and calculated variation of the absorption coefficient as a function of the radial distance in the Cr^{2+}:ZnSe sample. The sample was subjected to diffusion for 5 days at 1100 °C. The thickness and radius are 2 mm and 5 mm, respectively.

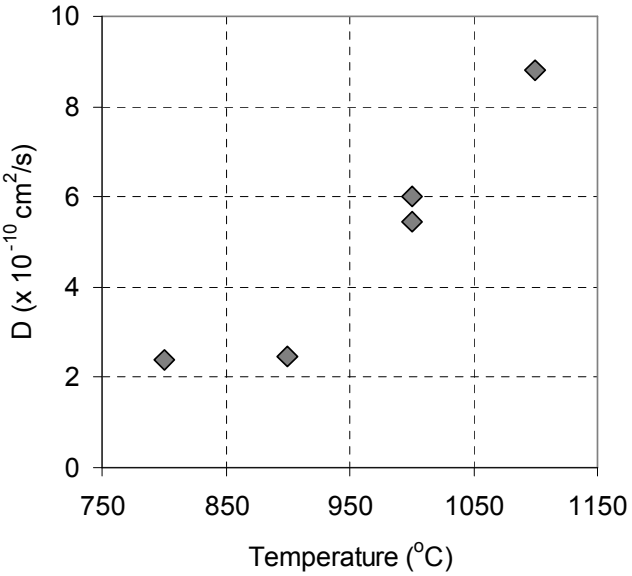

Figure 2.28. Temperature dependence of the diffusion coefficient D for the diffusion of Cr^{2+} into polycrystalline ZnSe between 800 and 1100 °C.

Chapter 3

FLUORESCENCE SPECTROSCOPY OF CR^{2+}:ZNSE

In this Section, we review the fluorescence properties of the Cr^{2+}:ZnSe medium. In particular, we present data that show how the lifetime and the fluorescence efficiency vary with the active ion concentration. An empirical fit is also obtained for the concentration dependence of the lifetime. We further discuss the models used for the determination of the absorption cross section from cw and pulsed absorption saturation measurements. Since lifetime data are needed in the cw analysis of saturation, we included this discussion on the modeling of saturation after Section 3.3.

3.1 Fluorescence Spectrum of Cr^{2+}:ZnSe

3.1.1 Fluorescence Spectrum Setup

Figure 3.1 shows the experimental setup used in fluorescence measurements. Fluorescence measurements were carried out with two different pump sources: a home-built cw Cr^{4+}:YAG laser operating at 1510 nm and a commercial thulium-doped fiber laser (IPG) at 1800 nm. In each case, the pump beam was focused at the center of the Cr^{2+}:ZnSe samples to a spot size of around 50 μm using a converging lens (L1, focal length=5 cm). The pump beams were also chopped to provide reference signal for lock-in detection. In the fluorescence measurements, the incident powers from the Cr^{4+}:YAG and thulium-doped fiber lasers were 40 mW and 0.5 W, respectively. The emitted fluorescence was collected with a concave gold mirror (diameter=7.6 cm, f=7.6 cm) and imaged at the entrance slit of a 0.5-m Czerny-Turner type monochromator, after passing through a high-pass optical filter that blocked the pump radiation. The fluorescence signal was detected with a PbS

detector and amplified in two stages by using a preamplifier and a lock-in amplifier. Figure 3.2 shows a photograph of the fluorescence measurement setup.

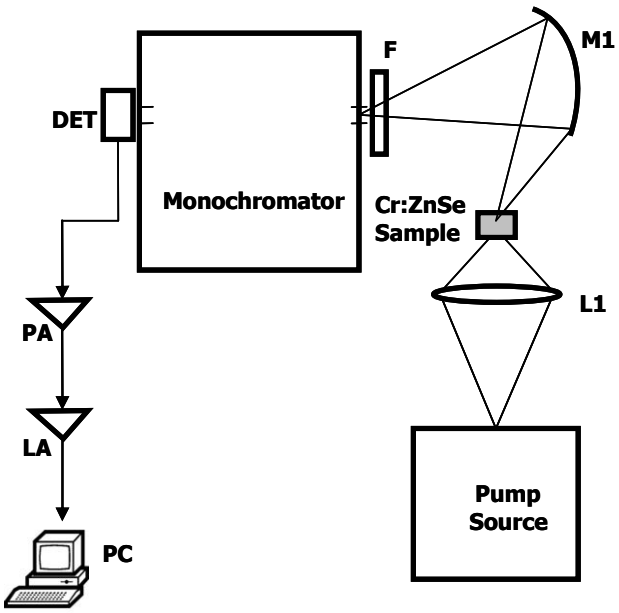

Figure 3.1 Experimental setup used in the fluorescence measurements.

Figure 3.2 Photograph of the fluorescence measurement setup.

3.1.2 Experimental Results

When the Cr^{2+}:ZnSe gain medium is excited by using optical sources operating between 1500 and 2100 nm ($^5T_2 \rightarrow {}^5E$ excitation), efficient, Stokes-shifted fluorescence can be obtained in the 2-3 μm wavelength range. Figure 3.3 shows the emission spectrum of Cr^{2+}:ZnSe samples excited at 1510 nm by a cw Cr^{4+}:YAG laser. The Cr^{2+}:ZnSe samples have the concentrations of $3x10^{18}$ ion/cm^3 (sample a) and $14x10^{18}$ ion/cm^3 (sample b) with peak absorption coefficients of 3.4 cm^{-1} and 16 cm^{-1}, respectively, at 1775 nm. Samples showed wide emission between 1.7 and 3.1 μm. Note that due to the self absorption of the medium between 1.5 and 2.1 μm, emission intensity on the low-wavelength side of the spectrum is reduced for sample b. This suggests that samples with relatively low chromium concentration are more suitable to obtain lasing in the low-wavelength end of the emission band. Experiments aimed at operating a gain-switched Cr^{2+}:ZnSe laser below 2000 nm are further discussed in Section 4.3. We also note in passing that even ultraviolet (355 nm) and visible (532 nm) pump sources can be used to obtain mid-infrared emission from Cr^{2+}:ZnSe [121]. The details of this indirect excitation mechanism and a discussion of lasing at 2.4 μm under 532-nm excitation can be found in Ref. [121].

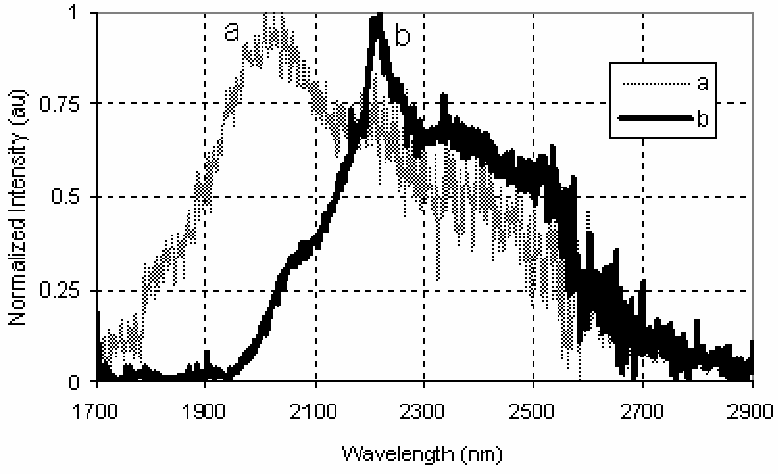

Figure 3.3. Measured emission spectra of two Cr^{2+}:ZnSe samples with concentrations of a) $3x10^{18}$ ion/cm^3 and b) $14x10^{18}$ ion. The samples were excited at 1510 nm using a cw Cr^{4+}:YAG laser.

The stimulated emission cross section σ_e is an important laser parameter which is related to the strength of the emission band and the amount of optical amplification that can be obtained from the gain medium. σ_e can be determined from the fluorescence spectrum by using the Fuchtbauer-Ladenburg formula [18, 88, 122]:

$$\sigma_{em}(\lambda) = \frac{\lambda^5}{8\pi c n^2 \tau_{rad} \int_{band} \lambda I_e(\lambda) d\lambda} I_e(\lambda). \quad (3.1)$$

Here, c is the speed of light, n is the index of refraction, τ_{rad} is the radiative lifetime, and $I_e(\lambda)$ is the spectral distribution of the fluorescence intensity. The emission data for the sample with lower chromium concentration (sample a) can be used to determine $I_e(\lambda)$. In our analysis the refractive index n and the radiative lifetime τ_{rad} were taken as 2.45 and 5.5 μs for Cr^{2+}:ZnSe, respectively [123, 124], yielding a peak emission cross section of $13x10^{-19}$ cm^2 at 2050 nm. This is in good agreement with the previously reported values [14, 44, 122, 125, 126]. However, the peak of the observed emission spectrum was at a lower wavelength (around 2050 nm) compared to the emission peaks reported in the literature, probably due to the difference in pumping wavelengths used in excitation and the effect of reabsorption on the emission curve [14, 30, 122, 127].

3.2 Temperature and Concentration Dependence of the Fluorescence Lifetime

3.2.1 Theoretical Background

In general, the total fluorescence decay rate of an energy level is the sum of the radiative (W_{rad}) and nonradiative ($W_{non\text{-}rad}$) decay rates. The experimentally measured fluorescence lifetime (τ_f) is related to W_{rad} and $W_{non\text{-}rad}$ through

$$\frac{1}{\tau_f} = \frac{1}{\tau_{rad}} + \frac{1}{\tau_{non-rad}} = W_{rad} + W_{non-rad}, \quad (3.2)$$

where τ_{rad} is the radiative lifetime and $\tau_{non\text{-}rad}$ is the inverse of the non-radiative decay rate $W_{non\text{-}rad}$. As $W_{non\text{-}rad}$ increases, the fluorescence lifetime of the sample decreases and a larger fraction of the input pump energy is converted into heat.

For transition metal ions, a significant portion of the nonradiative decay is via direct multiphonon relaxation [30, 47]. The rate of multiphonon relaxation (W_m) for a gain medium depends both on the dopant ion and the host, and scales exponentially as

$$W_m \propto \mathrm{Exp}\left(-\beta\frac{\Delta E}{\hbar\omega}\right) = \mathrm{Exp}(-\beta p) \tag{3.3}$$

where ΔE is the bandgap energy between ground and excited state energy levels, $\hbar\omega$ is the phonon energy, and β is a constant [47, 128, 129]. The ratio of ΔE to $\hbar\omega$ is generally expressed as p, and it is the number of phonons necessary to bridge the energy gap between the levels. Note that as p increases, the nonradiative transition rate become insignificant. The temperature dependence of nonradiative decay rate due to multiphonon relaxation (W(T)) can be modeled using

$$W(T) \approx W(T=0)\left(\frac{\mathrm{Exp}(\frac{h\omega}{k_B T})}{\mathrm{Exp}(\frac{h\omega}{k_B T})-1}\right)^p \tag{3.4}$$

where W(T=0) is the nonradiative decay rate at low temperature, k_B is Boltzman constant and T is the temperature [129]. Here note that W(T=0) is an exponentially decreasing function of p (Eq. 3.3). Due to the exponential temperature-dependent nature of multiphonon relaxation process described by Eq. 3.4, as the temperature increases multiphonon relaxation rate increases.

Before closing this part, we note that besides the multiphonon relaxation process mentioned above as a nonradiative decay process, there is also a thermally activated nonradiative decay process observed in transition metals ions due to strong coupling between the electrons on the optically active ion and the lattice vibrations of the host [30, 129]. The rate of this process heavily depends on the ratio of the shift of the higher lying energy level with respect to the ground state in the configuration-coordinate diagram [44, 128]. This shift in configuration-coordinate diagram is observed because ions in the ground and excited electronic state oscillate about different equilibrium positions [128]. Due to this shift in configuration-coordinate diagram the peak of the emission curve was at a longer wavelength than the absorption peak (Stokes shift). Generally speaking, thermally activated nonradiative decay process is effective if the ratio of the Stokes shift

(E_{stokes}) to the bandgap energy (ΔE) between the energy levels (E_{stokes} /ΔE) is higher than 0.5 [128]. The rate of this decay process also scales exponentially with increasing temperature [44].

An important parameter that influences the power efficiency of a solid-state laser is the fluorescence quantum efficiency, which is the ratio of the fluorescence lifetime (τ_f) to the radiative lifetime (τ_{rad}). This parameter (τ_f/τ_{rad}) measures the fraction of the input pump energy that can be converted to laser emission. As noted earlier, Cr^{2+}:ZnSe attracted a lot of attention because at low doping densities, it has a near-unity fluorescence quantum efficiency near room temperature. This is quite rare in TM-doped tunable solid-state lasers. Near-unity quantum efficiency at room temperature further suggests that both the multiphonon relaxation and thermally activated nonradiative decay processes are negligible in Cr^{2+}:ZnSe at room temperature [30, 44, 47, 128, 129]. Here, we also note that the reduced role of multiphonon relaxation is due to the low phonon cutoff energy (250 cm^{-1} in ZnSe) of the medium [2].

3.2.2 Concentration Dependence of the Fluorescence Lifetime

As the doping concentration is increased, ion-ion interactions can also increase the strength of non-radiative decay processes, leading to a reduction in fluorescence quantum efficiency [128]. In this Section, we discuss the experiments performed in our group to investigate the concentration dependence of the fluorescence lifetime.

Experimental setup used in lifetime measurements is shown in Fig. 3.4. A pulsed optical parametric oscillator (OPO) operating at 1570 nm and producing 65-nsec pulses at a repetition rate of 1 kHz was used to excite the samples. A converging lens with a focal length of 5 cm was used to focus the output of the OPO into the Cr^{2+}:ZnSe samples. The fluorescence decay signal was separated from the OPO signal by using several high-pass filters and collected with a MgF_2 lens (focal length=8 cm) at 90° with respect to the direction of excitation beam. The time-dependent fluorescence decay signal was measured with a fast InGaAs detector that had extended spectral response up to 2.6 μm, and recorded with a digital sampling oscilloscope. The response time of the InGaAs detector was 3 n-sec. The detector was used with a built-in preamplifier. A photograph of the InGaAS detector and the amplifier is shown in Fig. 3.5.

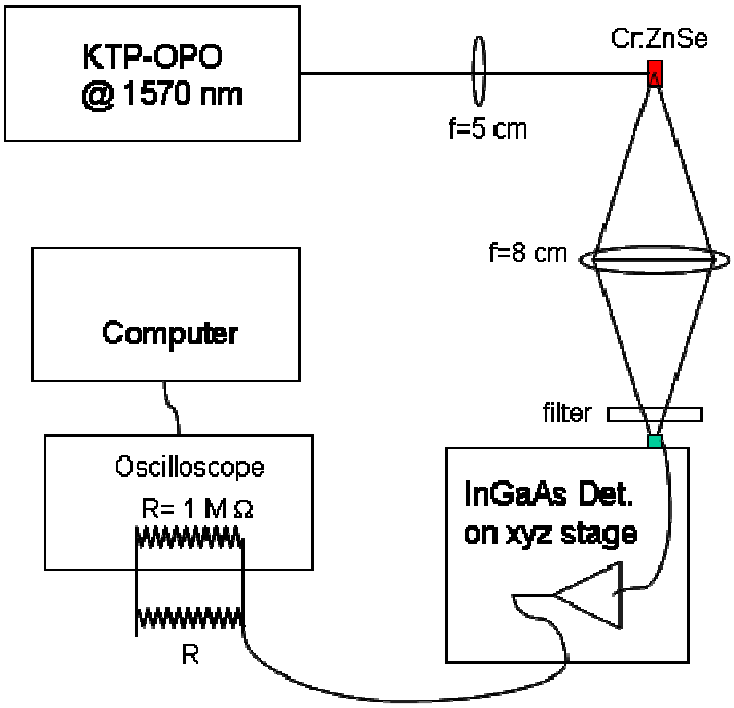

Figure 3.4. Experimental lifetime measurement setup for Cr^{2+}:ZnSe.

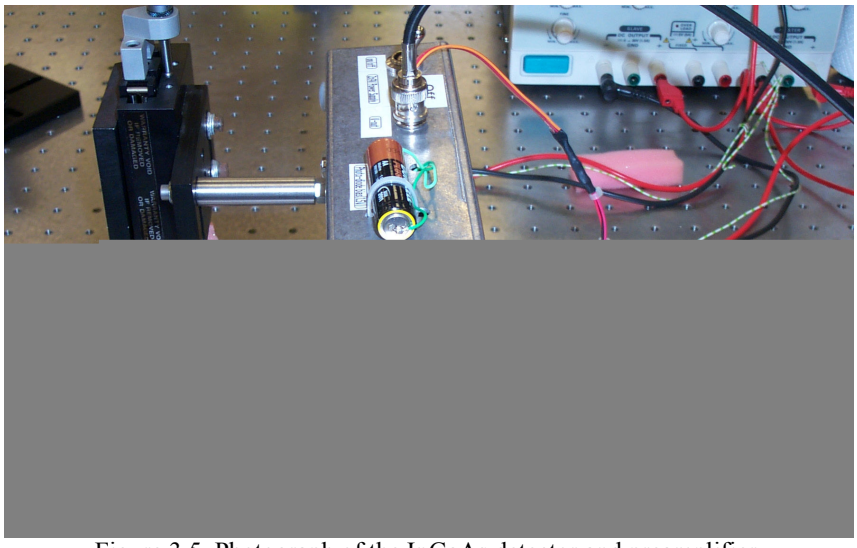

Figure 3.5. Photograph of the InGaAs detector and preamplifier.

As an example, Fig. 3.6 shows the room-temperature time-dependent fluorescence decay curve of a polycrystalline Cr^{2+}:ZnSe sample with a Cr^{2+} ion concentration of $9.5x10^{18}$ cm^{-3}. The corresponding peak absorption coefficient is 10.7 cm^{-1} at 1775 nm. The inset in Fig. 3.2 shows the variation of the natural logarithm of the fluorescence intensity. We note that the fluorescence signal shows a single-exponential decay (natural logarithm of the fluorescence intensity signal has only one slope). By doing a single-exponential fit to the experimental data, the fluorescence lifetime was determined to be 4.6±0.2 μs for this particular sample.

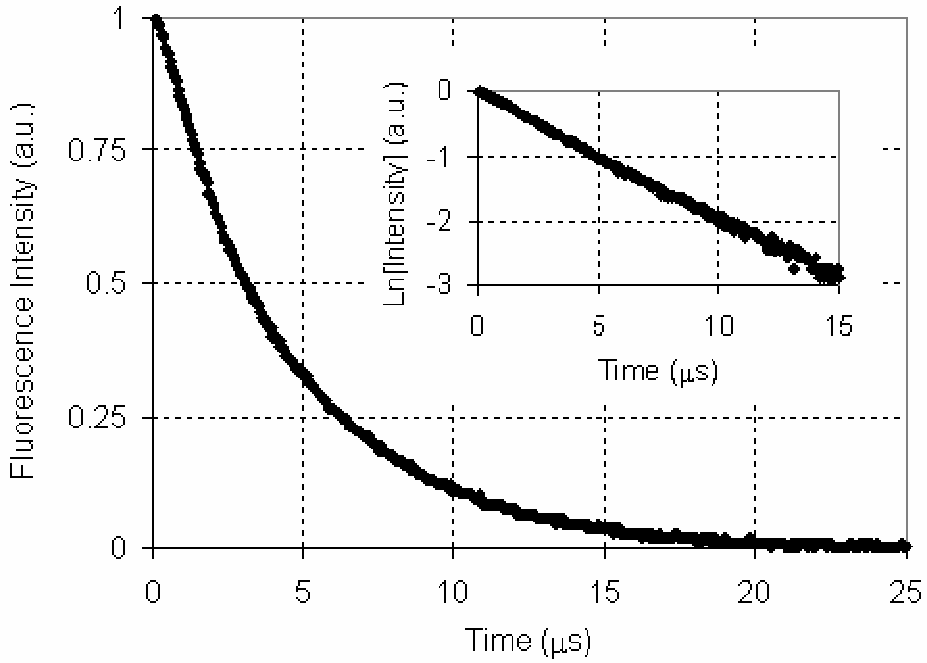

Figure 3.6. Room temperature time-dependent fluorescence decay of a Cr^{2+}:ZnSe sample with a concentration of $9.5x10^{18}$ cm^{-3}. The sample was excited with 65-ns-long pulses at 1570 nm. The inset shows the variation of the natural logarithm of the fluorescence intensity. The fluorescence lifetime was determined to be 4.6±0.2 μs.

The above measurement was repeated for various Cr^{2+}:ZnSe samples doped with different amounts of chromium. Figure 3.7 shows the measured variation of the fluorescence lifetime at room temperature as a function of the average chromium concentration. As can be seen, the

fluorescence lifetime shows a rapid decay with Cr^{2+} concentration due to concentration quenching. Similar decrease in the fluorescence lifetime with Cr^{2+} concentration was also observed in previous studies [81, 130, 131]. This observed decrease of fluorescence lifetime at higher concentrations can be explained by using the following argument [128]. As the active ion concentration in a material is increased, the possibility of the interaction between these active ions increases. Due to this interaction between the active ions, energy may transfer from an excited ion to the nearby ions in ground state (cross-relaxation). In concentrated materials this energy transfer process can be very efficient and allows the circulation of the energy inside the material. However, there are also nonradiative traps inside the gain materials and when the energy is transferred into these centers during this circulation, the energy will be lost. Due to the effectiveness of this energy transfer even trace amounts of traps inside the gain medium will cause severe decrease in fluorescence lifetime and efficiency. Fe^{2+} ions are a good example of such luminescent killer tracks in Cr^{2+}:ZnSe. Recently Kernal et al. showed efficient energy transfer from Cr^{2+} ions to Fe^{2+} in chromium and iron codoped ZnSe material [74].

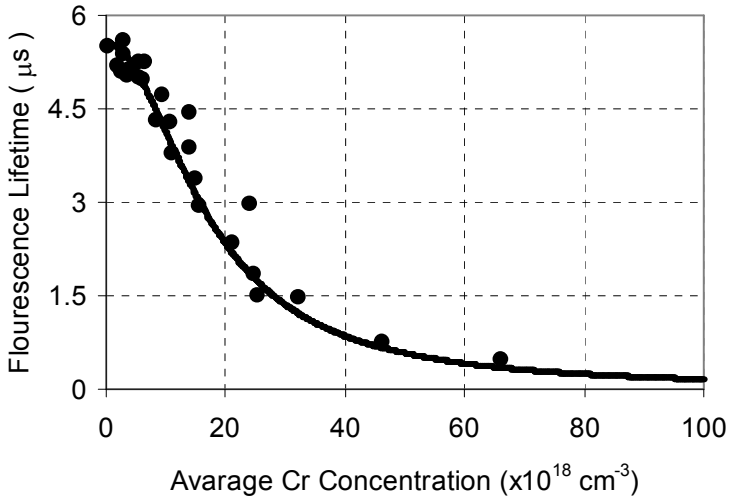

Figure 3.7. Measured variation of the fluorescence lifetime of polycrystalline Cr^{2+}:ZnSe as a function of the chromium concentration at room temperature. The solid line is the empirical fit given by Eq. 3.5 in the text.

The concentration dependence of the fluorescence lifetime τ_f can be described by an empirical formula of the form

$$\tau_F = \frac{\tau_{F0}}{1+\left(\frac{N_{Cr}}{N_0}\right)^2}, \qquad \text{(Eq. 3.5)}$$

where N_{Cr} is the chromium concentration, τ_{F0} is the low-concentration value of the fluorescence lifetime, and N_0 is the concentration where τ_F is reduced to $\tau_{F0}/2$. The solid line in Fig. 3.7 shows the least-squares fit to the experimental lifetime data by using Eq. 3.5. The best-fit values of τ_{F0} and N_0 were determined to be 5.56 μs and $17x10^{18}$ ions/cm^3, respectively. $N_0=17x10^{18}$ ions/cm^3 corresponds to a peak absorption coefficient of 19.5 cm^{-1} at 1775 nm. τ_{F0} values reported by other groups are in the 5-7 μs range [81, 122, 124, 131]. The observed variation may be due to the difference in the structural properties of the ZnSe host. The value of N_0 measured in our study ($17x10^{18}$ ions/cm^3) is also lower than those obtained in other studies (~$25x10^{18}$ ions/cm^3 [124, 130], ~$26x10^{18}$ ions/cm^3 [131], ~$30x10^{18}$ ions/cm^3 [81]). Despite the variation in the reported values of N_0 and τ_{F0}, we see clearly that the concentration dependence of the lifetime is relatively weak for concentrations lower than $10x10^{18}$ ions/cm^3 (see Fig. 3.3 and Refs. [81, 124, 130]). This value of concentration (~$10x10^{18}$ ions/cm^3) appears as the critical concentration where ion-ion interactions and non-radiative decay processes start to become effective. We can hence conclude, based on the lifetime measurements, that samples with chromium concentrations lower than about $10x10^{18}$ ions/cm^3 (peak absorption coefficient=11.5 cm^{-1} at 1775 nm) are more suitable for laser applications, especially in the cw regime.

3.2.3 Temperature Dependence of the Fluorescence Lifetime

Data on the temperature dependence of the fluorescence lifetime gives very useful information about the strength of multiphonon relaxation processes at different temperatures. In Cr^{2+}:ZnSe, the temperature dependence of the fluorescence lifetime was investigated by several groups [14, 81, 88, 122, 130]. In some of the previous measurements, a slight increase in fluorescence lifetime was observed as the temperature was increased from cryogenic temperatures to room temperature [14,

44, 122]. The reason for this increase remained unclear and several explanations were offered [14, 122]. In a recent work, Kisel et al. suggested that the observed increase in the fluorescence lifetime may be attributed to reabsorption in the bulk of the samples [124]. In support of this, the temperature dependence of the fluorescence lifetime was measured by using the luminescence from the surface and the bulk of Cr^{2+}:ZnSe samples. Insignificant increase in the fluorescence lifetime was observed with temperature when the fluorescence signal was collected from sample surface, in comparison with what was taken from the bulk of the samples.

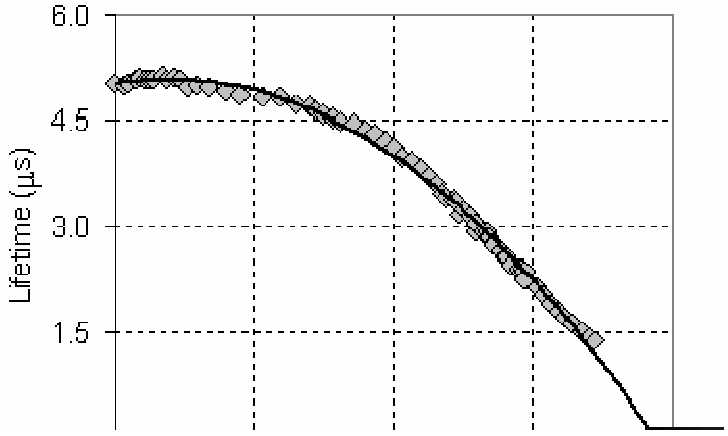

Figure 3.8. Measured variation of the fluorescence lifetime for a Cr^{2+}:ZnSe sample with a Cr^{2+} concentration of 5.7 x10^{18} ions/cm^3 between 0 and 150 °C

In our studies, we characterized the temperature dependence of the fluorescence lifetime at elevated temperatures between 0 and 160 °C. Such data provide useful information for the design of power-scalable Cr^{2+}:ZnSe lasers since the unused pump power can lead to thermal gradients inside the gain medium, and reduce the population inversion due to the temperature dependence of the fluorescence lifetime. Figure 3.8 shows the experimentally measured variation of the fluorescence lifetime as a function of temperature between 0 and 160 °C for a Cr^{2+}:ZnSe sample with a Cr^{2+} concentration of 5.7 x10^{18} ions/cm^3 (peak absorption coefficient =6.5 cm^{-1} at 1775 nm). A sharp

decrease in the fluorescence lifetime was observed above 60 °C similar to the results of other studies [14, 81, 88, 122, 130]. An empirical polynomial fit to the data shows that the fluorescence lifetime $\tau_F(T)$ can be estimated from

$$\tau_F(T) = \tau_{RT}\left(1 + 0.00166\,T - 0.000052\,T^2\right), \qquad \text{(Eq. 3.6)}$$

where τ_{RT} is the fluorescence lifetime of the sample at room temperature and T is the temperature in degrees Celsius. The solid line in Fig. 3.8 is the best fit to the experimental data based on Eq. 3.6 with τ_{RT} =5 μs.

3.3 Dependence of the Fluorescence Efficiency on Chromium Concentration

A direct consequence of the concentration dependence of the fluorescence lifetime is a reduction in the fluorescence efficiency in Cr^{2+}:ZnSe with increasing active ion concentration. As a result, the population inversion of the upper laser level for a given pump power decreases and the cw lasing threshold increases. In our studies, we have directly measured the effect of the ion concentration on the fluorescence quantum efficiency in Cr^{2+}:ZnSe.

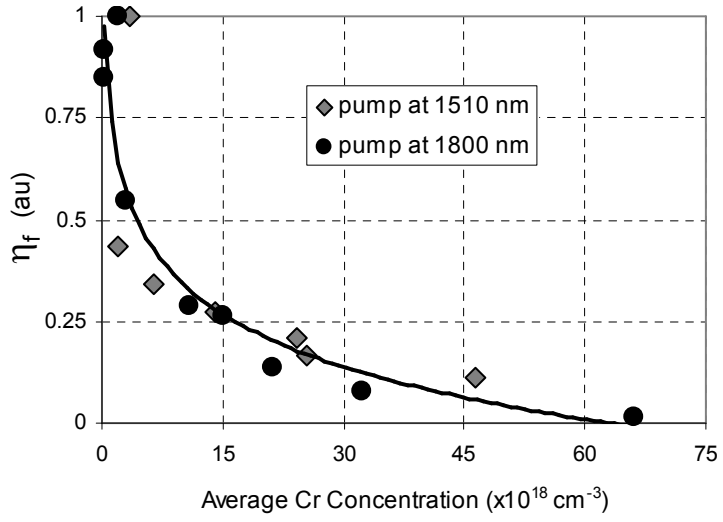

Figure 3.9. Variation of the fluorescence efficiency in Cr^{2+}:ZnSe samples at 2400 nm as a function of the chromium concentration. Two different pump sources (a Cr:YAG laser at 1510 nm and a Tm-fiber laser at 1800 nm) were used.

Figure 3.9 shows the measured variation of fluorescence efficiency (η_F) as a function of Cr^{2+} concentration at 2400 nm. Fluorescence efficiency η_F at 2400 nm is defined as

$$\eta_F = \frac{I_{2400}}{P_{abs}}, \qquad \text{(Eq. 3.7)}$$

where I_{2400} is the measured fluorescence intensity at 2400 nm and P_{abs} is the absorbed pump power at the excitation wavelength. Measurements were performed by using a Cr:YAG laser at 1510 nm and a Tm-fiber laser at 1800 nm. Results showed a monotonic decrease in the fluorescence efficiency with increasing Cr^{2+} concentration. The observed decrease in η_F (Fig. 3.9) is sharper than that for the fluorescence lifetime (Fig. 3.7). This may be attributed to the presence of higher passive losses at the lasing wavelength in more heavily doped samples, as explained in Section 2.5.

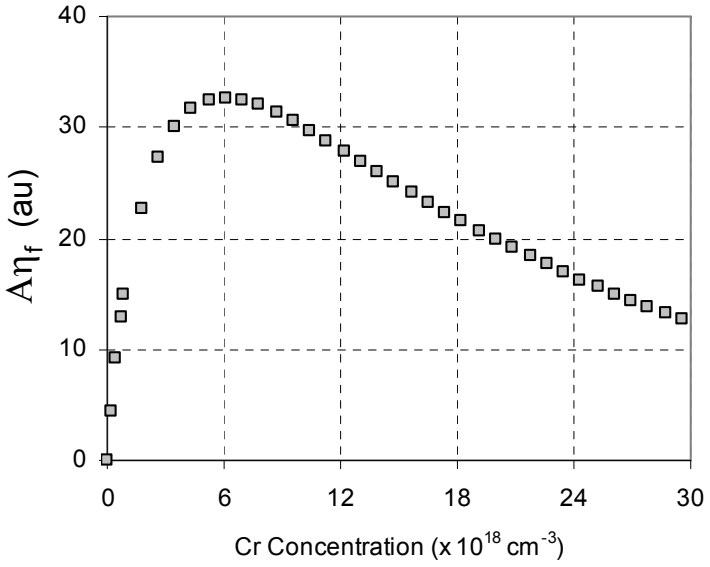

Figure 3.10: Estimated variation of $A\eta_f$ (A=Absorption, η_f =flouresence efficiency) for a 2-mm thick Cr^{2+}:ZnSe gain medium as a function of chromium concentration.

Based on the fluorescence efficiency data, it is possible to estimate the optimum chromium concentration where the emitted photons at the lasing wavelength will be maximized. Note that η_F gives the fraction of the absorbed pump power that is converted to photons at the emission

wavelength. By multiplying η_F with the total absorption A of the sample, we obtain a fraction which is proportional to the total number of photons at the emission wavelength. Note that the total absorption $A = 1 - \exp(-\sigma_a N_{Cr} l)$ (σ_a=absorption cross section, N_{Cr}=chromium concentration, and l=sample length) increases with ion concentration N_{Cr} and tends to unity at large N_{Cr}. Figure 3.10 shows the calculated variation of $A\eta_F$ for a 2-mm thick Cr^{2+}:ZnSe sample by taking σ_a=11.5x10^{-19} cm^2 [10]. As can be seen from Fig. 3.10, this simple analysis shows that the fluorescence intensity for Cr^{2+}:ZnSe will be maximum in a sample with an average chromium concentration of about 6x10^{18} ions/cm^3. We note here that the optimum chromium concentration will also depend on the chosen sample length. The result obtained here is for the specific case of l=2 mm.

3.4 Determination of Absorption Cross Sections

3.4.1 Model Equations

If the active ion density N_{Cr} inside the Cr^{2+}:ZnSe medium is accurately known, the absorption cross section $\sigma_a(\lambda)$ at the wavelength λ can be readily determined from

$$\sigma_a(\lambda) = \frac{\alpha_{p0}(\lambda)}{N_{Cr}}, \tag{3.8}$$

where the small-signal absorption coefficient $\alpha_{p0}(\lambda)$ is typically measured with a spectrophotometer as described before in Section 2.4. If N_{Cr} is not accurately known, absorption saturation measurements can instead be employed in the determination of $\sigma_a(\lambda)$. In this case, a laser whose operating wavelength λ overlaps with the absorption band of the medium is required. The transmission of the sample is measured as a function of the input power or input energy depending on whether a cw or a pulsed source is used, respectively. Alternatively, the input power or energy is kept fixed and the transmission is measured as a function of the pump beam waist location (z-scan method). Below, we employ the rate-equation formalism [132] to analyze the saturation characteristics of an absorber for the cw and pulsed cases and describe how $\sigma_a(\lambda)$ can be determined from the measured data. We model the Cr^{2+}:ZnSe medium as a modified 4-level system with the possibility of excited-state absorption. Transverse intensity variations across the beam

cross section are also taken into account. As we will point out, knowledge of the fluorescence lifetime is necessary in order to determine $\sigma_a(\lambda)$ from the cw saturation measurements.

3.4.2 Continuous-Wave Case

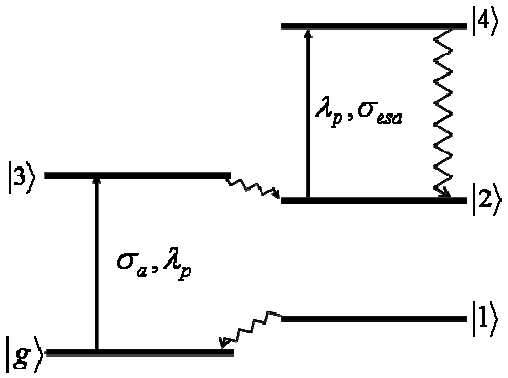

Figure 3.11: Energy level diagram for Cr^{2+}: ZnSe medium, with the possibility of excited state absorption at the pump wavelength.

In the case of cw saturation, we derive the differential equation satisfied by the beam power during propagation through the saturable absorber. A schematic of the energy-level diagram is shown in Fig. 3.11. Spectroscopic designations of the energy levels are not used in order to keep the analysis general. Let us suppose that pump photons at the wavelength of λ_p are incident on the absorber. If λ_p overlaps with the absorption band, absorber ions will be raised from the ground state $|g\rangle$ to the first excited-state $|3\rangle$. We assume that fast non-radiative decay of the excited ions then takes place to the upper level $|2\rangle$. In the case of Cr^{2+}:ZnSe, level $|2\rangle$ is the upper laser level from which ions decaying via stimulated emission produce laser radiation around 2.5 μm. In the analysis of the saturable absorber, we neglect stimulated emission and only consider spontaneous emission to the lower level $|1\rangle$. Finally, fast non-radiative decay brings the ions back to the ground state $|g\rangle$. Typically, the non-radiative decay rates are extremely fast compared to spontaneous decay and populations of levels $|1\rangle$ and $|3\rangle$ may be neglected. We further assume that excited-state

absorption may occur from level $|2\rangle$ to a higher lying level $|4\rangle$ at the pump wavelength of λ_p and that once ions are excited to level $|4\rangle$, rapid nonradiative decay takes them back to level $|2\rangle$. In the following analysis, we drop the spatial and temporal dependence of the populations and intensities to simplify the notation. The population density N_2 of the upper level obeys the differential equation

$$\frac{\partial N_2}{\partial t} = \frac{\sigma_a \lambda_p I_p}{hc} N_g - \frac{N_2}{\tau_f}, \tag{3.9}$$

where h is Planck's constant, c is the speed of light, I_p is the intensity of the pump radiation at λ_p, σ_a is the ground state absorption cross section at λ_p, N_g is the population density of the ground state, and τ_f is the fluorescence lifetime.

As the pump beam propagates through a thin slab of the saturable absorber with cross-sectional area A and thickness dz, conservation of energy yields

$$\frac{\partial I_p}{\partial z} + \frac{1}{v_g}\frac{\partial I_p}{\partial t} = -\sigma_a I_p \left(N_g + f_p N_2\right). \tag{3.10}$$

Here, v_g is the group velocity of the pump beam, and f_p is the normalized strength of excited-state absorption at λ_p ($f_p = \sigma_{esa}/\sigma_a$, σ_{esa}=excited-state absorption cross section). Note that here, N_2+ N_g=N_{Cr} . In steady state, N_2 becomes

$$N_2 = N_{Cr}\frac{I_p/I_{sa}}{1 + I_p/I_{sa}}, \tag{3.11}$$

where I_{sa} is the absorption saturation intensity given by

$$I_{sa} = \frac{hc}{\sigma_a \lambda_p \tau_f}. \tag{3.12}$$

Note that the smaller the value of I_{sa}, the easier it will be to saturate the absorption. By using the steady-state expressions for N_2 and N_g, it can be shown that I_p will satisfy the differential equation

$$\frac{\partial I_p}{\partial z} = -\alpha_{p0} I_p \left[\frac{1 + f_p \frac{I_p}{I_{sa}}}{1 + \frac{I_p}{I_{sa}}} \right]. \tag{3.13}$$

Here, α_{p0} is the small-signal differential pump absorption coefficient defined in Eq. (3.8) above. If excited-state absorption is present, note from Eq. (3.13) that it is not possible to fully saturate the absorber even at very high pump intensities.

If the normalized transverse distribution Φ_P of the intensity is assumed to be cylindrically symmetric, then the beam power $P_p(z)$ at the location z satisfies

$$\frac{dP_p}{dz} = -\alpha_{p0} P_p \int dr\, 2\pi r \Phi_p \left[\frac{1 + f_p \frac{P_p \Phi_p}{I_{sa}}}{1 + \frac{P_p \Phi_p}{I_{sa}}} \right], \tag{3.14}$$

where r is the radial coordinate. As an example, Φ_P for a Gaussian beam is given by

$$\Phi_P = \frac{2}{\pi \omega_p^2} \exp\left(-\frac{2r^2}{\omega_p^2} \right), \tag{3.15}$$

where ω_p is the position-dependent pump spot-size distribution. The transmitted power will depend on the input power and the waist location of the pump spot-size function. Best fits can be made to experimental data by varying f_p and I_{sa}. From the values of the best-fit parameters, σ_a and σ_{esa} can be determined. To find σ_a, the fluorescence lifetime τ_f of the sample is also needed (see Eq. (3.12)).

3.4.3 Pulsed Case

As an alternative to the cw saturation measurements, a train of pulses can also be sent through the medium to measure the dependence of the transmission on input pulse energy and beam focusing. Here, we analyze the behavior of the saturable absorber by assuming that the duration of the pulses is much shorter than the fluorescence lifetime. We also assume that the absorber completely

recovers before the next pulse comes. The pulse intensity $I_p(t)$ and the integrated energy density $\overline{E}_p$ are related through

$$\int_{-\infty}^{\tau} dt I_p(t) = \overline{E}_p . \tag{3.16}$$

Here, τ is much greater than the pulsewidth so that to a very good approximation, $I_p(\tau) = 0$. By using Eqs. (3.9) and (3.10) and by neglecting spontaneous decay rates, we obtain

$$\frac{\partial I_p}{\partial z} + \frac{1}{v_g}\frac{\partial I_p}{\partial t} = (1 - f_p)\frac{hc}{\lambda_p}\frac{\partial N_g}{\partial t} - f_p \alpha_{p0} I_p . \tag{3.17}$$

If Eq. (3.9) is integrated from $t = -\infty$ to $t = \tau$, the ground state population N_g can be expressed in terms of the integrated energy density as

$$N_g = N_{Cr} \exp\left(-\frac{\overline{E}_p}{E_{sa}}\right), \tag{3.18}$$

where the initial ground-state population density is $N_g(-\infty) = N_{Cr} = \frac{\alpha_{p0}}{\sigma_a}$ and E_{sa} ($E_{sa}=hc/\sigma_a\lambda_p$) is the saturation fluence for absorption. If Eq. (3.17) is integrated from $t = -\infty$ to $t = \tau$, we obtain the differential equation that describes the spatial evolution of the energy density:

$$\frac{\partial \overline{E}_p}{\partial z} = -(1 - f_p)\alpha_{p0} E_{sa}\left[1 - \exp\left(-\frac{\overline{E}_p}{E_{sa}}\right)\right] - f_p \alpha_{p0} \overline{E}_p . \tag{3.19}$$

Finally, by assuming that the transverse energy distribution of the beam is described by Φ_p, we find that the total pulse energy E_p obeys

$$\frac{\partial E_p}{\partial z} = -(1 - f_p)\alpha_{p0} E_{sa} \int dr\, 2\pi r\left[1 - \exp\left(-\frac{E_p \Phi_p}{E_{sa}}\right)\right] - f_p \alpha_{p0} E_p . \tag{3.20}$$

In the analysis of saturation data, f_p and E_{sa} can be used as the fitting parameters to determine σ_a and σ_{esa}.

3.4.4 Experimental Results

In this section, we present the results of saturation measurements performed with a polycrystalline Cr^{2+}:ZnSe sample to determine the absorption cross section σ_a. In the measurements, a 1.85-mm-thick Cr^{2+}:ZnSe sample with a peak absorption coefficient of 12.2 cm^{-1} at 1775 nm and a fluorescence lifetime of 4.3 μ

negligible, in agreement with earlier work [124, 133-135]. The calculated absorption cross section values at 1570 nm and 1800 nm correspond to a peak absorption cross section of $5.6x10^{-19}$ and $6.1x10^{-19}$ cm^2 at 1775 nm (using Eq. 2.5), respectively. The agreement between these values obtained by using different techniques is reasonably good. The averaged best-fit value of the cross section at 1775 nm comes to 5.85 x 10^{-19} cm^2. Several other groups also determined the absorption cross section for Cr^{2+}:ZnSe. The results of these measurements along with the pump wavelengths used appear in Table 3.1. The best-fit average obtained in our studies is lower than the average ($\sim 10x10^{-19}$ cm^2) of the previously reported values shown in Table 3.1.

σ_o ($x10^{-19}cm^2$)	f_p	Pump Wavelength	Reference
~11	0	pulsed, 1534 nm	[124]
~7.5	-	pulsed, 2017 nm	[136]
~10	< 0.04	pulsed, 1598 nm	[133]
~9.5	-	cw, 2000 nm	[137]
~12	0	pulsed, 1534 nm	[134]
~11.5	-	*	[10]
~8	-	*	[15]
~10	~0	-	Average
~5.5	0.06	pulsed, 1570 nm	This work
~6	0	cw, 1800 nm	This work

Table 3.1. Reported peak absorption cross section values (σ_o) and the relative strength of the excited state absorption (f_p) for Cr^{2+}:ZnSe. Pump wavelengths used in the measurements are also indicated. Those marked by * use the known chromium concentration value of the prepared samples to calculate σ_o.

Chapter 4

PULSED OPERATION OF Cr^{2+}:ZnSe LASERS

Cr^{2+}:ZnSe lasers can be operated in pulsed mode by using a second pulsed pump laser whose wavelength overlaps with the absorption band. The peak powers obtainable from pulsed pump sources are typically high and lasing can thus be achieved at lower average pump powers than those needed for cw pumping. In this Section, we review the work done in the development of pulsed Cr^{2+}:ZnSe lasers. Continuous-wave and mode-locked regimes of operation will later be discussed in Sections 5 and 6, respectively.

4.1 Review of Earlier Work on Pulsed Cr^{2+}:ZnSe Lasers

The first experimental demonstration of lasing action in Cr^{2+}:ZnSe employed pulsed pumping [14, 15]. In this work, Page et al. used a 10-Hz, 10-mJ, Co:MgF_2 laser operating at the wavelength of 1860 nm to excite the Cr^{2+}:ZnSe gain medium. The pump pulsewidth was about 40 μsec. Plane-parallel Cr^{2+}:ZnSe samples were placed at the center of a confocal resonator consisting of two curved mirrors (R=20 cm). The output coupler had a transmission of 7.5%. The pump beam was focused to a spot of several millimeters and up to 600 μJ of output pulse energy was obtained with ~3.5 mJ of absorbed pump energy. The slope efficiency with respect to absorbed pump power was 22.6 %. By using a diffraction grating in Littrow configuration, the laser output could be tuned between 2150 and 2800 nm. The same group also demonstrated the first diode-pumped, pulsed Cr^{2+}:ZnSe laser [28]. In these experiments, an InGaAsP/InP diode laser array producing more than 70 W of peak power at 1.65 μm was used as the pump. The gain medium was excited from one

side. Using a 10 % output coupler, output energies as high as 18 μJ (0.34 W peak power) were obtained with about 150 μJ of absorbed pump energy. To date, pulsed operation of Cr^{2+}:ZnSe lasers has been characterized in numerous other studies [28, 43, 122, 125, 138-141]. In the particular experiments reported by Zakel et al., a 10-mm-long cylindrical Cr^{2+}:ZnSe sample (chromium concentration = $6x10^{18}$ ions/cm^3) was pumped by a 30-W, 7-kHz, Tm:YALO laser at 1940 nm and average output powers as high as 18.5 W (2.64 mJ pulse energy) were obtained during gain-switched operation [141]. The slope efficiency exceeded 65 %. An acousto-optic tunable filter was further used for rapid tuning of the laser output between 2.04 and 2.74 μm.

4.2 Dependence of the Power Performance on Chromium Concentration

In our studies, we investigated the gain-switched operation of a Cr^{2+}:ZnSe laser pumped at 1.57 μm by a pulsed, eye-safe KTP optical parametric oscillator (OPO) [123]. This is a very attractive excitation scheme since the KTP OPO can be pumped by the 1064-nm Nd:YAG lasers which are widely available. One important issue that needs to be addressed in the case of 1570-nm pumping has to do with the poor overlap of the pump wavelength with the Cr^{2+}:ZnSe absorption band (1500 nm to 2100 nm) whose center is at 1775 nm. If the crystal lengths are kept fixed, this requires the use of gain media with higher active ion concentrations to absorb the same amount of pump power. However, as explained in previous sections, high doping concentrations can increase the fluorescence quenching, passive losses at the lasing wavelength, and thermal loading. Hence, it is important to understand the effect of the active ion concentration on the lasing efficiency. In this work, we investigated the dependence of the laser power performance on the active ion concentration in 1570-nm-pumped gain-switched Cr^{2+}:ZnSe lasers.

Figure 4.1 shows the schematic of the KTP OPO pumped Cr^{2+}:ZnSe laser. A Q-switched Nd:YAG laser operating at 1064 nm, producing 145 nsec-long (FWHM) pulses at a pulse repetition rate of 1kHz, was used as the pump source for the OPO. The OPO resonator consisted of a curved dichroic input mirror (M1, R=10 cm) which passed 94 % of the 1064-nm pump and a flat output coupler (M2) with a transmission of 32.5 % at 1570 nm. The OPO output coupler (M2) was also highly reflective at 1064 nm to double-pass the pump through the nonlinear crystal. Optical parametric oscillation occurred inside a 20-mm-long non-critically phase-matched KTP crystal

which was anti-reflection coated at 1064 and 1570 nm on both surfaces. Figure 4.2. shows a photograph of the KTP OPO cavity.

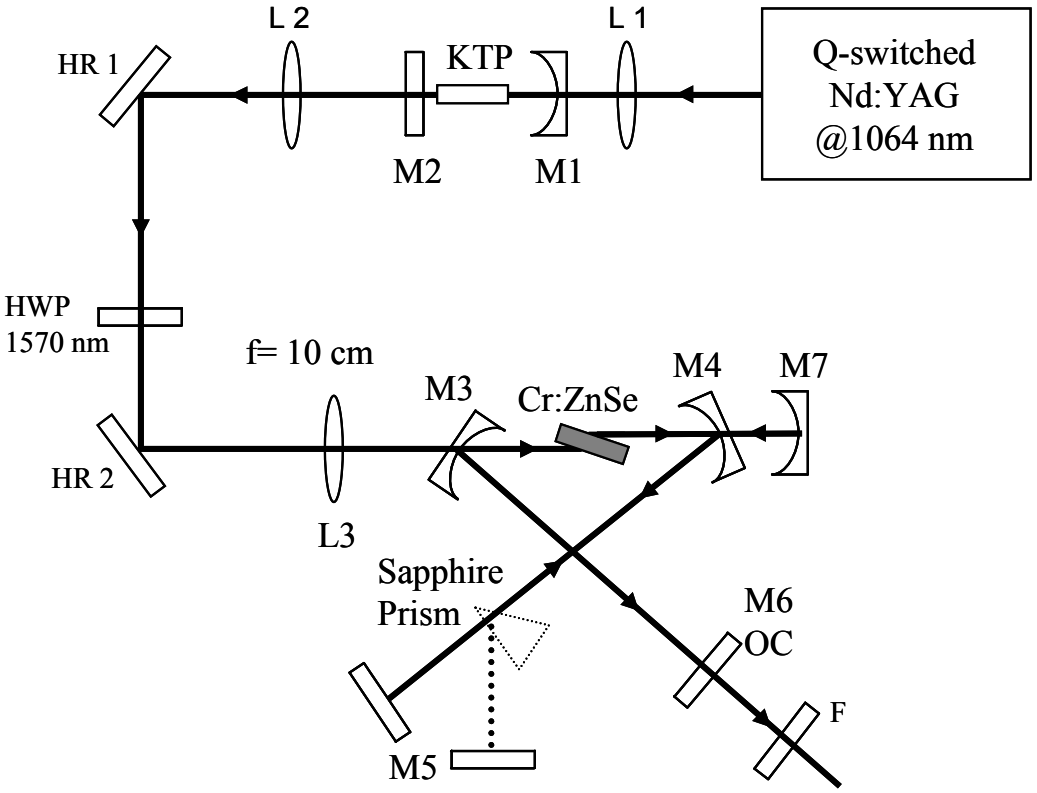

Figure 4.1. Schematic of the gain-switched OPO intracavity Cr^{2+}:ZnSe laser. The main pump source was a Q-switched 1 kHz Nd:YAG laser operating at 1064 nm. A 20 mm long KTP crystal was used to produce 1570 nm light. OPO cavity was constructed between M1 and M7. OPO intracavity Cr^{2+}:ZnSe resonator consist of the mirrors M3-M6 (See the text for a detailed description of the various components).

A converging lens (L2, f = 10 cm) was used to collimate the OPO output, which was then sent into the Cr^{2+}:ZnSe sample with two turning mirrors (HR1-HR2). The pump was focused to a beam waist of about 100 μm with a second converging lens (L3, f = 10 cm). The Cr^{2+}:ZnSe laser was a standard x-cavity, consisting of two curved high reflectors each with a radius of curvature of 10 cm (M3 and M4), a flat end high reflector (M5), and a flat output coupler (M6). The length of each resonator arm was around 15 cm. 2 to 3 mm-thick Cr^{2+}:ZnSe samples prepared using thermal

diffusion doping [104] was used in the lasing experiments. The samples were not antireflection coated, and placed at Brewster's angle between M3 and M4. Figure 4.3 shows a photograph of the KTP OPO-pumped Cr^{2+}:ZnSe laser cavity.

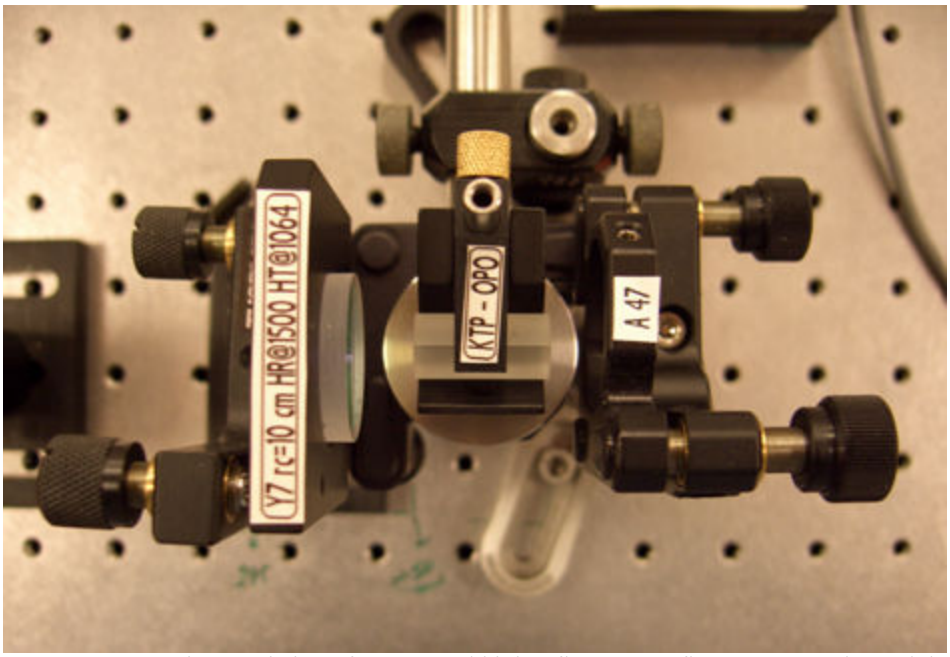

Figure 4.2. KTP OPO cavity consisting of one curved high reflector, one flat output coupler and the 20-mm long KTP material.

To demonstrate tuning in different parts of the spectrum, four different mirror sets with central reflectivity wavelengths at 2, 2.25, 2.6 and 2.9 μm were used. All the high reflectors had transmission greater than 90 % at 1570 nm. In the experiments, tuning was achieved by using a Brewster-cut sapphire prism. A filter (F) was used after the output coupler to block the residual pump beam. The cavity was not purged during the measurements, and the relative humidity was around 40 %. A curved gold retro reflector (M7, R=10 cm) was further placed after the curved high reflector (M4) in some of the experiments. In addition to enabling double-pass pumping of the gain medium [27, 116], this configuration also provides feedback for the OPO setup, extending the effective resonator for 1570-nm oscillation from M1 to M7. This intracavity configuration will be further discussed in Section 4.4.

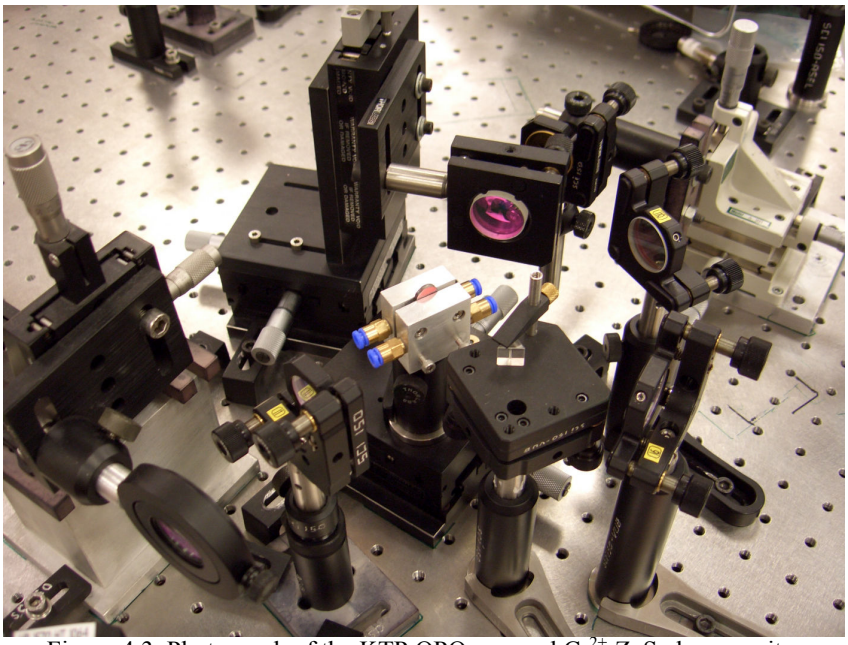

Figure 4.3. Photograph of the KTP OPO pumped Cr^{2+}:ZnSe laser cavity.

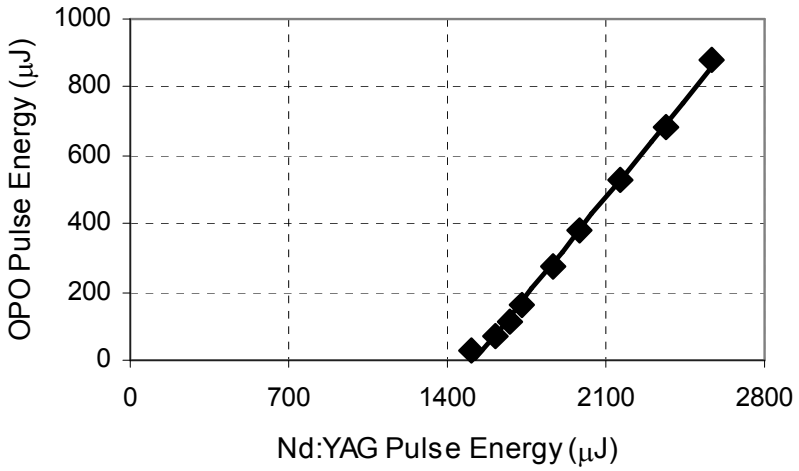

Figure 4.4. Efficiency curve of the KTP OPO, pumped by a Q-switched Nd:YAG laser operating at 1570 nm. In double pumping configuration slope efficiencies as high as 82% was obtained.

Figure 4.4 shows the efficiency curve for the KTP OPO pump system, in the double-pumped configuration (since M2 was HR @ 1064 nm). With 2.57 mJ of 1064-nm pump, as high as 880 μJ of output was obtained at 1570 nm with a slope efficiency of 82 %. The high slope efficiency resulted from the double passing of the pump. The estimated pump spot size and the threshold pump energy were 190 μm and 1.4 mJ, respectively. The KTP OPO produced 65-ns (FWHM) pulses at a pulse repetition rate of 1 kHz. A typical KTP OPO pulse is shown in Fig. 4.5. This OPO system was also used to measure the fluorescence lifetime of the Cr^{2+}:ZnSe samples as explained in Section 3.2.

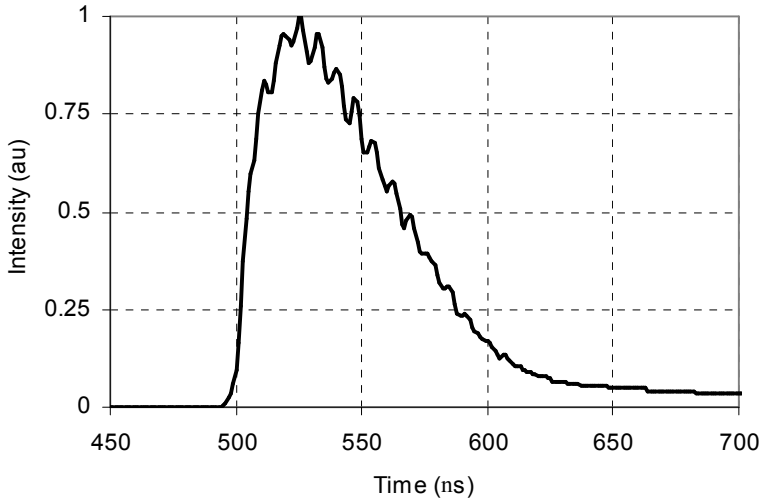

Figure 4.5. Oscilloscope trace of a typical KTP OPO pulse.

Sample	Sample Length (mm)	$\alpha_{1.775\ \mu m}$ (cm^{-1})	Absorption at 1570 nm (%)	Average Cr^{2+} Concentration (x 10^{18} cm^{-3})	Lifetime (μs)
1	3.03	4.1	51	3.6	5.0
2	3.04	16	75	14	4.4
3	3.06	29	99	25	1.5
4	1.94	6.5	43	5.7	5.0
5	1.85	12.2	60	11	4.3

Table 4.1. Properties of the Cr^{2+}:ZnSe samples used in the KTP OPO pumped, gain switched lasing experiments.

We used three Cr^{2+}:ZnSe samples with thickness of ~3 mm and Cr^{2+} concentrations of $3.6x10^{18}$, $14x10^{18}$, and $25x10^{18}$ ions/cm^3 to investigate the concentration dependence of the power performance. Table 4.1 lists the optical properties of the three samples (Samples 1-3). Figure 4.6 shows a photograph of the Cr^{2+}:ZnSe sample 2, held securely between aluminum plates.

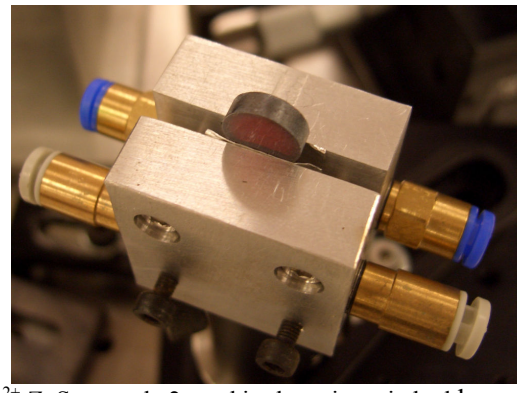

Figure 4.6. Cr^{2+}:ZnSe sample 2 used in the gain switched laser experiments .

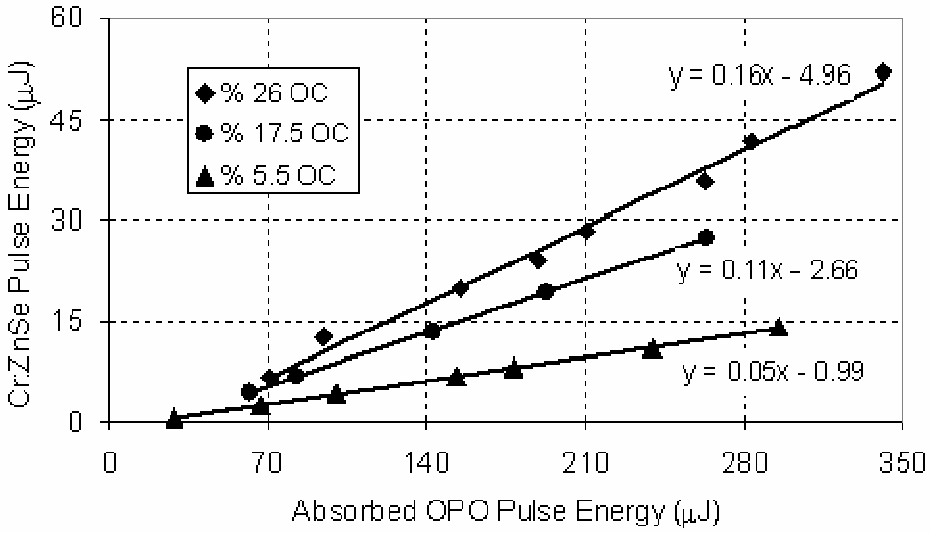

Figure. 4.7. Measured variation of the output energy as a function of the absorbed pump energy for the Cr^{2+}:ZnSe sample 2 with a doping concentration of $14x10^{18}$ cm^{-3}. Output couplers with 5.5, 17.5, and 26 % transmission were used.

Three different output couplers with 5.5, 17.5, and 25 % transmission were used to characterize the laser performance with each sample. Figure 4.7 shows the variation of the output pulse energy as a function of the absorbed pump energy for different output coupler transmissions using sample 2. The highest output energy was obtained using the 25 % output coupler.

The role of active ion concentration on the lasing performance was also studied. Figure 4.8 shows the energy efficiency curves taken with the 25 % output coupler. The highest output energy was obtained with Sample 2, which had a peak absorption coefficient of 16 cm^{-1} at 1775 nm and a corresponding Cr^{2+} concentration of $14x10^{18}$ ions/cm^3. In this case, the resonator produced 52 μJ of output energy with 340 μJ of absorbed pump energy. Note that the power performance degrades monotonically with increasing ion concentration. In particular, the slope efficiency of the resonator decreases from 25 % to 12 % when the ion concentration increases from $3.6x10^{18}$ to $25x10^{18}$ ions/cm^3. This could be mainly attributed to an increase in passive losses at the lasing wavelength, as described in Section 2.5. Although the slope efficiency was higher with Sample 1, higher output energy was obtained with Sample 2 due the larger absorption of the latter.

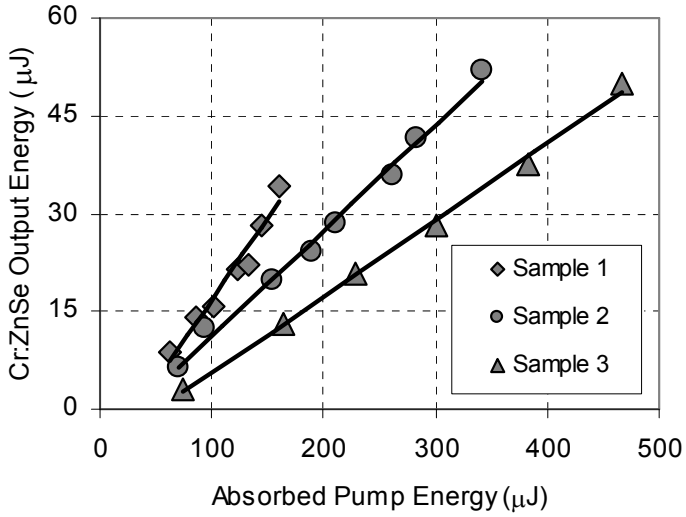

Figure 4.8. Measured variation of the output energy as a function of the absorbed pump energy for the three different Cr^{2+}: ZnSe samples used in the experiment. Properties of the samples are listed in Table 4.1. 2.9-μm mirror set and a 25 % output coupler was used in the measurements.

The passive loss analysis of the samples was also performed by using the power efficiency data obtained with three output couplers [142]. The slope efficiency η of the laser can be expressed in terms of the output coupler transmission T and the round trip passive loss L as

$$\eta = \eta_0 \frac{T}{T + L}, \tag{4.1}$$

where η_0 is the maximum slope efficiency that can be obtained at high output coupling. Factors including the finite quantum defect of the laser transition, mode matching between the pump and the laser beams, and luminescence quantum efficiency all affect η_0. Figure 4.9 shows the variation of the inverse slope efficiency (1/η) as a function of the inverse transmission (1/T) of the output couplers for the three samples. As can be seen from Eq. 4.1 the intercept and the slope of the linear best fit can be used to determine the values of η_0 and L. Using this method, the single-pass loss was estimated to be 11, 15 and 31 % for samples 1, 2 and 3, respectively. Here, atmospheric and mirror losses were neglected. The estimated passive losses of the samples scale with chromium concentration, as expected from the spectroscopic results (See section 2.5).

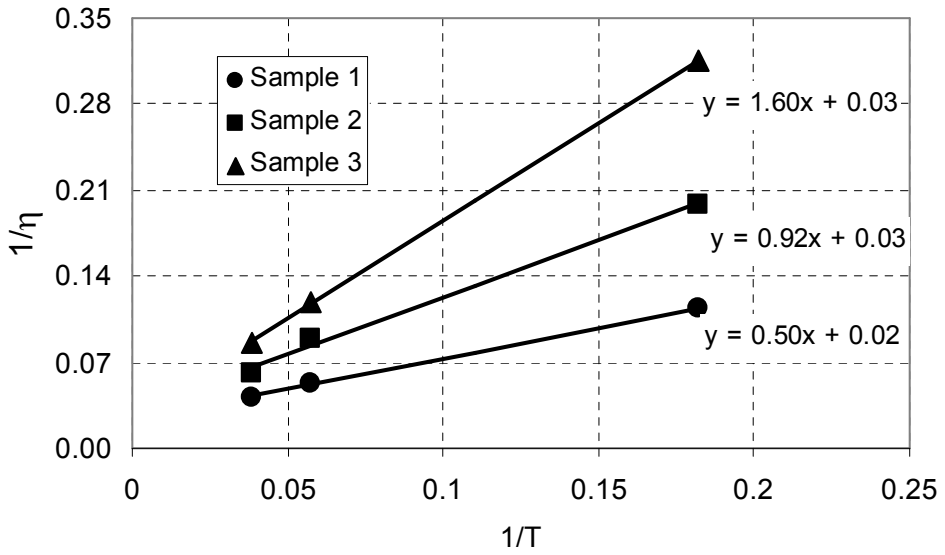

Figure 4.9. Measured variation of the inverse slope efficiency (1/η) as a function of the inverse output coupler transmission (1/T) for the three different Cr^{2+}: ZnSe samples used in the experiment.

4.3 Intracavity-Pumped Cr^{2+}:ZnSe Laser with Ultrabroad Tuning

To date, different tuning schemes have been used to obtain broad tuning with Cr^{2+}:ZnSe lasers. With gratings [15], birefringent filters [143], or prisms [27], [116] as wavelength-selective elements, broad tuning of Cr^{2+}:ZnSe gain medium between 2000-3100 nm has been achieved [30]. Note that tuning with gratings was obtained only in the pulsed regime, whereas tuning with the other wavelength-selective elements was demonstrated in continuous-wave regime. So far, tuning below 2000 nm has not been possible due to the overlap of the absorption and emission bands (absorption peak=1775 nm, with a width (FWHM) of 365 nm extending from 1500 nm to 2100 nm) [104].

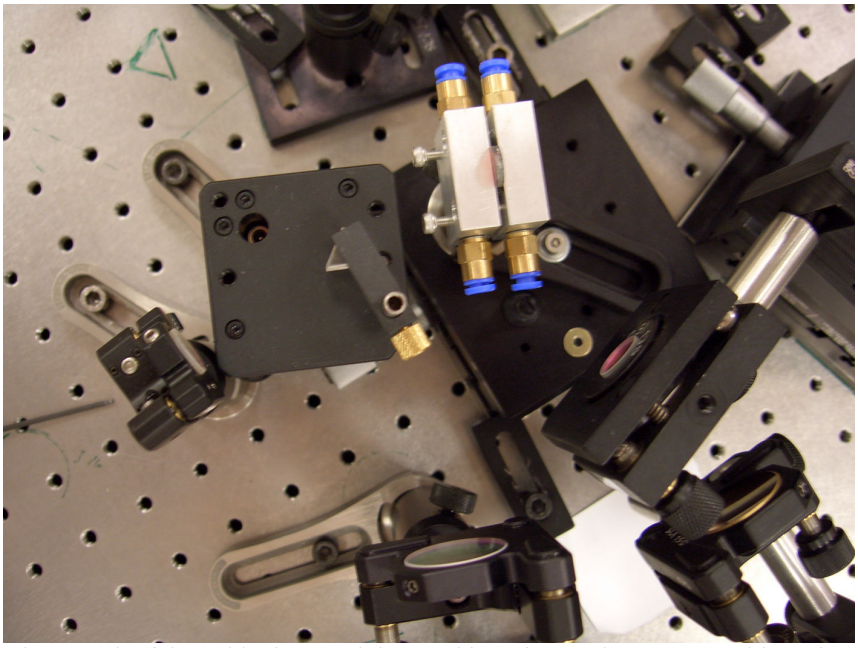

Figure 4.10 Photograph of the gold mirror and the sapphire prism to demonstrate wide tuning of the gain-switched Cr^{2+}:ZnSe laser.

In this section, we describe continuous tuning of a gain-switched Cr^{2+}:ZnSe laser in the 1880 to 3100 nm wavelength range. To extend the tuning range below 2000 nm, samples with lower Cr^{2+} concentration were used to decrease the self-absorption losses at this wavelength region. To compensate for the reduced absorption of the crystal, an intracavity pumping scheme was further used with a KTP optical parametric oscillator (OPO) operating at 1570 nm. A curved gold retro

reflector (M7, R=10 cm) was further placed after the curved high reflector (M4) (See Fig. 4.10). In addition to enabling double-pass pumping of the gain medium [27, 116], this configuration also provides feedback for the OPO setup, extending the effective resonator for 1570-nm oscillation from M7 up to the input high reflector of the optical parametric oscillator (M1). Choosing a pump wavelength close to the lower end of the absorption band was also crucial in obtaining laser operation below 2 μm. Furthermore, intracavity pumping resulted in about threefold increase in the maximum attainable laser power in comparison with single-pass pumping. To the best of our knowledge, this is the first demonstration of lasing below 2000 nm with Cr^{2+}:ZnSe lasers, making the fractional tuning range ($\Delta\lambda/\lambda_0 \cong (3100\text{-}1880)/2490=0.49$) comparable to that of Ti^{+3}:Al_2O_3 ($\Delta\lambda/\lambda_0 \cong 0.57$) lasers.

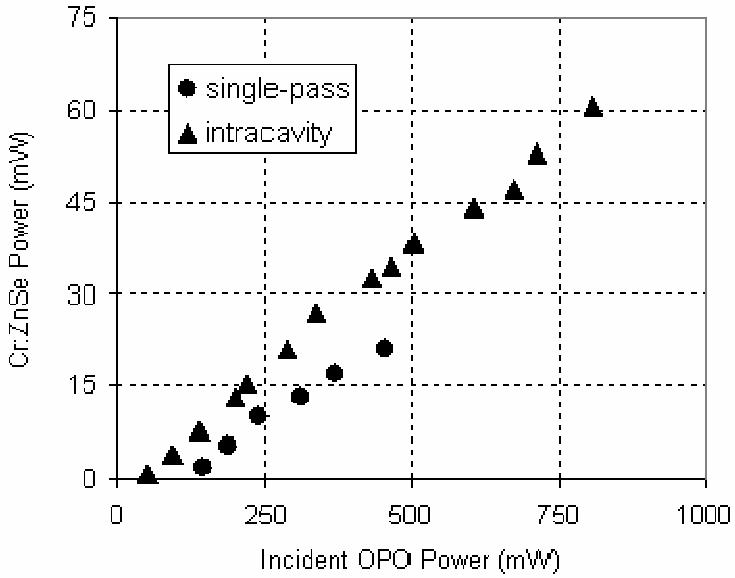

Figure 4.11. Efficiency curves for the Cr^{2+}:ZnSe laser at 2100 nm for single pass and intracavity pumping. With 1.8 W of Nd:YAG power, 21 and 61 mW of Cr^{2+}:ZnSe laser output powers were obtained for single-pass pumping and intracavity configurations, respectively.

To demonstrate tuning below 2 μm, the HR set which had a high reflectivity between 1790 and 2150 nm (reflectivity > 99 %) was used, along with a 6 % output coupler (1900 nm). Figure 4.11 shows the power performance of the gain-switched Cr^{2+}:ZnSe laser at 2100 nm taken with sample 4

(see Table 4.1, Cr^{2+} concentration = $5.7x10^{18}$ ions/cm^3, fluorescence lifetime = 5 μs, small signal absorption at 1570 nm = 43 %). In single-pass pumping configuration, with 1.8 W of Nd:YAG power, 460 mW of OPO power was available to pump the Cr^{2+}:ZnSe laser. At this pumping level, only 21 mW of Cr^{2+}:ZnSe output power could be obtained. In intracavity pumping configuration, the available OPO pump power with 1.8 W of Nd:YAG power increased from 460 mW to 810 mW. Besides, double pumping of the pump beam increased the slope efficiency (with respect to incident pump power) of the Cr^{2+}:ZnSe laser from 6 % to 8 %, and decreased the laser threshold from about 75 mW to 50 mW. Overall as high as 61 mW of Cr^{2+}:ZnSe output power was obtained using the intracavity pumping configuration. The best power performance was obtained with the 2.6 μm HR set using a 25 % OC. Figure 4.12 shows power performance of the gain-switched Cr^{2+}:ZnSe laser taken with the 2.6 μm HR set using sample 4. Here, as high as 145 mW of laser output power was obtained at 2365 nm, with about 1.2 W of intracavity OPO power (Nd:YAG pump power = 1.8 W). In this case, the slope efficiency with respect to the incident pump power was 12.5 %. At this pumping level, only 36 mW of output power could be obtained using single-pass pumping. Similar results were obtained with other high reflectors, except for the 2.25 μm HR set, where intracavity pumping could not be achieved due to the low damage threshold of the high reflector coatings.

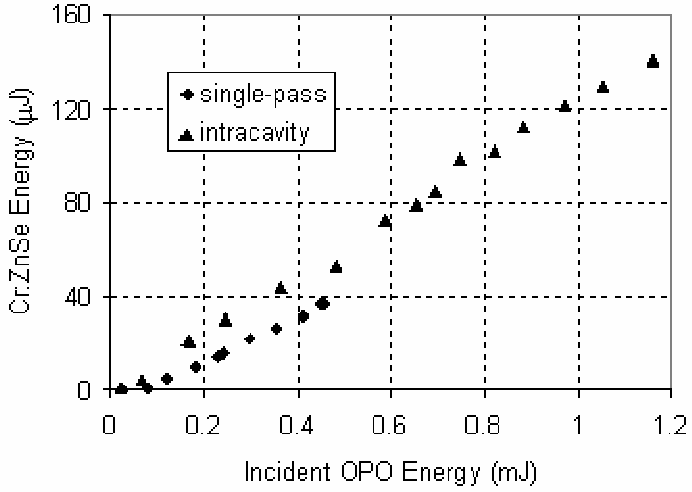

Figure 4.12. Energy efficiency curves taken with Sample 4 in the single-pass and intracavity pumping configurations. 2.6-μm mirror set (output coupler transmission=25%) was used.

Figure 4.13 shows the tuning data of the intracavity pumped Cr:ZnSe laser taken with the 2 μm HR set. Continuous tuning could be obtained between 1880 and 2130 nm. The solid line in Fig. 4.13 shows the estimated round-trip cavity loss due to reabsorption in the gain medium. Note that due to the low saturation intensity of the Cr^{2+}:ZnSe gain medium, the actual reabsorption losses were lower during laser operation. The tuning curve was optics-limited above 2130 nm, and lasing could not be obtained below 1880 nm due excessive reabsorption losses.

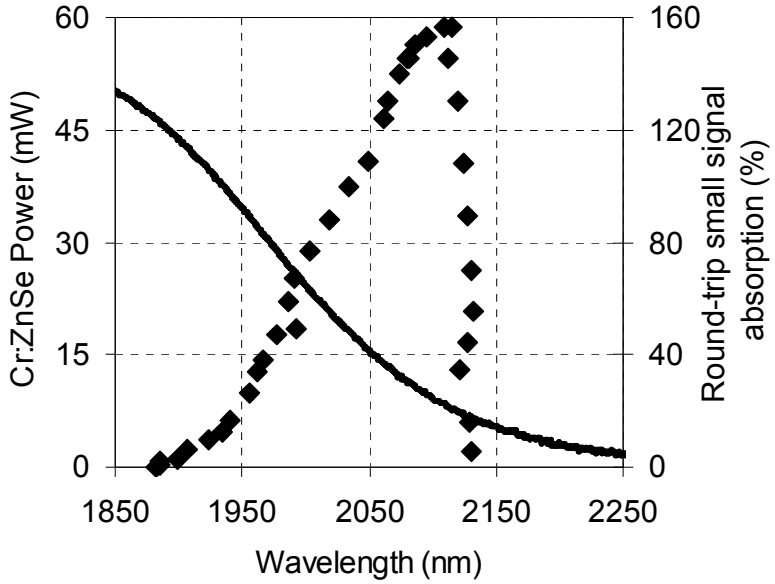

Figure 4.13. Tuning curve of the intracavity pumped Cr^{2+}:ZnSe laser between 1880 and 2130 nm. Solid line shows the estimated round-trip small-signal cavity loss caused by reabsorption in the gain medium.

Tuning experiments were conducted by using 4 sets of resonator optics with center wavelengths of 2 (OC transmission =7%), 2.25 (OC transmission =25%), 2.6 (OC transmission =25 %), and 2.9 μm (OC transmission =4 %). The bracketed values indicate the output coupler transmission for each set of mirrors at the center of the reflectivity window. Measured variation of the output energy as a function of the wavelength is shown in Fig. 4.14 for an input Nd:YAG pump energy of about 1.8 mJ. Here the input intracavity OPO pump energy did not remain constant due to the fact that different sets of the optics used in the tuning experiments had different overall transmission at 1570 nm. Due to the low damage threshold of the 2.25 μm HR mirrors, intracavity configuration was not

applied with this set; hence lower output powers were obtained. The solid curve in Fig 4.14 shows the estimated single pass small signal reabsorption loss of the Cr^{2+}:ZnSe gain medium (Sample 4). With intracavity pumping, the demonstrated fractional tuning range was 0.49 ($\Delta\lambda/\lambda_0 \cong (3100-1880)/2490=0.49$) comparable to that of $Ti^{+3}:Al_2O_3$ ($\Delta\lambda/\lambda_0 \cong 0.57$) lasers (see Table 1.1). Also note from Fig. 4.14 that use of Sample 5 with a 25 % transmitting output coupler improves the laser efficiency in the long wavelength end of the tuning range.

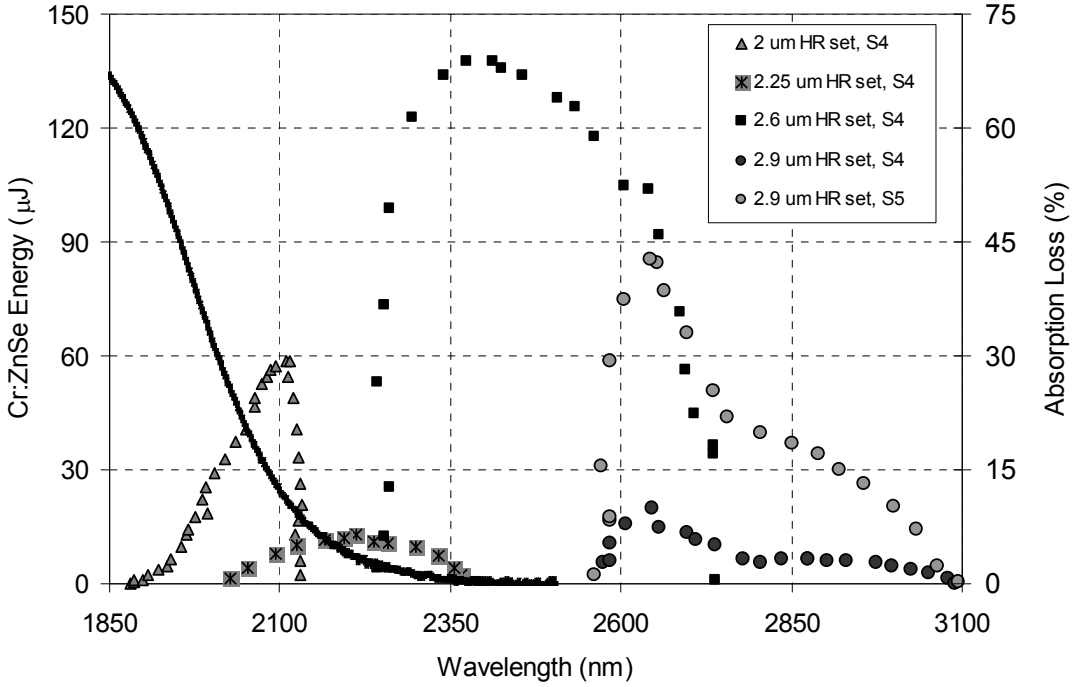

Figure 4.14. Tuning curve for the intracavity-pumped gain-switched Cr^{2+}: ZnSe laser taken with four different mirror sets. Laser emission could be obtained in the 1880 to 3100 nm wavelength range. The solid line is the small-signal, single pass loss of Sample 4 due to self absorption.

4.4 Pulse Forming Dynamics of Cr^{2+}:ZnSe Laser

In this part we will review the work on pulse formation dynamics in gain-switched Cr^{2+}:ZnSe laser. In gain switched operation, Cr^{2+}:ZnSe gain medium was excited using a high peak power pulsed laser. The pumping rate is fast enough to accumulate a population inversion at the upper laser level

that is much more than the laser threshold, before laser oscillation builds up in the resonator. Depending on the width and the intensity of the pump pulse, the gain medium relaxes either by producing one or several output laser pulses. Roughly speaking, if the pump pulse is much shorter than the relaxation oscillation period, then the gain medium will produce only one single pulse (with one spike) [144]. The relaxation oscillation period (T_R) of a laser is roughly equal to

$$T_R \approx 2\pi\sqrt{\tau_{rad}\tau_{cav}} \tag{4.2}$$

where τ_{rad} is the radiative lifetime (~5.6 μs for Cr^{2+}:ZnSe) and τ_{cav} is the cavity photon lifetime [15]. For a resonator length of 40 cm, an output coupler transmission of 20 %, and a 2 mm thick sample with a single pass passive loss of 0.1 cm^{-1}, cavity photon lifetime is about 10 ns, making the relaxation oscillation period approximately equal to 1.5 μs. For example, Page et al. used ~5 μs long pulses of a Co:MgF_2 to excite Cr^{2+}:ZnSe medium [15]. Since the pump pulse length was longer than the expected relaxation oscillation period, the obtained output pulses consisted of several spikes. Similarly, Alford et al. used ~450 ns long output of a 1.94 μm Tm:$YAlO_3$ laser as the excitation source [140]. In this case the pump pulse duration was also comparable with the expected relaxation oscillation period. Similarly the gain switched laser output pulse consisted of two spikes. In the case where a pulse consists of several spikes, the time period between the pulses is roughly equal to the relaxation oscillation period [15, 140].

In our case, we used a 65-ns long OPO pulse at 1570 nm for excitation, which is much shorter than the relaxation oscillation period (1.5 μs), thus the laser cavity produced a single pulse without any spike. As an example, Fig. 4.15 shows the temporal profile of the pump and laser pulses, obtained with the Cr^{2+}:ZnSe sample 1. The output coupler transmission and the incident pump energy were 25 % and 90 μJ, respectively. In Fig. 4.15 the first pulse is the 65-ns long incoming OPO pulse at 1570 nm. At this pump pulse, the resonator produced 28-ns-long pulses with 4 μJ of energy and the pulse build-up time (the delay between the 1570-nm pump pulse and the laser pulse) was around 210 ns. We investigated the variation of the pulse build-up time and the output pulsewidth as a function of absorbed pump energy, chromium concentration, and output coupler transmission. Three Cr^{2+}:ZnSe samples (Samples 1-3, in Table 4.1) were used in the experiments. As an example, Figure 4.16 shows temporal profile of the pump and laser pulses obtained with

sample at two different pumping levels. Note that as the pump power is increased both the pulse delay and the pulse buildup time decreases.

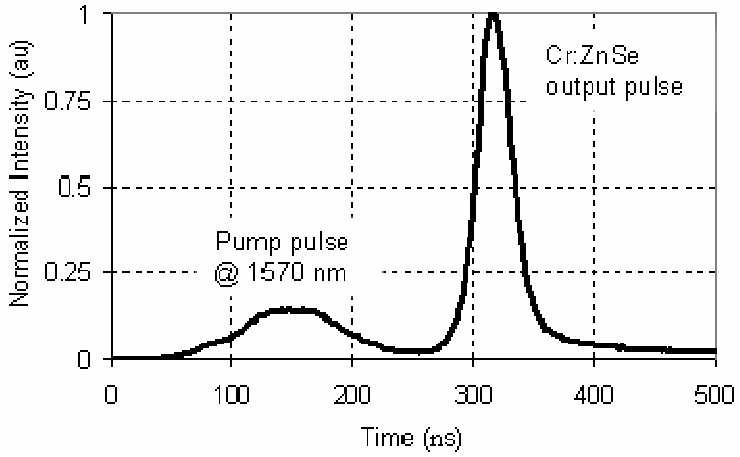

Figure 4.15. Temporal profiles of the OPO pump pulse (pulsewidth=65 ns) and the output laser pulse (pulsewidth= 28 ns). The pulse build-up time is 210 ns. Intensities of the pump and the laser pulse are not to scale.

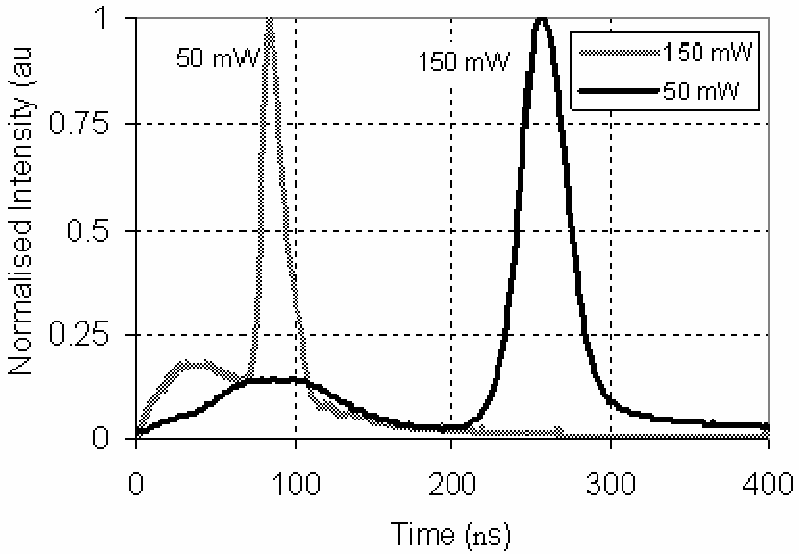

Figure 4.16. Temporal profiles of the OPO pump pulse and the output laser pulse at two different pumping levels taken with sample 1 using the 25% OC. Intensities of the pump and the laser pulses are not to scale.

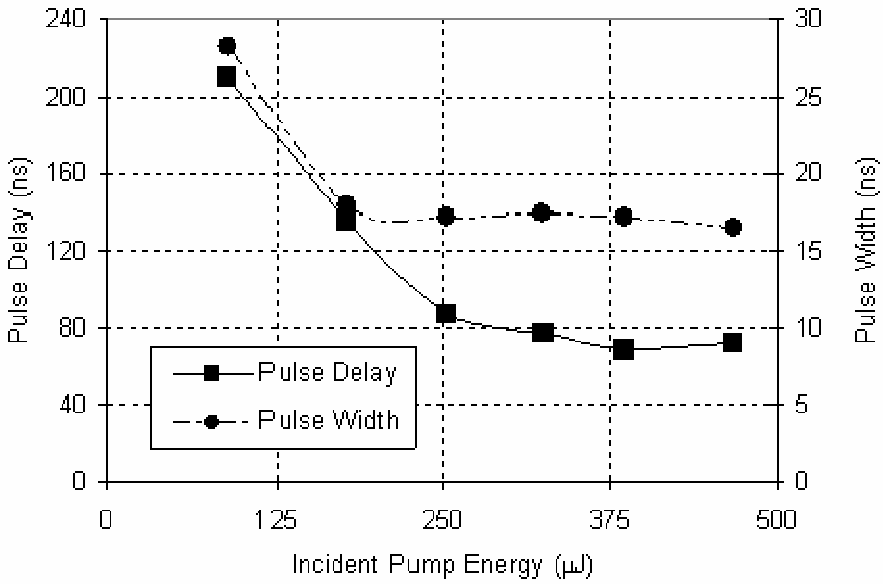

Figure 4.17. Measured variation of the delay and the output pulse width as a function of incident pump energy for the gain-switched Cr^{2+}: ZnSe laser. Sample 1 and the 2.9-μm mirror set (output coupler transmission=25%) were used.

Figure 4.17 shows the measured variation of the pulse build-up time and the output pulsewidth as a function of the incident pulse energy. As expected, both the build-up time and the output pulsewidth decrease with increasing pump energy (increasing gain) until the pump pulse saturates. Furthermore, for a fixed output coupler transmission and pumping level, both pulse build-up time and the output pulsewidth were found to decrease with increasing concentration due to an increase in the overall absorption and hence the gain of the samples. The shortest pulse width and pulse build-up time were obtained with the highly doped Cr^{2+}:ZnSe sample 3. In this case, with 470 μJ of incident pump energy (~400 μJ absorbed) and output coupler transmission, pulses as short as 11 ns in duration were obtained with a corresponding build-up time of 60 ns. Finally, the effect of output coupler transmission on pulse formation dynamics was also investigated. The pulsewidth was fairly insensitive to output coupler transmission; however, the pulse delay increased due to larger resonator losses. In particular, the pulse delay increased from 82 ns to 94 ns when the output

coupler transmission went from 1 to 26% at incident pump energy of 210 μJ (sample 1). In the same transmission range, output pulsewidth increased from 17 ns to 20 ns.

Chapter 5

CONTINUOUS-WAVE Cr^{2+}:ZnSe LASERS

As noted in the Introduction, several favorable characteristics of the Cr^{2+}:ZnSe medium enable efficient continuous-wave laser operation at room temperature. These include the 4-level energy structure, absence of excited-state absorption, and high luminescence quantum efficiency near room temperature. On the other hand, the high thermal index coefficient ($dn/dT=70x10^{-6}$ /°K for Cr^{2+}:ZnSe [145]) and temperature dependence of the fluorescence lifetime above room temperature cause unwanted thermal loading problems and could limit power scaling in room-temperature systems. In this section, we review the work done on the development of cw Cr^{2+}:ZnSe lasers. We discuss the operation under various pumping configurations and the results obtained with regard to power efficiency and tuning performance. We also discuss the recent work done in our group on the characterization of a cw Cr^{2+}:ZnSe laser pumped by a Tm-fiber laser at 1800 nm. Experimental data showing power efficiency, tuning, and the role of active ion concentration are presented.

5.1 Review of Earlier Work on CW Cr^{2+}:ZnSe Lasers

Room-temperature continuous-wave operation of a Cr^{2+}:ZnSe laser was first reported by Wagner et al. [27]. A 1-W Tm:YALO laser operating at 1940 nm was used as the pump source. A three-mirror cavity was end-pumped with the Tm:YALO laser and different Cr^{2+}:ZnSe samples with thicknesses in the 1-3-mm range were used. The pump was focused to a 60-μm waist. Best results were obtained with a 2.76-mm-long crystal that had a single-pass absorption of 35%. The curved gold high reflector of the laser cavity was used for double passing the pump beam, resulting in a total effective pump absorption of 58%. With a 7% transmitting output coupler, 250 mW of output was

obtained by using 600 mW of absorbed pump power, giving a slope efficiency (with respect to the absorbed pump power) of 63%. By using a Brewster-cut ZnSe prism placed near the output coupler, the output wavelength of the laser could also be continuously tuned between 2138 and 2760 nm.

Following the first demonstration of cw lasing in Cr^{2+}:ZnSe lasers, several alternative pump sources were employed to obtain tunable cw output. These include Co^{2+}:MgF_2 [116, 146], Tm:YALO [27], Tm:YLF [145], NaCl:OH^- [147], Er-doped fiber lasers [33, 36, 127, 148-150], and others. In the particular experiments described by Sorokin and Sorokina, tunable diode-pumped cw operation was demonstrated by using InGaAsP-InP laser diodes operating at 1600 nm [143]. A three-mirror resonator was used and the gain crystal was end-pumped from two sides. The total available diode power was 1W. With 1 % output coupler, lasing could be obtained with as low as 30 mW of absorbed pump power. Different output couplers with transmissions in the range 1-7% were used to investigate the dependence of the output power on pump power. By using the 7% output coupler and 460 mW of absorbed pump power, 70 mW of output could be obtained. The output wavelength of the laser could be varied by using an intracavity Lyot filter. In this case, the polarized output of the laser could be tuned over 350 nm from 2300 to 2650 nm.

5.2 1.8-μm Tm-Fiber Pumped CW Cr^{2+}:ZnSe Laser

In our experiments, we employed a thulium-doped fiber laser operating at 1800 nm to investigate the cw lasing characteristics of a Cr^{2+}:ZnSe laser. Pumping at 1800 nm has several advantages. First and foremost, because the pump wavelength is very close to the absorption resonance, a desired level of absorption can be obtained by incorporating the minimum possible amount of active ions into the ZnSe host. It is known that the amount of passive losses at the lasing wavelength as well as the rate of non-radiative decay increase with ion concentration. Pumping at 1800 nm and using crystals with low active ion concentration reduces passive laser losses, decreases the rate of non-radiative decay and also minimizes thermal loading effects that would arise due to the temperature dependence of the fluorescence lifetime. All these positive factors are expected to improve the power scaling capability of room-temperature Cr^{2+}:ZnSe lasers especially at higher pumping levels.

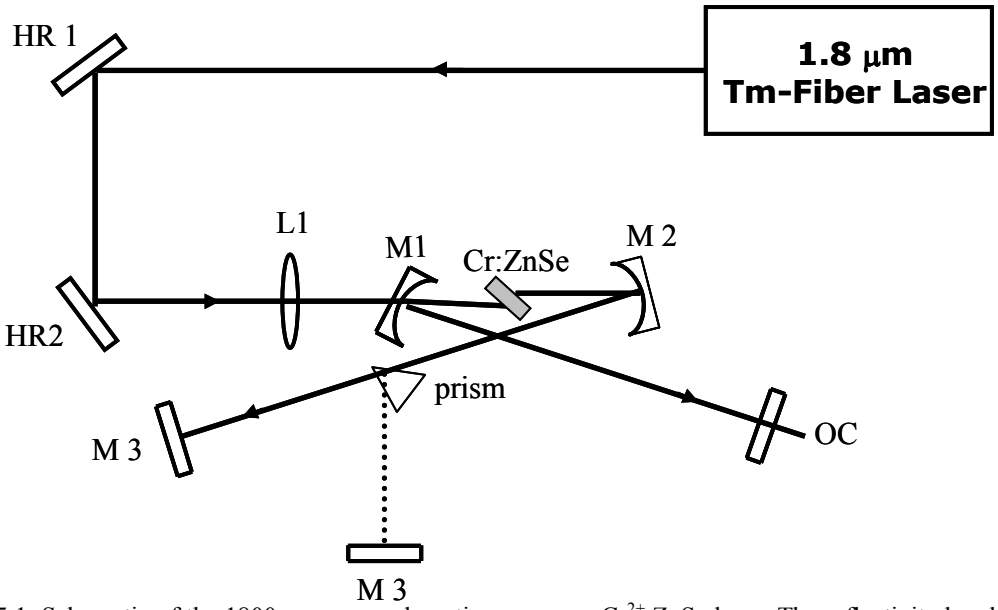

Figure 5.1. Schematic of the 1800-nm-pumped continuous wave Cr^{2+}:ZnSe laser. The reflectivity band of the high reflectors was centered around 2.6-μm. See the text for a detailed description of the components.

Figure 5.1 shows the experimental arrangement of the cw Tm-fiber-pumped Cr^{2+}:ZnSe laser (A photograph of the cavity is shown in Fig 5.3). The pump source was a 5-W, commercial Tm-fiber laser at 1800 nm. The collimated beam diameter ($1/e^2$) and the M^2 were 4.5 mm and 1.03, respectively. In the first set of experiments, we used a single Cr^{2+}:ZnSe sample with a length 2.6 mm and a pump absorption coefficient of 10.7 cm^{-1} at 1800 nm (See Fig. 5.2). The measured fluorescence lifetime was 4.6 μsec. The round-trip loss was 4.1 % at the lasing wavelength, giving a crystal figure of merit (FOM=$\alpha_{1800}/\alpha_{2500}$, α_{1800}=differential absorption coefficient at 1800 nm and α_{2500}=differential loss coefficient at 2500 nm) of 70. The sample was held in a copper holder maintained at 15 °C.

The cavity was a standard, astigmatically compensated, 4-mirror x-cavity in which the gain crystal was placed between two curved high reflectors each with R=10 cm (M1 and M2). The cavity was terminated with a flat high reflector (M3) on one end and a flat output coupler (OC) on the other. In the experiments, 3 different output couplers with transmissions of 3, 5.8, and 15.3 % at 2500 nm were used. The incident pump beam was focused to a waist of 36 μm inside the gain

medium with an input lens (f=10 cm). ABCD analysis of the cavity shows that the cavity beam waist at the center of the stability region was 45 μm at the wavelength of 2400 nm (total cavity length=90 cm).

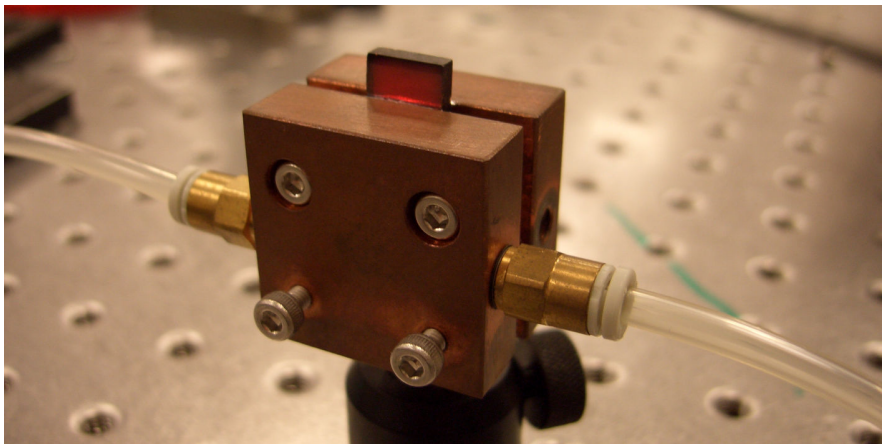

Figure 5.2. Cr^{2+}:ZnSe sample with a length 2.6 mm and a pump absorption coefficient of 10.7 cm^{-1} at 1800 nm is used in cw lasing experiments

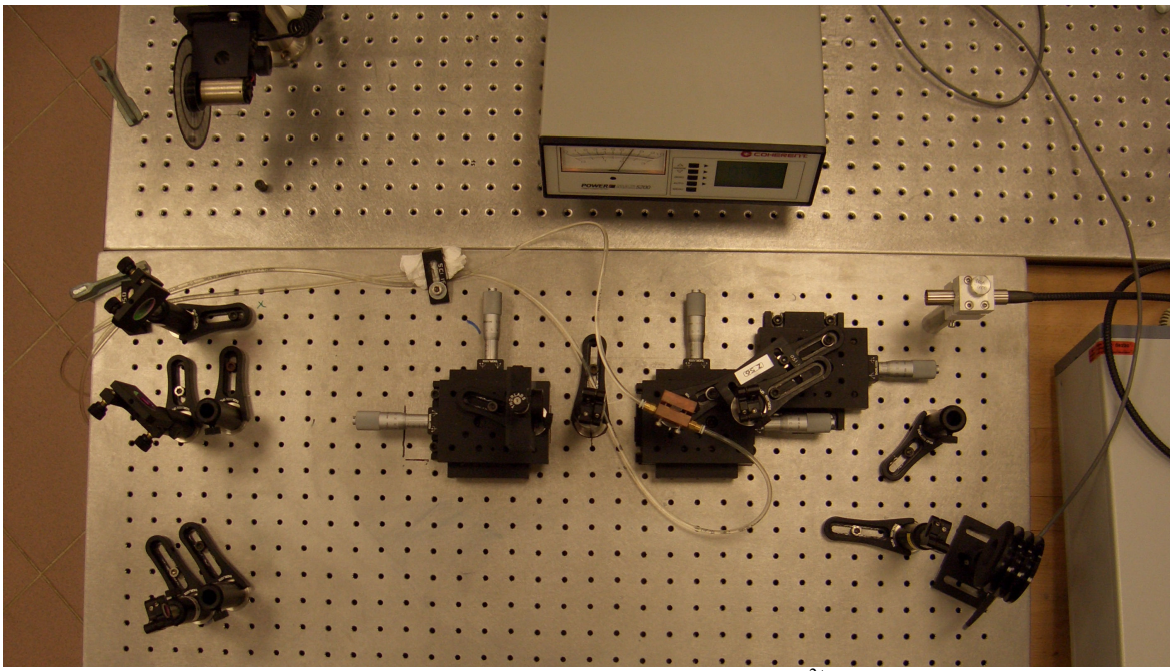

Figure 5.3. Photograph of the 1.8-μm Tm-fiber pumped Cr^{2+}:ZnSe laser.

Figure 5.4 shows the measured cw lasing performance of the Cr^{2+}:ZnSe sample for the 3 different output couplers. As an example, with the 3% transmitting output coupler, 300 mW of output power was obtained with 2.3 W of pump power. The corresponding threshold pump power and the incident power slope efficiency were 207 mW and 16 %, respectively. The free running laser output wavelength shifted slightly for the different output couplers used. While the lasing peak was at 2512 nm with the 3 % OC, it shifted to 2480 nm with the 15.3 % OC. The width of the laser line (FWHM) was about 0.5 nm.

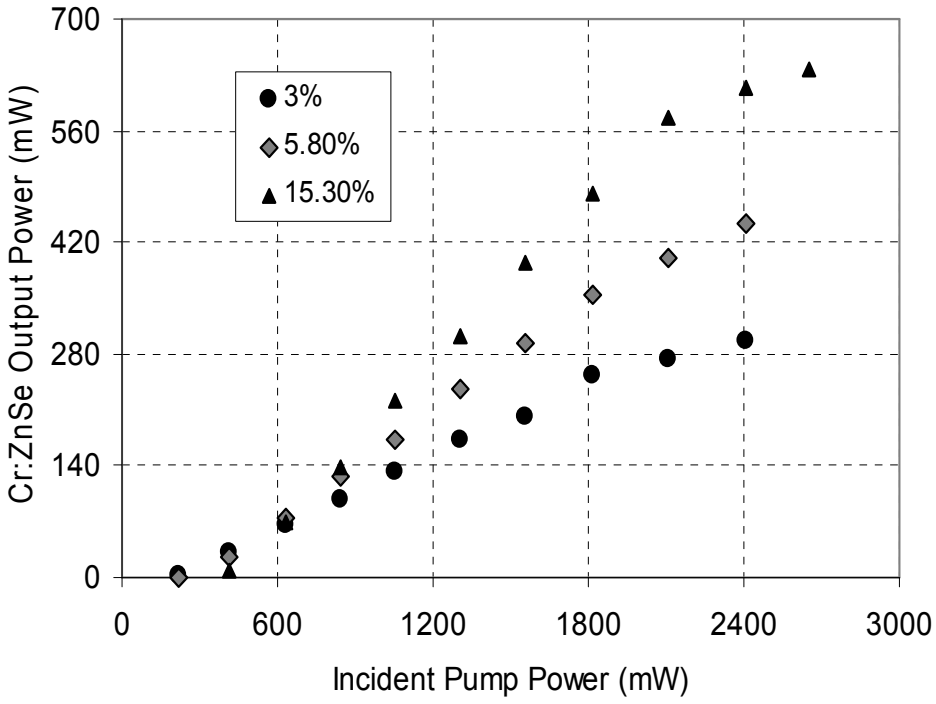

Figure 5.4. Continuous-wave power efficiency data for the cw Cr^{2+}:ZnSe laser taken with 3, 5.8, and 15.3 % transmitting output couplers.

The best power performance was obtained with the 15.3 % transmitting output coupler. Here, as high as 640 mW of output power was obtained with 2.5 W of pump. The slope efficiency with respect to incident pump power was 34 %. Due to thermal loading saturation of the output power was observed at pump powers beyond 2.5 W [145]. The slope efficiencies were calculated from a

linear fit to the laser efficiency data at low pump powers where the output power saturation is not yet effective. Threshold pump powers were estimated by using these linear fits. Table 5.1 lists the threshold pump power and the slope efficiency obtained with each output coupler.

OC Transmission (%)	Slope Efficiency (%)	Threshold Pump Power (mW)
3	16	208
5.8	23	277
15.3	34	413

Table 5.1. Threshold pump power and the slope efficiency values for each output coupler (OC).

Resonator losses at the lasing wavelength were estimated by using the Findlay-Clay and Caird [142] analysis. In the Findlay-Clay analysis, one can use the laser threshold data to estimate the cavity round trip passive loss. Under several simplifying assumptions (low output coupling, absence of excited-state absorption, uniform pump and laser spot sizes), the threshold pump power P_{th} required to attain lasing can be expressed as [47, 71, 151]

$$P_{th} = \frac{\pi}{4}\frac{h\upsilon_p}{\sigma_{em}(\lambda_L)\tau_f}\frac{\left(\omega_L^2+\omega_P^2\right)}{\left(1-Exp\left(-\alpha_p\,\ell\right)\right)}(T+L) = A(T+L)\,, \tag{5.1}$$

where $h\upsilon_p$ is the energy of pump photons, $\sigma_{em}(\lambda_L)$ is the emission cross section at the laser wavelength, τ_f is the fluorescence lifetime of the upper laser level, ω_L and ω_p are the average values of the laser and pump spot sizes in the gain medium, $\left(1-Exp\left(-\alpha_p\,\ell\right)\right)$ is the total absorption at the pump wavelength, L is the passive round trip resonator loss, and T is the transmission of the output coupler. Collecting all the parameters in one constant, A, clearly shows that the threshold pump power is proportional to the total round trip loss L. A plot of P_{th} versus T gives a straight line and the loss L can be determined by using the best-fit values of the slope (A) and intercept (AL). In addition, using Caird analysis, one can use the experimentally measured laser slope efficiency values for different output coupler transmissions to estimate the laser passive losses as described in the previous section (by using the formula in Eq. 4.1).

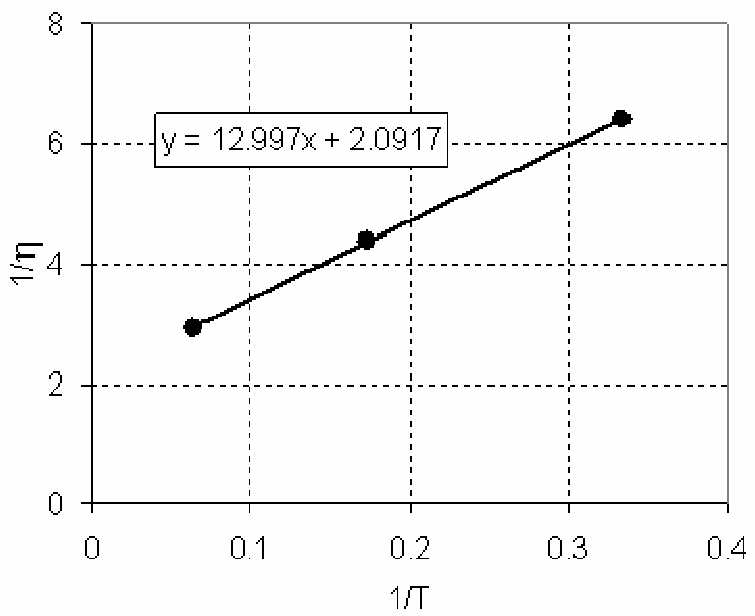

Figure 5.5: Findlay-Clay analyses of the power efficiency data showing the variation of the incident threshold pump power as a function of the output coupler transmission. L was determined to be 10.6 %.

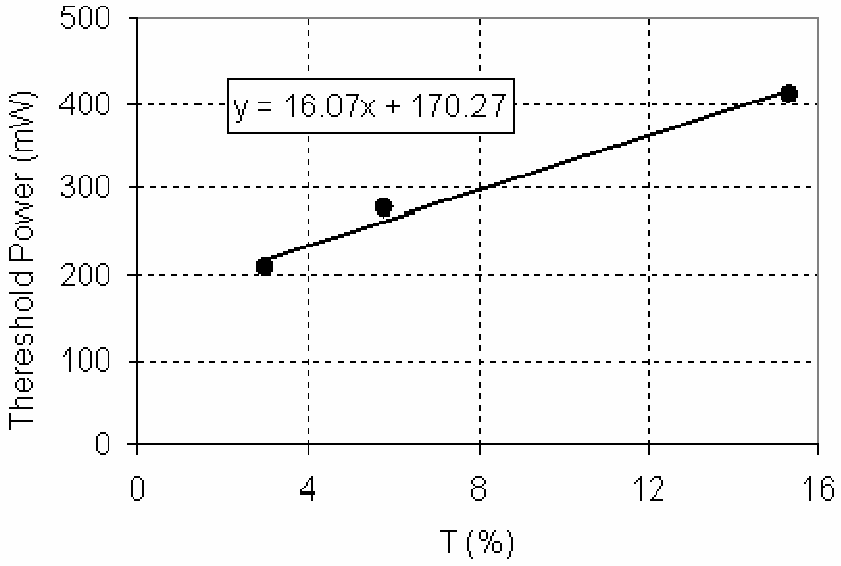

Figure 5.6: Caird analyses of the power efficiency data showing the variation of the inverse of the slope efficiency with the inverse of the output coupler transmission. L was determined to be 6.2 %.

Figure 5.5 shows the variation of the laser threshold power with output coupler transmission, and Figure 5.6 shows the dependence of the inverse of the slope efficiency ($1/\eta$) on the inverse of the output coupling ($1/T$) (Caird Plot). A linear fit to the graphs gave an L value of 10.6 % for Findlay-Clay analysis (Fig. 5.5) and 6.2 % for Caird analysis (Fig. 5.6). This disagreement between the passive round-trip cavity loss estimations with the Findlay-Clay and Caird analyses was also observed in several previous laser studies with Cr^{2+}:ZnSe [15, 27, 116, 119] gain medium, and attributed to the existence of residual ground-state absorption at the lasing wavelength [44, 86, 112, 116, 119]. Since Cr^{2+}:ZnSe medium has near unity quantum yield at room temperature [14], the existence of ground-state absorption affects only the threshold power (but not the slope efficiency) [47, 116] and Findlay-Clay analysis gave higher L values than Caird analysis [15, 27, 116, 119]. The excess part in the Findlay-Clay analysis value may be attributed to the round-trip ground state absorption loss (L_{GSA}) for this sample. The calculated value is in good agreement with previous studies [47, 116].

The stimulated emission cross section of the gain medium at the laser wavelength can be determined from the threshold data by using the formula [47, 151]

$$\sigma_{em}(\lambda_L) = \frac{\pi}{4}\frac{h\nu_P}{P_{th}\,\tau_f}\frac{\left(\omega_L^2+\omega_P^2\right)}{\left(1-\mathrm{Exp}\left(-\alpha_P\,\ell\right)\right)}\left(L+L_{GSA}+T\right) \tag{5.2}$$

In Eq. 5.2, $h\nu_P$ is the energy of pump photons, τ_f is the fluorescence lifetime of the upper laser level, P_{th} is the laser threshold pump power, ω_L and ω_p are the average values of the laser and pump spot sizes in the gain medium, and $\left(1-\mathrm{Exp}\left(-\alpha_P\,\ell\right)\right)$ is the total absorption at the pump wavelength. Findlay-Clay analysis result value of $L+L_{GSA}$ (10.6 %) determined above was used in the calculation of the stimulated emission cross section. Threshold data taken with the 3, 5.8, 15.3 % output couplers were used. The average value of σ_e came to $4.2\text{x}10^{-23}$ m^2 at the laser wavelength (around 2500 nm) where the deviation was $0.2\ \text{x}10^{-23}$ m^2. Alternatively, σ_e can be determined from the spectroscopic emission data by using the Fuchtbauer-Ladenburg formula [88, 122] given by

$$\sigma_{em}(\lambda) = \frac{\lambda^5}{8\pi c n^2 \tau_{rad}\int_{band}\lambda I_e(\lambda)\,d\lambda}I_e(\lambda) \tag{5.3}$$

Here, c is the speed of light, n is the index of refraction, τ_{rad} is the radiative lifetime, and $I_e(\lambda)$ is the fluorescence intensity signal.

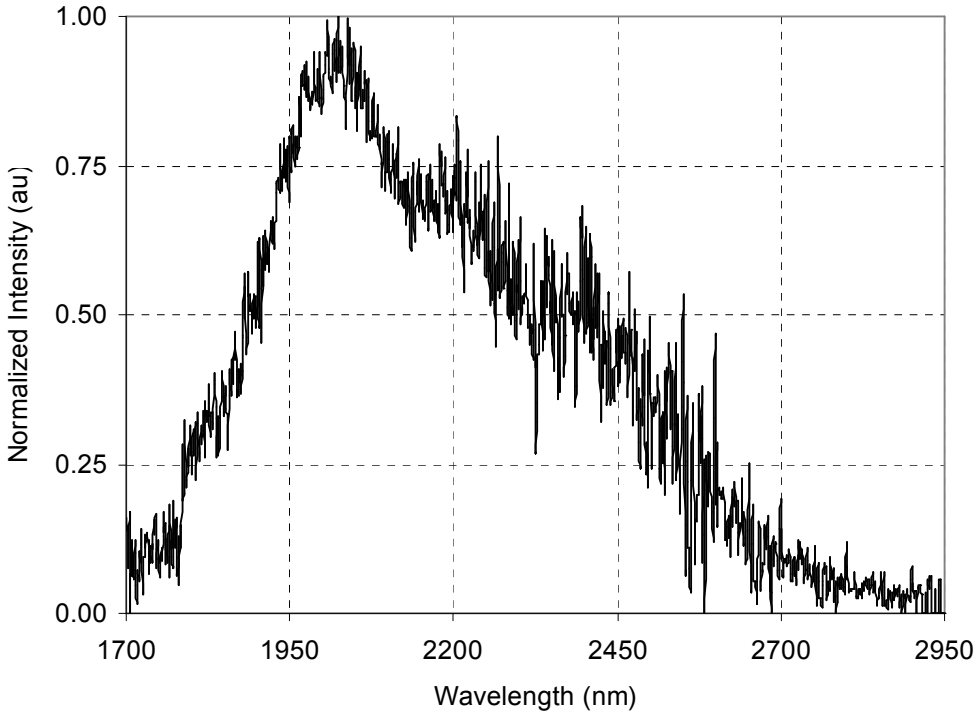

Fig 5.7. Emission spectrum of the Cr^{2+}:ZnSe medium excited with a cw Cr:YAG laser operating at 1490 nm.

Normalized emission spectrum of Cr^{2+}:ZnSe is shown in Fig. 5.7. In this measurement, the gain medium was excited at 1490 nm with a Cr^{4+}:YAG laser. A sample with a very low chromium concentration ($3x10^{18}$ cm^{-3}) was used in the emission measurement to minimize the reabsorption losses between 1.7-2 μm. The fluorescence spectrum was corrected for filter, detector and grating response. The data were used to determine the lineshape function and the area under the emission spectrum. Other parameter values appearing in the above equation are n = 2.45, τ_{rad} = 6 μs [123]. The peak of the observed emission spectrum was at a lower wavelength (around 2050 nm) than most of the previously reported values (around 2400 nm) [14, 30, 122], but came close to the peak position reported by Mirov at al. (around 2150 nm) [127]. This difference is possibly due to the

minimization of reabsorption of emitted photons in the lower wavelength side by using a sample with low density, in our case. The peak emission cross value determined using Eq. 5.3 and the measured emission spectrum gave a value of $12x10^{-23}$ m^2 (at 2050 nm) in good agreement with the previously reported values in literature [14, 44, 122, 125, 126]. However the reported peak emission wavelengths are different (around 2400 nm). At the wavelength of 2500 nm, spectroscopic data gave a value of $4.3x10^{-23}$ m^2 for σ_e, in good agreement with the laser cross section determined from threshold data.

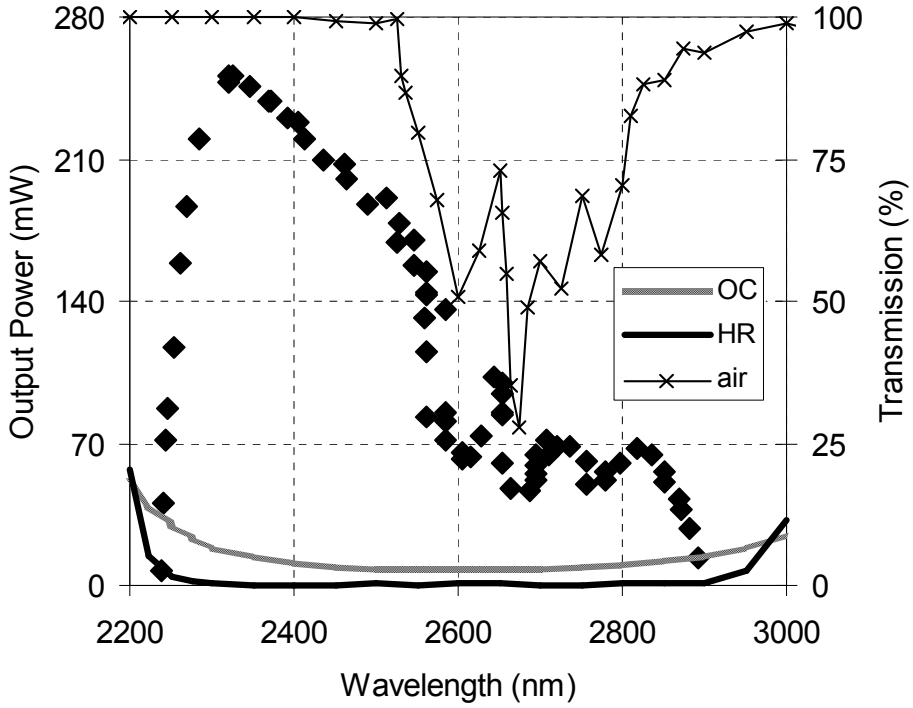

Figure 5.8. Tuning curve for the 1800-nm-pumped cw Cr^{2+}:ZnSe laser. The variation of the transmission of the output coupler and the high reflectors is also shown. The laser could be tuned between 2240 and 2900 nm. The dips in the tuning curve correspond to the atmospheric absorption lines.

Tuning characteristics of the cw Cr^{2+}:ZnSe laser was further investigated by using a Brewster-cut MgF_2 prism placed in the high-reflector arm of the resonator. The output coupler had a transmission of 3%. At the pump power of 1.8 W, the output of the laser was reduced from 255 to

250 mW after the insertion of the prism. Figure 5.8 shows the tuning curve. Without purging the cavity, broad tunability could be obtained in the 2240-2900 nm wavelength range with a single set of optics. The black and gray solid lines in Fig. 23 show the wavelength dependence of the high reflector (HR) and output coupler transmissions (OC), respectively. Tuning on both sides was limited with the reflectivity bandwidth of the high reflectors. In these measurements, the relative humidity was 67%. A rough estimate of the transmission of air at that humidity level is also shown [152]. Note that the observed dips near the wavelength of 2600 nm coincide with the atmospheric absorption peaks.

5.3 Concentration Dependence of CW Laser Performance

In the second set of experiments, we investigated the effect of active ion concentration on the cw power performance of the Cr^{2+}:ZnSe laser. Here, several Cr^{2+}:ZnSe samples with different Cr^{2+} concentration were used. Properties of the samples are summarized in Table 5.2.

Sample No	Length (mm)	α_{p0} @ 1775 nm (cm^{-1})	Average Cr^{2+} Concentration ($x10^{18}$ ions /cm^3)	Fluorescence Lifetime (μs)	Small Signal Pump Absorption @ 1800 nm (%)
pure	-	0	0	-	0
1	1.94	0.9	0.8	5.5	16
2	1.86	2.5	2.2	5.2	40
3	1.92	3.1	2.7	5.1	46
4	1.95	4.6	4.0	5.1	61
5	1.94	6.5	5.7	5.0	72
6	1.77	9.7	8.5	4.3	82
7	1.85	12.2	10.6	4.3	88
8	1.80	14.7	12.8	3.8	93
9	1.93	26.7	23.2	2.4	99

Table5.2. Length, small-signal peak absorption coefficient (α_{p0} at 1775 nm), average Cr^{2+} ion concentration, fluorescence lifetime and small signal pump absorption of the nine polycrystalline Cr^{2+}:ZnSe samples used in lasing experiments.

Chromium was incorporated into 2-mm-thick polycrystalline ZnSe samples by diffusion doping. All of the samples were prepared at 1000 °C. By varying the diffusion time, samples with average Cr^{2+} concentration between $0.8x10^{18}$ and 23.2 $x10^{18}$ ions /cm^3 were prepared. The laser setup was similar to what was described above. Figure 5.9 shows the variation of the output power

as a function of the incident pump power for 5 different Cr^{2+}:ZnSe samples (Samples 1, 2, 4, 8, and 9). Efficiency curves of the other samples were not included to simplify the appearance of Fig. 5.9. The laser performance varied significantly from sample to sample and the best power performance was obtained with sample 4. Sample 4 has a Cr^{2+} concentration of $4x10^{18}$ ions/cm^3, a fluorescence lifetime of 5.1 μs, and an absorption of about 60 % at 1800 nm. With sample 4, as high as 256 mW of output power was obtained with 3.7 W of incident pump power. The corresponding threshold pump power and the incident power slope efficiency were 340 mW and 8 %, respectively.

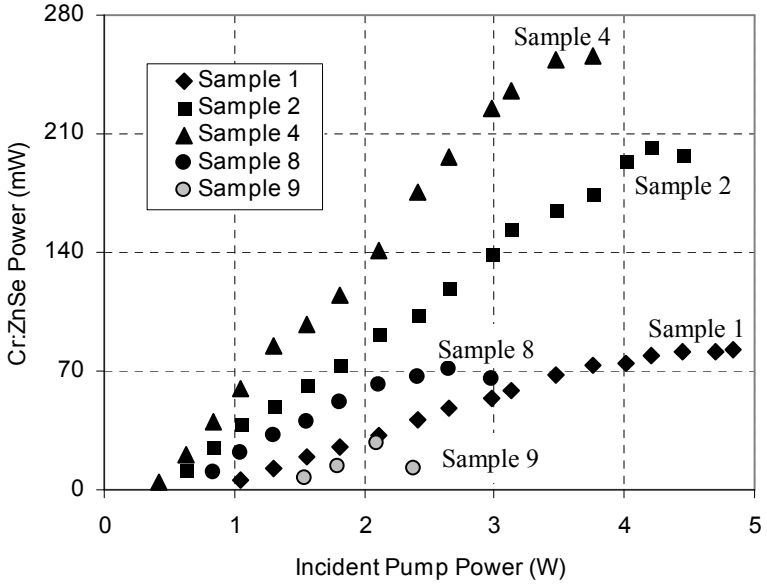

Figure 5.9: CW Cr^{2+}:ZnSe laser output power as a function of incident pump power taken with a 3 % OC, for Cr^{2+}:ZnSe samples 1, 2, 4, 8, and 9. Spectroscopic properties of the samples are listed in Table 5.1.

To better visualize and investigate the concentration dependence of laser performance, Fig. 5.10-5.12 were prepared using the laser slope efficiency curves. Figure 5.10 shows the variation of maximum attainable laser output power with Cr^{2+} concentration at an incident pump power of 2.1 W. The results indicate that for samples with a thickness of 2 mm, the best laser performance could be obtained with the samples having a Cr^{2+} concentration of 5 to$10x10^{18}$ ions/cm^3. For samples having chromium concentrations outside of this interval, either the chromium concentration is too

low to absorb enough of the pump, or the chromium concentration is too high such that deleterious effects such as lifetime reduction and increased passive losses degrades laser performance.

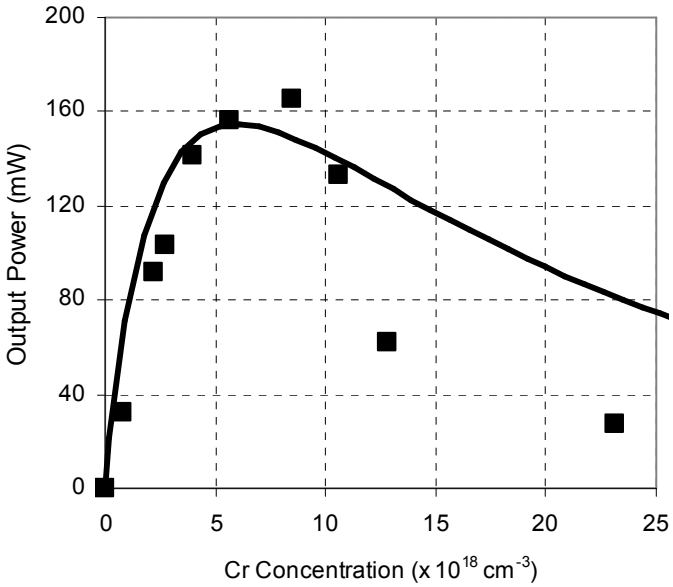

Figure 5.10: Square dots are the experimentally measured Cr^{2+}:ZnSe laser output power values at an incident pump power of 2.1 W, for the 9 different Cr^{2+}:ZnSe samples used in the lasing experiments (samples 1-9 in table 1). The data is shown as a function of active Cr^{2+} ion concentration. The solid line is the expected laser performance trend based on the fluorescence efficiency measurements.

To delineate this issue further, Figure 5.11 and 5.12 show the measured variation of threshold pump power and incident slope efficiency with Cr^{2+} concentration, respectively. As can be seen from Fig. 5.11, with increasing Cr^{2+} concentration, measured threshold pump power level first decreases due to the increasing amount of pump absorption. However, it starts to saturate and then increase due to the increase of passive losses at the lasing wavelength as well as the decrease in fluorescence lifetime. A similar trend was observed in the variation of the measured slope efficiency value (Fig. 5.12). The optical to optical conversion efficiency first increases with increasing pump absorption, and at high concentration values, a sharp decrease is observed due the mentioned effects.

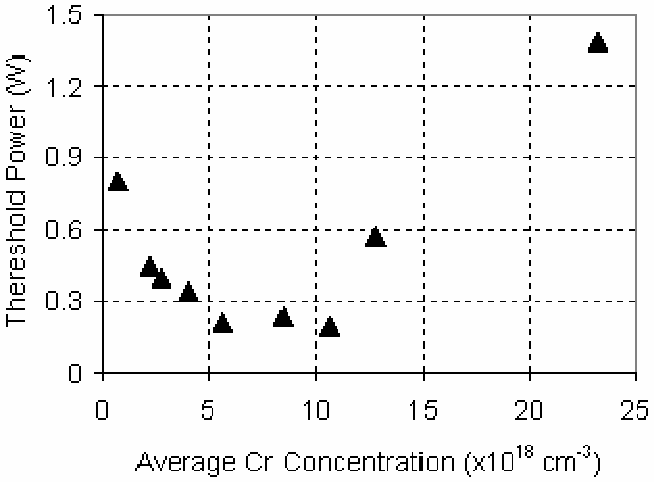

Figure 5.11: Experimentally measured variation of incident threshold pump power with Cr^{2+} concentration for 9 different Cr^{2+}:ZnSe samples used in the lasing experiments.

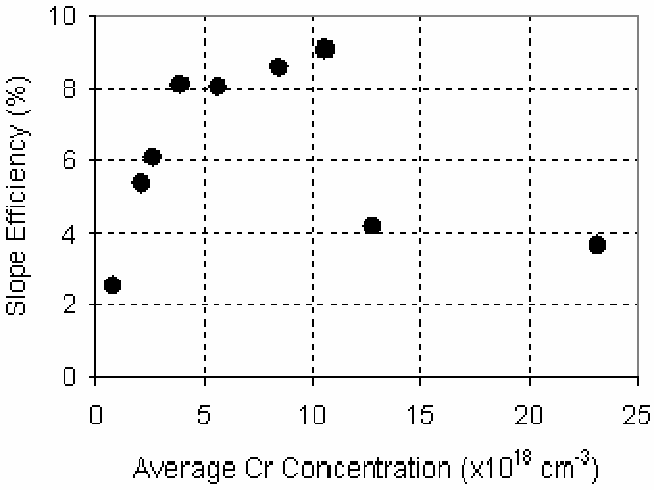

Figure 5.12: Experimentally measured variation of laser slope efficiency with respect to incident pump power as a function of Cr^{2+} concentration for the 9 different Cr^{2+}:ZnSe samples used in the lasing experiments.

The solid line in Fig. 5.10 is the estimated laser performance based on the fluorescence efficiency measurements for a hypothetical 2-mm-thick Cr^{2+}:ZnSe sample (from section 3.3, Fig.

3.10). The measured laser performance agrees very well with the fluorescence analysis estimate for low concentration values. However, for the highly doped samples, experimentally observed laser output power levels are lower than fluorescence analysis estimates. This is because laser power estimate based on fluorescence analysis does not consider the thermal load on the gain medium.

Detailed analysis of the effect of thermal loading on the laser parameters can be found in previous studies[145, 147, 153-155]. To analyze the effect in a rough manner, one can consider the pump-induced heating of the gain medium which is directly proportional to the heating fraction of the medium

$$\eta_h(T) = \left(1 - \frac{\lambda_p}{\lambda_L}\frac{\tau_f(T)}{\tau_r}\right) \tag{5.4}$$

where λ_p and λ_L are the respective pump and laser wavelengths, $\tau_f(T)$ is the fluorescence lifetime at a temperature of T, and τ_r is the radiative lifetime. As an example, at a temperature of 15 °C, the heating fraction of sample 1 is only 0.27, where the heating fraction of sample 9 is 0.67. Besides, as the secondary effect one must also consider the decrease in the fluorescence lifetime with temperature ($\tau_f(T)$). For a sample with a high initial heating fraction, the medium heats up rapidly, and the fluorescence lifetime decreases (Section 3.2.3, Fig. 3.8). The decrease in fluorescence lifetime further increases the heating fraction and the thermal load on the medium.

To investigate the effect quantitatively we use the analysis described in a previous work[153]. At an incident pump power of 5 W, and at a boundary temperature of 15 °C we estimate that the average temperature at the laser active region inside the gain medium reaches only up to 30 °C in sample 1. However, due to its low quantum efficiency average temperature inside sample 9 can increase above 80 °C, where considerable amount of decrease in fluorescence lifetime is seen. Moreover, under thermal loading, due to due to the large refractive index derivative (dn/dT) of the Cr^{2+}:ZnSe material, thermal lensing will also play a crucial role in laser performance. These two effects are the main factors that degrade the laser power performance for highly doped samples.

Chapter 6

CONCLUSIONS

In this thesis, we have provided a comprehensive review of the work on the development of Cr^{2+}:ZnSe lasers. A detailed account of the preparation methods and spectroscopic characterization techniques was presented. Diffusion doping was described in detail and various methods for the determination of the diffusion coefficient were discussed. Pulsed and continuous-wave operations of the Cr^{2+}:ZnSe lasers were also reviewed. Overall, the studies performed in our group delineated the effect of active ion concentration on passive losses, fluorescence efficiency, fluorescence lifetime, and power performance. The results indicate that chromium concentrations of less than $10x10^{18}$ ions/cm^3 are more suitable for obtaining efficient lasing especially in the cw regime. Related to this, we note that the best route to power scaling in cw Cr^{2+}:ZnSe lasers is through use of pump lasers operating as close to the peak absorption wavelength at 1775 nm as possible. This makes it possible to obtain a desired level of pump absorption with the least possible chromium concentration and hence minimizes several deleterious thermal loading problems that can arise during high-power operation.

APPENDIX A

THEORETICAL MODELING of THERMAL DIFFUSION

In this section, we will present a more detailed description of the solution of the diffusion equation in cylindrical coordinates. As described in Section 2, all of the ZnSe wafers that we used were in the form of short cylinders. In order to model diffusion in this geometry, we need to solve Fick's second equation in cylindrical geometry, with prescribed initial and boundary conditions. Imagine a finite cylinder with thickness 2L and radius R, ($-L < z < L$, $0 \leq r < R$), with its center at the origin as demonstrated in Fig. A.1.

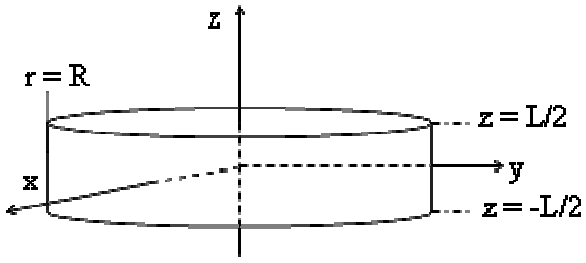

Figure A.1. Sketch of the cylindrical sample with thickness L and radius R ($-L/2 < z < L/2$, $0 \leq r < R$). The center of the sample coincides the origin.

Placing the center of the cylinder at the origin of the coordinate system will make the solution symmetric. In our problem, we have initially zero diffused material concentration inside the ZnSe sample. Also, during the diffusion, we have constant dopant material surface concentration, n_o, so mathematical statement of our problem is

$$\left(\frac{1}{\mathrm{r}}\frac{\partial}{\partial \mathrm{r}}\left(\mathrm{r}\frac{\partial \mathrm{N}(\mathrm{r},\mathrm{z},\mathrm{t})}{\partial \mathrm{r}}\right)+\frac{\partial^2 \mathrm{N}(\mathrm{r},\mathrm{z},\mathrm{t})}{\partial \mathrm{z}^2}\right)-\frac{1}{\mathrm{D}}\frac{\partial \mathrm{N}(\mathrm{r},\mathrm{z},\mathrm{t})}{\partial \mathrm{t}}=0 \tag{A.1}$$

$$N(\mathrm{r},\mathrm{z},\mathrm{t}=0)=0, \quad \text{(IC)} \tag{A.2}$$

$$N(\mathrm{r}=\mathrm{a},\mathrm{z},\mathrm{t}>0)=n_{\mathrm{o}}, \qquad N(\mathrm{r},\mathrm{z}=\pm L,\mathrm{t}>0)=n_{\mathrm{o}} \quad \text{(BC).} \tag{A.3}$$

In Eq. A.1, $N(\mathrm{r},\mathrm{z},\mathrm{t})$ is the diffused material concentration, r and z are cylindrical position coordinates, t is time and D is diffusion coefficient. Also notice that, in Eq. A.1, we excluded the θ dependent terms since our problem is symmetric in θ.

The first step in solving this problem is reducing the problem into a case where all boundaries are kept at zero dopant concentration, by putting

$$N(\mathrm{r},\mathrm{z},\mathrm{t})=n_{\mathrm{o}}\left(U(\mathrm{r},\mathrm{z})+W(\mathrm{r},\mathrm{z},\mathrm{t})\right), \tag{A.4}$$

where $U(\mathrm{r},\mathrm{z})$ and $W(\mathrm{r},\mathrm{z},\mathrm{t})$ satisfy the following equations

$$\left(\frac{1}{\mathrm{r}}\frac{\partial}{\partial \mathrm{r}}\left(\mathrm{r}\frac{\partial U(\mathrm{r},\mathrm{z})}{\partial \mathrm{r}}\right)+\frac{\partial^2 U(\mathrm{r},\mathrm{z})}{\partial \mathrm{z}^2}\right)=0 \tag{A.5}$$

$$U(\mathrm{r}=R,\mathrm{z})=1, \qquad U(\mathrm{r},\mathrm{z}=\pm L)=1 \quad \text{for t>0} \quad \text{(BC).} \tag{A.6}$$

and

$$\left(\frac{1}{\mathrm{r}}\frac{\partial}{\partial \mathrm{r}}\left(\mathrm{r}\frac{\partial W(\mathrm{r},\mathrm{z},\mathrm{t})}{\partial \mathrm{r}}\right)+\frac{\partial^2 W(\mathrm{r},\mathrm{z},\mathrm{t})}{\partial \mathrm{z}^2}\right)-\frac{1}{\mathrm{D}}\frac{\partial W(\mathrm{r},\mathrm{z},\mathrm{t})}{\partial \mathrm{t}}=0 \tag{A.7}$$

$$W(\mathrm{r},\mathrm{z},\mathrm{t}=0)=-U(r,z), \quad \text{(IC)} \tag{A.8}$$

$$W(\mathrm{r}=\mathrm{a},\mathrm{z},\mathrm{t})=0, \qquad W(\mathrm{r},\mathrm{z}=\pm L,\mathrm{t})=0 \quad \text{for t>0} \quad \text{(BC).} \tag{A.9}$$

One can solve $U(\mathrm{r},\mathrm{z})$ immediately as

$$U(r,z)=1. \tag{A.10}$$

After this substitution, the solution of $W(r,z,t)$, which we have zero dopant concentration as the boundary condition, can be expressed as products of the solutions of simpler problems, namely

$$W(r,z,\mathrm{t})_{short\_cylinder}=W(\mathrm{r},\mathrm{t})_{\mathrm{inf}\,inite\_cylinder}\times W(z,\mathrm{t})_{\mathrm{inf}\,inite\_slab} \tag{A.11}$$

Note that we can not write the solution of $N(\mathrm{r},\mathrm{z},\mathrm{t})$ as a product of simpler problem solutions since it has nonzero boundary conditions, thus substitution of Eq. A.4 is necessary. In Eq. A.11 $W(z,\mathrm{r},\mathrm{t})_{short\_cylinder}$ is the solution that we are seeking, $W(z,\mathrm{t})_{\mathrm{inf}\,inite\_slab}$ is the solution of diffusion equation for an infinite slab with thickness of 2L (between – L and L)

$$\frac{\partial^2 W(z,t)}{\partial z^2}-\frac{1}{\mathrm{D}}\frac{\partial W(z,t)}{\partial \mathrm{t}}=0 \quad (-\mathrm{L}<\mathrm{z}<\mathrm{L}), \tag{A.12}$$

$$W(z,t=0)=0\,,\ (\mathrm{IC}) \tag{A.13}$$

$$W(\mathrm{z}=\pm L,t)=1\,,\ (\mathrm{BC}) \tag{A.14}$$

and $W(\mathrm{r},\mathrm{t})_{\mathrm{inf}\,inite\_cylinder}$ is the solution of diffusion equation for an infinite cylinder with radius R

$$\left(\frac{\partial^2 W(r,t)}{\partial \mathrm{r}^2}+\frac{1}{\mathrm{r}}\frac{\partial W(r,t)}{\partial \mathrm{r}}\right)-\frac{1}{D}\frac{\partial W(r,t)}{\partial \mathrm{t}}=0 \quad (0<\mathrm{r}<\mathrm{R}), \tag{A.15}$$

$$W(r=R,t)=1\,,\ (\mathrm{BC}) \tag{A.16}$$

$$W(r,t=0)=0\,,\ (\mathrm{IC}). \tag{A.17}$$

In solving $W(\mathrm{r},\mathrm{t})_{\mathrm{inf}\,inite\_cylinder}$ and $W(z,\mathrm{t})_{\mathrm{inf}\,inite\_slab}$, one can use separation of variables technique, (details of the solutions of these kind of problems can be found in the book by Carslaw, and Jaeger [108]), and get

$$W(z,t)_{\mathrm{inf}\,inite\_slab}=-\frac{4}{\pi}\sum_{n=0}^{\infty}\frac{(-1)^n}{(2n+1)}e^{\left(-\frac{(2n+1)^2\pi^2}{4L^2}Dt\right)}Sin\left(\frac{(2n+1)\pi}{2L}z\right) \tag{A.18}$$

$$W(\mathrm{r},\mathrm{t})_{\mathrm{inf}\,inite\_cylinder}=\frac{2}{R}\sum_{m=1}^{\infty}\mathrm{Exp}\left(-\mathrm{D}\alpha_{\mathrm{n}}^2\mathrm{t}\right)\frac{\mathrm{J}_0(\mathrm{r}\alpha_m)}{\alpha_m\,\mathrm{J}_1(R\alpha_m)}. \tag{A.19}$$

In equation A.18, $\mathrm{J}_0(x)$ is the Bessel function of order zero of the first kind, α_m is the m[th] positive root of $\mathrm{J}_0(ax)=0$ and $\mathrm{J}_1(x)$ is the Bessel function of order one of the first kind. Now, substituting A.18 and A.19 into A.11, we get $W(\mathrm{r},\mathrm{z},\mathrm{t})$ as

$$W(r,z,t) = -\frac{8}{\pi R}\sum_{m=1}^{\infty}\sum_{n=0}^{\infty}\frac{(-1)^n J_0(r\alpha_m)}{(2n+1)\alpha_m J_1(R\alpha_m)}\cos\left(\frac{(2n+1)\pi}{2L}z\right)e^{\left(-\left(\frac{(2n+1)^2\pi^2}{4L^2}+\alpha_n^2\right)Dt\right)}. \quad (A.20)$$

Then, substituting A.10 and A.20 into A.4, we finally get $N(r,z,t)$ as

$$N(r,z,t) = n_0 - \frac{8n_0}{\pi R}\sum_{m=1}^{\infty}\sum_{n=0}^{\infty}\frac{(-1)^n J_0(r\alpha_m)}{(2n+1)\alpha_m J_1(R\alpha_m)}\cos\left(\frac{(2n+1)\pi}{2L}z\right)e^{\left(-\left(\frac{(2n+1)^2\pi^2}{4L^2}+\alpha_n^2\right)Dt\right)}. \quad (A.21)$$

VITA

Umit Demirbas was born in Egirdir, Isparta, in December 1979. He received his BS degrees both in Physics and Electrical-Electronics Engineering from Koç University, Istanbul, in 2004. In September 2004, he entered Materials Science and Engineering Department of Koç University where he currently is working towards his MS degree. His research interests include mid-infrared solid-state lasers and spectroscopy of novel laser and amplifier media. He will continue his Ph.D. work at Massachusetts Institute of Technology, at the Department of Electrical Engineering and Computer Science.

List of Publications:

Book Chapter

- Alphan Sennaroglu and Umit Demirbas "Tunable Cr^{2+}:ZnSe Lasers in the Mid Infrared", Chapter in Handbook of Solid-State Lasers and Applications, CRC Press, Editors: Alphan Sennaroglu, (in press).

Journal Articles

- Alphan Sennaroglu, Umit Demirbas, Nathalie Vermeulen, Heidi Ottevaere & Hugo Thienpont, "Continuous-Wave Broadly Tunable Cr^{2+}:ZnSe Laser Pumped by a Thulium Fiber Laser", Optics Communications, (accepted).
- Umit Demirbas and Alphan Sennaroglu "Intracavity-pumped Cr^{2+}:ZnSe laser with ultrabroad tuning range between 1880 and 3100 nm ", Optics Letters, (in press).

- Alphan Sennaroglu, Umit Demirbas, Adnan Kurt & Mehmet Somer, "Concentration Dependence of Fluorescence and Lasing Efficiency in Cr:ZnSe Lasers", Optical Materials, (in press).
- Umit Demirbas, Adnan Kurt, Alphan Sennaroglu, Emel Yilgor & Iskender Yilgor "Luminescent Nd^{3+} Doped Silicone-Urea Copolymers", Polymer, 47, 982-990 (2006).
- Alphan Sennaroglu, Umit Demirbas, Sarper Ozharar & Fatih Yaman, "Accurate Determination of Saturation Parameters for Cr^{4+}:Doped Solid-State Saturable Absorbers", JOSA B, 23, 241-249 (2006).
- Umit Demirbas, Alphan Sennaroglu & Mehmet Somer, "Synthesis and Characterization of Diffusion-Doped Cr^{2+}:ZnSe and Fe^{2+}:ZnSe", Optical Materials, 28, 231-240 (2006).
- Alphan Sennaroglu, Idris Kabalci, Adnan Kurt, Umit Demirbas & Gonul Ozen, "Spectroscopic Properties of Tm^{3+}:TeO_2-PbF_2 glasses", Journal of Luminescence, 116, 79-86 (2006).

International Conference Articles and Presentations

- Umit Demirbas, Alphan Sennaroglu, Nathalie Vermeulen, Heidi Ottevaere & Hugo Thienpont, "Continuous-Wave Fiber-Pumped Cr:ZnSe Laser", Conference on Solid-State Lasers and Amplifiers, Photonics Europe 2006, (Strasbourg, France, 3-7 April 2006).
- Iskender Yilgor, Umit Demirbas, Alphan Sennaroglu, Adnan Kurt & Emel Yilgor, "Luminescent Nd^{3+} Doped Thermoplastic Silicone-Urea Copolymers", Division of Polymeric Materials: Science and Engineering for the 231st American Chemical Society National Meeting, Atlanta, March 26-30, 2006.
- Umit Demirbas, Adnan Kurt, Alphan Sennaroglu, Emel Yilgor & Iskender Yilgor, "Luminescence Characteristics of Nd^{3+} Doped Silicone-Urea Copolymers", Advanced Solid-State Photonics Topical Meeting, (Optical Society of America, Nevada, USA, January 29-February 1, 2006).

- Umit Demirbas, Alphan Sennaroglu, Adnan Kurt & Mehmet Somer, "Influence of Active Ion Concentration on Fluorescence Efficiency and Lasing Performance in Cr^{2+}:ZnSe Lasers", 18th Annual Lasers and Electro Optics Society Meeting, (Sydney, Australia , 23 – 27 October 2005).
- Umit Demirbas, Alphan Sennaroglu, Adnan Kurt & Mehmet Somer, "Preparation and Spectroscopic Investigation of Diffusion-Doped Fe^{2+}:ZnSe and Cr^{2+}:ZnSe", Advanced Solid-State Photonics Topical Meeting, (Optical Society of America, Vienna, Austria, 2005).
- Kabalci, G. Ozen, A. Kurt, U. Demirbas, A. Sennaroglu, 'Spectroscopic properties of Tm^{3+}:TeO_2-PbF_2 glasses in the near infrared,' (a) Conference on Solid-State Lasers and Amplifiers, Photonics Europe 2004, paper 5460-25 (26-30 April, 2004, Strasbourg, France); (b) in Solid State Lasers and Amplifiers, edited by Alphan Sennaroglu, James G. Fujimoto, and Clifford R. Pollock, Proceedings of SPIE Vol. 5460 (SPIE, Bellingham, WA, 2004) 195-203.

National Conference Articles and Presentations

- Alphan Sennaroglu, Umit Demirbas, Mehmet Somer & Adnan Kurt, "Orta Kızılaltı Bölgesinde Çalışan Cr^{+2}:ZnSe Laserleri" (Oral presentation at 7th Turkish Workshop on Electro-Optics and Photonics, Bilkent University, Istanbul, December 12, 2005).
- Umit Demirbas, Alphan Sennaroglu & Mehmet Somer, "2.6 μm'de Çalışan Nanosaniye Darbeli Cr^{2+}: ZnSe Laseri" (Poster presentation at 6th Turkish Workshop on Electro-Optics and Photonics, Sabancı University, Istanbul, December 10, 2004).
- Umit Demirbas, Alphan Sennaroglu & Mehmet Somer, "Cr^{+2}:ZnSe ve Fe^{+2}:ZnSe Kizilalti Laser Malzemelerinin Sentezi ve Spektroskopik Incelenmesi" (Oral presentation given during 5th Turkish Workshop on Electro-Optics and Photonics, Middle East Technical University, Ankara, December 12, 2003).
- Idris Kabalci, Gonul Ozen, Adnan Kurt, Umit Demirbas & Alphan Sennaroglu, "Tm^{+3} Katkili (1-x) TeO_2-(x)PbF_2 Camlarinin Yakin-Kizilalti Bolgesindeki Spektroskopik

Ozellikleri" (Poster presentation at 5th Turkish Workshop on Electro-Optics and Photonics, Middle East Technical University, Ankara, December 12, 2003).

Other Publications

- Alphan Sennaroglu, Umit Demirbas, Mehmet Somer, Adnan Kurt, ve Clifford R. Pollock, 'Kızılaltı Katıhal Laser Malzemelerinin Sentezi ve Spektroskopik İncelenmesi' (Synthesis and Spectroscopic Investigation of Infrared Laser Materials) Tubitak Report No. TBAG-2030 (101T051), January 2005.

BIBLIOGRAPHY

[1] S. Adachi and T. Taguchi, "Optical Properties of ZnSe," *Physical Review B*, vol. 43, pp. 9569-9577, 1991.

[2] I. T. Sorokina, "Cr^{2+}-doped II-VI materials for lasers and nonlinear optics," *Optical Materials*, vol. 26, pp. 395-412, 2004.

[3] E. M. Gavrushchuk, "Polycrystalline zinc selenide for IR optical applications," *Inorganic Materials*, vol. 39, pp. 883-898, 2003.

[4] H. A. Weakliem, "Optical spectra of Ni^{2+}, Co^{2+}, and Cu^{2+} in tetrehedral sites in crystals," *The Journal of Chemical Physics*, vol. 36, pp. 2117-2140, 1961.

[5] J. M. Baranowski, J. W. Allen, and G.L.Pearson, "Crystal-Field Spectra of $3d^n$ Impurities in II-VI and III-V Compound Semiconductors," *Physical Review*, vol. 160, pp. 627-632, 1967.

[6] G. A. Slack, F. S. Ham, and R. M. Cherenko, "Optical Absorption of Tetrahedral Fe^{2+} (cd^6) in Cubic ZnS, CdTe, and $MgAl_2O_4$," *Physical Review*, vol. 152, pp. 376-402, 1966.

[7] G. A. Slack and B. M. Omera, "Infrared Luminescence of Fe^{2+} in ZnS," *Physical Review*, vol. 163, pp. 335-341, 1967.

[8] G. A. Slack, S. Roberts, and F. S. Ham, "Far-Infrared Optical Absorption of Fe^{2+}: in ZnS," *Physical Review*, vol. 155, pp. 170-177, 1967.

[9] R. Pappalardo and R. E. Dietz, "Absorption spectra of transition ions in CdS crystals," *Physical Review*, vol. 123, pp. 1188-1203, 1961.

[10] J. T. Vallin, G. A. Slack, S. Roberts, and A. E. Hughes, "Infrared Absorption in Some II-VI Compounds Doped with Cr," *Physical Review B*, vol. 2, pp. 4313-4333, 1970.

[11] J. T. Vallin and G. D. Watkins, "EPR of Cr^{2+} in II-VI lattices," *Physical Review B*, vol. 9, pp. 2051-2072, 1974.

[12] W. Low and M. Weger, "Paramagnetic resonance and optical spectra of divalent iron in cubic fields. I. Theory," *Physical Review*, vol. 118, pp. 1119-1130, 1960.

[13] W. Low and M. Weger, "Paramagnetic resonance and optical spectra of divalent iron in cubic fields. I. Experimental Results," *Physical Review*, vol. 118, pp. 1130-1136, 1960.

[14] L. D. DeLoach, R. H. Page, G. D. Wilke, S. A. Payne, and W. F. Krupke, "Transition Metal-Doped Zinc Chalcogenides Spectroscopy and Laser Demonstration of a New Class of Gain Media," *IEEE Journal of Quantum Electronics*, vol. 32, pp. 885-895, 1996.

[15] R. H. Page, K. I. Schaffers, L. D. DeLoach, G. D. Wilke, F. D. Patel, J. B. TassanoJr., S. A. Payne, W. F. Krupke, K.-T. Chen, and A. Burger, "Cr^{2+} Doped Zinc Chalcogenides as Efficient, Widely Tunable Mid-Infrared Lasers," *IEEE Journal of Quantum Electronics*, vol. 33, pp. 609-619, 1997.

[16] J. McKay and K. L. Schepler, "Kilohertz, 2.6-μm Cr^{2+}:CdSe laser," presented at Advanced Solid-State Lasers, Boston, 1999.

[17] J. McKay, K. L. Schepler, and G. C.Catella, "Efficient grating-tuned mid-infrared Cr^{2+}:CdSe laser," *Optics Letters*, vol. 24, pp. 1575-1577, 1999.

[18] J. B. McKay, W. B. Roh, and K. L. Schepler, "Extended mid-IR tuning of a Cr^{2+}:CdSe laser," presented at Advanced Solid State Photonics, Quebe, 2002.

[19] A. G. Bluiett, U. Hommerich, R. T. Shah, S. B. Trivedi, S. W. Kutcher, and C. C. Wang, "Observation of lasing from Cr^{2+}:CdTe and compositional effects in Cr^{2+}-doped II-VI semiconductors," *Journal of Electronic Materials*, vol. 31, pp. 806-810, 2002.

[20] I. T. Sorokina, E. Sorokin, A. D. Lieto, M. Tonelli, B. N. Mavrin, and E. A. Vinogradov, "A new broadly tunable room temperature continuous-wave Cr^{2+}:ZnS_xSe_{1-x} laser," presented at Advanced Solid State Photonics, Vienna, Austria, 2005.

[21] U. Hommerich, X. Wu, V. R. Davis, S. B. Trivedi, K. Grasza, R. J. Chen, and S. Kutcher, "Demonstration of room-temperature laser action at 2.5 μm from Cr^{2+}:$Cd_{0.85}Mn_{0.15}Te$," *Optics Letters*, vol. 22, pp. 1180-1182, 1997.

[22] U. Hömmerich, J. T. Seo, A. Bluiett, D. Temple, S. B. Trivedi, H. Zong, S. W. Kutcher, C. C. Wang, R. J. Chen, and B. Schumm, "Mid-infrared laser development based on transition metal doped cadmium manganese telluride," *Luminescence*, pp. 1143-1145, 2000.

[23] S. B. Trivedi, S. W. Kutcher, C. C. Wang, G. V. Jagannathan, U. Hommerich, A. Bluiett, M. Turner, J. T. Seo, K. L. Schepler, B. Schumm, P. R. Boyd, and G. Green, "Transition metal doped cadmium manganese telluride: a new material for tunable mid-infrared lasing," *Journal of Electronic Materials*, vol. 30, pp. 728-732, 2001.

[24] J. T. Seo, U. Hommerich, H. Zong, S. B. Trivedi, S. W. Kutcher, C. C. Wang, and R. J. Chen, "Mid-Infrared lasing from a novel optical material: chromium-doped $Cd_{0.55}Mn_{0.45}Te$," *Phys. Stat. Sol.*, vol. 175, pp. R3, 1999.

[25] J. T. Seo, U. Hömmerich, S. B. Trivedi, R. J. Chen, and S. Kutcher, "Slope efficiency and tunability of Cr^{2+}:$Cd_{0.85}Mn_{0.15}Te$ mid-infrared laser," *Optical Communications*, pp. 267-270, 1998.

[26] P. Cerny, H. Sun, D. Burns, U. N. Roy, and A. Burger, "Spectroscopic investigation and continuous wave laser demonstration utilizing single crystal Cr^{2+}:CdZnTe," presented at Advanced Solid-State Photonics, Vienna, Austria, 2005.

[27] G. J. Wagner, T. J. Carrig, R. H. Page, K. I. Schaffers, J. Ndap, X. Ma, and A. Burger, "Continuous-wave broadly tunable Cr^{2+}:ZnSe laser," *Optics Letters*, vol. 24, pp. 19-21, 1999.

[28] R. H. Page, J. A. Skidmore, K. I. Schaffers, R. J. Beach, S. A. Payne, and W. F. Krupke, "Demonstrations of diode-pumped grating-tuned ZnSe:Cr^{+2} lasers," presented at OSA TOPS, Advanced Solid-State Lasers, Orlando, 1997.

[29] T. J. Carrig, G. J. Wagner, A. Sennaroglu, J. Y. Jeong, and C. R. Pollock, "Mode-locked Cr^{2+}:ZnSe laser," *Optics Letters*, vol. 25, pp. 168-170, 2000.

[30] E. Sorokin, S. Naumov, and I. T. Sorokina, "Ultrabroadband infrared solid-state lasers," *IEEE Journal of Selected Topics in Quantum Electronics*, vol. 11, pp. 690-712, 2005.

[31] G. J. Wagner, B. G. Tiemann, W. J. Alford, and T. J. Carring, "Single-Frequency Cr:ZnSe Laser," presented at OSA Advanced Solid-State Photonics, New Mexico, 2004.

[32] U. Demirbas and A. Sennaroglu, "Intracavity-pumped Cr^{2+}:ZnSe laser with ultrabroad tuning range between 1880 and 3100 nm," *Optics Letters*, 2006 in press.

[33] C. Fischer, E. Sorokin, I. T. Sorokina, and M. W. Sigrist, "Photoacoustic monitoring of gases using a novel laser source tunable around 2.5 μm," *Optics and Lasers in Engineering*, vol. 43, pp. 573-582, 2005.

[34] T. J. Carrig, A. K. Hankla, G. J. Wagner, C. B. Rawle, and I. T. M. Kinnie, "Tunable infrared laser sources for DIAL," presented at Laser Radar Technology and Applications VII, Proceedings of SPIE, 2002.

[35] E. Sorokin, I. T. Sorokina, C. Fischer, and M. W. Sigrist, "Widely tunable Cr^{2+}:ZnSe laser source for trace-gas sensing," presented at Advanced Solid State Photonics, Vienna, Austria, 2005.

[36] N. Picque, F. Gueye, G. Guelachvili, E. Sorokin, and I. T. Sorokina, "Time-resolved Fourier transform intracavity spectroscopy with a Cr^{2+}:ZnSe laser," *Optics Letters*, vol. 30, pp. 3410-3412, 2005.

[37] V. A. Akimov, V. I. Kozlovskii, Y. V. Korostelin, A. I. Landman, Y. P. Podmar'kov, and M. P. Frolov, "Spectral dynamics of intracavity absorption in a pulsed Cr^{2+}:ZnSe laser," *Quantum Electronics*, vol. 35, pp. 425-428, 2005.

[38] F. K. Tittel, D. Richter, and A. Fried, "Mid-Infrared Laser Applications in Spectroscopy," in *Solid-State Mid-Infrared Laser Sources*, vol. 89, *Springer Topics in Applied Physics*, I. T. Sorokina and K. L. Vodopyanov, Eds. Berlin Heidelberg: Springer, 2003, pp. 445-516.

[39] V. Girard, R. Farrenq, E. Sorokin, I. T. Sorokina, G. Guelachvili, and N. Picque, "Acetylene weak bands at 2.5 μm from intracavity Cr^{2+}:ZnSe laser absorption observed with time-resolved Fourier transform spectroscopy," *Chemical Physics Letters*, vol. 419, pp. 584-588, 2006.

[40] V. A. Akimov, M. P. Frolov, Y. V. Korostelin, V. I. Kozlovsky, A. I. Landman, and Y. P. podmar'kov, "Cr^{2+}:ZnSe laser for application to intracavity laser spectroscopy," presented at Laser Optics 2003: Solid State Lasers and Nonlinear Frequency Conversion, 2003.

[41] E. Sorokin and I. T. Sorokina, "Mid-IR high-resolution intracavity Cr^{2+}:ZnSe laser based spectrometer," presented at Advanced Solid State Photonics, Vienna, Austria, 2005.

[42] M. Raybaut, A. Godard, R. Haidar, M. Lefebvre, P. Kupecek, P. Lemasson, and E. Rosencher, "Generation of mid-infrared radiation by self difference frequency mixing in chromium-doped zinc selenide," *Optics Letters*, vol. 31, pp. 220-222, 2006.

[43] A. Zakel, G. J. Wagner, W. J. Alford, and T. J. Carrig, "High-power, rapidly tunable dual-band CdSe optical parametric oscillator," presented at Advanced Solid-State Photonics, Vienna, Austria, 2005.

[44] I. T. Sorokina, "Crystalline Mid-Infrared Lasers," in *Solid-State Mid-Infrared Laser Sources*, vol. 89, *Springer Topics in Applied Physics*, I. T. Sorokina and K. L. Vodopyanov, Eds. Berlin Heidelberg: Springer, 2003, pp. 255-349.

[45] A. Sennaroglu, "Broadly tunable Cr^{4+} -doped solid-state lasers in the near infrared and visible," *Progress in Quantum Electronics*, vol. 26, pp. 287-352, 2002.

[46] A. A. Kaminskii, "Modern Developments in the physics of crystalline laser materials," *Phys. Stat. Sol.*, vol. 200, pp. 215-296, 2003.

[47] S. Kück, "Laser-related spectroscopy of ion-doped crystals for tunable solid-state lasers," *Applied Physics B*, vol. 72, pp. 515-562, 2001.

[48] P. F. Moulton, "Tunable solid-state lasers," *Proceedings of the IEEE*, vol. 80, pp. 348-364, 1992.

[49] J. C. Walling, O. G. Peterson, H. P. Jenssen, R. C. Morris, and E. W. O`Dell, "Tunable alexandrite lasers," *IEE Journal of Quantum Electronics*, vol. 16, pp. 1302-1315, 1980.

[50] J. C. Walling, D. F. Heller, H. Samelson, D. J. Harter, J. A. Pete, and R. C. Morris, "Tunable alexandrite lasers:development and performance," *IEE Journal of Quantum Electronics*, vol. QE-21, pp. 1568-1581, 1985.

[51] P. F. Moulton, "Spectroscopic and laser characteristics of Ti:Al_2O_3," *JOSA B*, vol. 3, pp. 125-133, 1986.

[52] V. G. Baryshevskii, M. V. Korzhik, A. E. Kimaev, M. G. Livshits, V. B. Pavlenko, M. L. Meil'man, and B. I. Minkov, "Tunable chromium forsterite laser in the near IR region," *Journal of Applied Spectroscopy (USSR)*, vol. 53, pp. 675-676, 1990.

[53] S. Kuck, K. Petermann, U. Pohlmann, U. Schonhoff, and G. Huber, "Tunable room-temperature laser action of a Cr-4^{+}-doped $Y_3Sc_xAl_5$-$_xO_{12}$," *Applied Physics B*, vol. 58, pp. 153-156, 1994.

[54] D. Welford and P. F. Moulton, "Room-temperature operation of a Co:MgF_2 laser," *Optics Letters*, vol. 13, pp. 975-977, 1988.

[55] J. Kernal, V. V. Fedorov, A. Gallian, S. B. Mirov, and V. V. Badikov, "3.9-4.8 μm gain-switched lasing of Fe:ZnSe at room temperature," *Optics Express*, vol. 13, pp. 10608-10615, 2005.

[56] I. T. Sorokina, E. Sorokin, S. Mirov, V. Fedorov, V. Badikov, V. Panyutin, and K. I.Schaffers, "Broadly tunable compact continuous-wave Cr^{2+}:ZnS laser," *Optics Letters*, vol. 27, pp. 1040-1042, 2002.

[57] T. H. Maiman, "Stimulated optical radiation in ruby," *Nature*, vol. 187, pp. 493-494, 1960.

[58] L. F. Johnson, R. E. Dietz, and H. J. Guggenheim, "Optical maser oscillation from Ni^{2+} in MgF_2 involving simultaneous emission of phonons," *Physical Review Letters*, vol. 11, pp. 318-320, 1963.

[59] L. F. Johnson, H. J. Guggenhem, and R. A. Thomas, "Phonon-terminated optical masers," *Physical Rev.*, vol. 149, pp. 179-185, 1966.

[60] L. F. Johnson, R. E. Dietz, and H. J. Guggenheim, "Spontaneous and stimulated emission from Co^{2+} ions in MgF_2 and ZnF_2," *Applied Physics Letters*, vol. 5, pp. 21-23, 1964.

[61] L. F. Johnson and H. J. Guggenheim, "Phonon-terminated coherent emission from V^{2+} ions in MgF_2," *Journal of Applied Physics*, vol. 38, pp. 4837-4839, 1967.

[62] D. E. McCumber, "Theory of phonon-terminated optical masers," *Physical Rev.*, vol. 134, pp. A299-A306, 1963.

[63] D. E. McCumber, "Theory of vibrational structure in optical spectra of impurities in solids. I. Singlets," *Journal of Mathematical Physics*, vol. 5, pp. 221-230, 1963.

[64] D. E. McCumber, "Theory of vibrational structure in optical spectra of impurities in solids. II. multiplets," *Journal of Mathematical Physics*, vol. 5, pp. 508-521, 1963.

[65] D. E. McCumber, "Einstein relations connecting broadband emission and absorption spectra," *Physical Rev.*, vol. 136, pp. A954-A957, 1964.

[66] P. F. Moulton, A. Mooradian, and T. B. Reed, "Efficient cw optically pumped Ni:MgF2 laser," *Optics Letters*, vol. 3, 1978.

[67] J. C. Walling, H. P. Jenssen, R. C. Morris, E. W. O'Dell, and O. G. Peterson, "Tunable-laser performance in BeAl2O:Cr3+," *Optics Letters*, vol. 4, 1979.

[68] P. Zeller and P. Peuser, "Efficient, multiwatt, continuous-wave laser operation on the $^4F_{3/2}$-$^4I_{9/2}$ tarnsitions of Nd:YVO_4 and Nd:YAG," *Optics Letters*, vol. 25, pp. 34-36, 2000.

[69] B. Struve, G. Huber, V. V. Laptev, I. A. Scherbakov, and E. V. Zharikov, "Tunable room-temperature cw laser action in Cr^{3+}:GdScGa-Garnet," *Applied Physics B*, vol. 30, pp. 117-120, 1983.

[70] J. Drube, B. Struve, and G. Huber, "Tunable room-temperature cw laser action in Cr^{3+}:GdScAl-Garnet," *Optic Communications*, vol. 50, pp. 45-48, 1984.

[71] S. A. Payne, L. L. Chase, H. W. Newkirk, L. K. Smith, and W. F. Krupke, "$LiCaAlF_6$:Cr^{3+}: A Promising New Solid-State Laser Material," *IEEE JOURNAL OF QUANTUM ELECTRONICS*, vol. 24, pp. 2243-2252, 1988.

[72] S. A. Payne, L. L. Chase, L. K. Smith, W. L. Kway, and H. W. Newkirk, "Laser performance of $LiSAlF_6$:Cr^{3+}," *Journal of Applied Physics*, vol. 66, pp. 1051-1056, 1989.

[73] J. J. Adams, C. Bibeau, R. H. Page, D. M. Krol, L. H. Furu, and S. A. Payne, "4.0-4.5 μm lasing of Fe: ZnSe below 180 K, a new mid-infrared laser material," *Optics Letters*, vol. 24, pp. 1720-1722, 1999.

[74] J. Kernal, V. V. Fedorov, A. Gallian, S. B. Mirov, and V. V. Badikov, "Room temperature 3.9-4.5 μm gain-switched lasing of Fe:ZnSe," presented at Advanced Solid State Photonics, Nevada, 2006.

[75] A. A. Voronov, V. I. Kozlovskii, Y. V. Korostelin, A. I. Landman, Y. P. Podmar'kov, and M. P. Frolov, "Laser parameters of a Fe:ZnSe crystal in the 85-255-K temperature range," *Quantum Electronics*, vol. 35, pp. 809-812, 2005.

[76] V. A. Akimov, A. A. Voronov, V. I. Kozlovsky, Y. V. Korostelin, A. I. Landman, Y. P. Podmar'kov, and M. P. Frolov, "Efficient IR Fe:ZnSe laser continuously tunable in the spectral range from 3.77 to 4.40 μm," *Quantum Electronics*, vol. 34, pp. 912-914, 2004.

[77] J. J. Adams, C. Bibeau, R. H. Page, and S. A. Payne, "Tunable laser action at 4.0 microns from Fe:ZnSe," presented at Advanced Solid State Lasers, Boston, 1999.

[78] A. A. Voronov, V. I. Kozlovskii, Y. V. Korostelin, A. I. Landman, Y. P. Podmar'kov, V. G. Polushkin, and M. P. Frolov, "Passive Fe^{2+}:ZnSe single-crystal Q switch for 3-μm lasers," *Quantum Electronics*, vol. 36, pp. 1-2, 2006.

[79] V. A. Akimov, A. A. Voronov, V. I. Kozlovsky, Y. V. Korostelin, A. I. Landman, Y. P. Podmar'kov, and M. P. Frolov, "Efficient lasing in a Fe^{2+}:ZnSe crystal at room temperature," *Quantum Electronics*, vol. 36, pp. 299-301, 2006.

[80] C.-H. Su, S. Feth, M. P. Volz, R. Matyi, M. A. George, K. Chattopadhyay, A. Burger, and S. L. Lehoczky, "Vapor growth and characterization of Cr-doped ZnSe crystals," *Journal of Crystal Growth*, vol. 207, pp. 35-42, 1999.

[81] A. Burger, K. Chattopadhyay, J. O. Ndap, X. Ma, S. H. Morgan, C. I. Rablau, C. H. Su, S. Feth, R. H. Page, K. I. Schaffers, and S. A. Payne, "Preparation conditions of chromium doped ZnSe and their infrared luminescence properties," *Crystal Growth*, vol. 225, pp. 249-256, 2001.

[82] S. B. Mirov, S. Wang, V. V. Fedorov, and R. P. Camata, "Pulse laser deposition growth and spectroscopic properties of chromium doped ZnS crystalline thin films," presented at Advanced Solid State Photonics, Santa Fe, NM, 2004.

[83] B. L. Vanmil, A. J. Ptak, L. Bai, L. Wang, M. Chirila, N. C. Giles, T. H. Myers, and L. Wang, "Heavy Cr doping of ZnSe by molecular beam epitaxy," *Journal of Electronic Materials*, vol. 31, pp. 770-775, 2002.

[84] J.-O. Ndap, O. O. Adetunji, K. Chattopadhyay, C. I. Rablau, S. U. Egarievwe, X. Ma, S. Morgan, and A. Burger, "High-temperature solution growth of Cr^{2+}:CdSe for tunable mid-IR laser application," *Journal of Crystal Growth*, vol. 211, pp. 290-294, 2000.

[85] J. O. Ndap, K. Chattopadhyay, O. O. Adetunji, D. E. Zelmon, and A. Burger, "Thermal diffusion of Cr^{2+} in bulk ZnSe," *Journal of Crystal Growth*, vol. 240, pp. 176-184, 2002.

[86] C. I. Rablau, J. O. Ndap, X. Ma, A. Burger, and N. C. Giles, "Absorption and Photoluminescence Spectroscopy of Diffusion-Doped ZnSe:Cr^{2+}," *Electronic Materials*, vol. 28, pp. 678-682, 1999.

[87] U. N. Roy, O. S. Babalola, J. Jones, Y. Cui, T. Mounts, A. Zavalin, S. Morgan, and A. Burger, "Uniform Cr^{2+} doping of physical vapor transport grown CdS_xSe_{1-x} crystals," *Journal of Electronic Materials*, vol. 34, pp. 19-22, 2005.

[88] S. B. Mirov, V.V.Fedorov, K. Graham, I. S. Moskalev, I. T. Sorokina, E. Sorokin, V. Gapontsev, D. Gapontsev, V. V. Badikov, and V. Panyutin, "Diode and fibre pumped

Cr^{+2}:ZnS mid-infrared external cavity and microchip lasers," *IEE Proc. Optoelectron.*, vol. 150, pp. 340-345, 2003.

[89] M. B. Johnson, S. B. Mirov, V. Fedorov, M. E. Zvanut, J. G. Harrison, V. V. Badikov, and G. S. Shevirdyaeva, "Absorption and photoluminescence studies of $CdGa_2S_4$:Cr," *Optic Communications*, vol. 233, pp. 403-410, 2004.

[90] V. R. Davis, X. Wu, U. Hommerich, K. Grasza, S. B. Trivedi, and Z. Yu, "Optical properties of Cr^{2+} ions in $Cd_{085}Mn_{0.15}Te$," *Journal of Luminescence*, vol. 72, pp. 281-283, 1997.

[91] U. N. Roy, O. S. Babalola, Y. Cui, M. Groza, T. Mounts, A. Zavalin, S. Morgan, and A. Burger, "Vapor growth and chracterization of Cr-doped $CdS_{0.8}Se_{0.2}$ single crystals," *Journal of Crystal Growth*, vol. 265, pp. 453-458, 2004.

[92] V. A. Akimov, M. P. Frolov, Y. V. Korostelin, V. I. Kozlovsky, A. I. Landman, Y. P. Podmar'kov, and A. A. Voronov, "Vapour growth of II-VI single crystals doped by transition metals for mid-infrared lasers," *Physica Status Solidi (c)*, vol. 3, pp. 1213-1216, 2006.

[93] K. L. Schepler, S. Kück, and L. Shiozawa, "Cr^{2+} emission spectroscopy in CdSe," *Luminescence*, pp. 116-117, 1997.

[94] V. Kasiyan, Z. Dashevsky, R. Shneck, and E. Towe, "Optical and transport properties of chromium-doped CdSe and $CdS_{0.67}Se_{0.33}$ crystals," *Journal of Crystal Growth*, vol. 290, pp. 50-55, 2006.

[95] U. N. Roy, Y. Cui, C. Barnett, K.-T. Chen, A. Burger, and J. T. Goldstein, "Growth of undoped and chromium-doped CdS_xSe_{1-x} crystals by the physical vapor transport method," *Journal of Electronic Materials*, vol. 31, pp. 791-794, 2002.

[96] I. T. Sorokina, E. Sorokin, S. Mirov, V. Fedorov, V. Badikov, V. Panyutin, A. D. Lieto, and M. Tonelli, "Tunable continuous-wave room temperature Cr^{2+}:ZnS laser," presented at Advanced Solid State Photonics, Quebe, 2002.

[97] K. Graham, S. B. Mirov, V. V. Fedorov, M. E. Zvanut, A. Avanesov, V. Badikov, B. Ignat'ev, V. Panutin, and G. Shevirdyaeva, "Spectroscopic chracterization and laser

performance of diffusion doped Cr^{2+}:ZnS," presented at Advanced Solid State Photonics, San Jose, 2001.

[98] Y. G. Sadofyev, V. F. Pevtsov, E. M. Dianov, P. A. Trubenko, and M. V. Korshkov, "Molecular beam epitaxy growth and characterization of ZnTe:Cr^{2+} layers on GaAs(100)," *J. Vac. Sci. Technol. B*, vol. 19, pp. 1483-1487, 2001.

[99] U. Demirbas, A. Sennaroglu, A. Kurt, and M. Somer, "Preparation and spectroscopic investigation of diffusion-doped Fe^{2+}:ZnSe and Cr^{2+}:ZnSe," presented at Advanced Solid-State Photonics, Vienna, Austria, 2005.

[100] G. J. Wagner, T. J. Carrig, R. H. Jarman, R. H. Page, K. I. Schaffers, J.-O. Ndap, X. Ma, and A. Burger, "High-efficiency, broadly-tunable continuous-wave Cr^{2+}:ZnSe laser," presented at Advanced Solid State Photonics, Boston, 1999.

[101] E. Sorokin and I. T. Sorokina, "Mode-locked ceramic Cr^{2+}:ZnSe laser," presented at Advanced Solid-State Photonics, San Antonio, 2003.

[102] T. J. Carrig, "Transition-Metal-Doped Chalcogenide Lasers," *Journal of Electronic Materials*, vol. 31, pp. 759-769, 2002.

[103] V. I. Levchenko, V. N. Yakimovich, L. I. Postnova, V. I. Konstantinov, V. P. Mikhailov, and N. V. Kuleshov, "Preparation and properties of bulk ZnSe:Cr single crystals," *Crystal Growth*, vol. 198, pp. 980-983, 1999.

[104] U. Demirbas, A. Sennaroglu, and M. Somer, "Sythesis and characterization of diffusion-doped Cr^{2+}:ZnSe and Fe^{2+}:ZnSe," *Optical Materials*, vol. 28, pp. 231-240, 2006.

[105] U. Hömmerich, A. G. Bluiett, I. K. Jones, S. B. Trivedi, and R. T. Shah, "Crystal growth and infrared spectroscopy of Cr:$Cd_{1-x}Zn_xTe$ and Cr:$Cd_{1-x}Mg_xTe$," *Journal of Crystal Growth*, vol. 287, pp. 243-247, 2006.

[106] Crystran, http://www.crystran.co.uk/index.asp, consulted in: January 11, 2006.

[107] Carbolite firm web page, http://www.carbolite.com/index.asp, consulted in: January, 09, 2006.

[108] H. S. Carslaw and J. C. Jaeger, *Conduction of Heat in Solids*. Oxford: Oxford Science, 1959.

[109] Shimadzu UV-3101PC UV-VIS-NIR spectrophotometer, http://www.ssi.shimadzu.com/products/spectro/uv3101.pdf, consulted in: January 11, 2006.

[110] Y. P. V. Subbaiah, P. Prathap, M. Devika, and K. T. R. Reddy, "Close-spaced evaporated ZnSe films: Preparation and chracterization," *Physica B*, vol. 365, pp. 240-246, 2005.

[111] G. J. Hawkins, "Spectral characterization of infrared optical materials and filters," in *Department of Cybernetics*: The University of Reading, 1998, pp. 173.

[112] G. Goetz, H. Zimmermann, and H.-J. Schulz, "Jahn-Teller interaction at $Cr^{2+}(d^4)$ centers in tetrahedrally coordinated II-VI lattices studied by optical spectroscopy," *Zeitschrift Für Physik B*, vol. 91, pp. 429-236, 1993.

[113] M. Godlewski and M. Kaminska, "The chromium impurity photogeneration transitions in ZnS, ZnSe and ZnTe," *Journal of Physics C: Solid State Physics*, vol. 13, pp. 6537-6545, 1980.

[114] S. Bhaskar, P. S. Dobal, B. K. Rai, R. S. Katiyar, H. D. Bist, J.-O. Ndap, and A. Burger, "Photoluminescence study of deep levels in Cr-doped ZnSe," *Applied Physics*, vol. 85, pp. 439-443, 1998.

[115] M. Godlewski, "Mechanisms of radiative and nonradiative recombination in ZnSe:Cr and ZnSe:Fe," *Low Temperature Physics*, vol. 30, pp. 891-896, 2004.

[116] I. T. Sorokina, E. Sorokin, A. D. Lieto, M. Tonelli, R. H. Page, and K. I. Schaffers, "Efficient broadly tunable continuous-wave Cr^{2+}:ZnSe laser," *Journal of the Optical Society of America B*, vol. 18, pp. 926-930, 2001.

[117] G. F. Neumark, "Defects in wide band gap II-VI crystals," *Materials Science and Engineering*, vol. R21, pp. 1-46, 1997.

[118] V. Y. Ivanov, M. Godlewski, A. Szczerbakow, A. Omel'chuk, A. Davydov, N. Zhavoronkov, and G. Raciukaitis, "Optically pumped mid-infrared stimulated emission of ZnSe:Cr crystals," *Acta Physica Polonica A*, vol. 105, pp. 553-558, 2004.

[119] A. V. Podlipensky, V. G. Shcherbitsky, N. V. Kuleshov, V. I. Levchenko, V. N. Yakimovich, M. Mond, E. Heumann, G. Huber, H. Kretschmann, and S. Kück, "Efficient laser operation and continuous-wave didode pumping of Cr^{2+}:ZnSe single crystals," *Applied Physics B*, pp. 253-255, 2001.

[120] Y. F. Vaksman, V. V. Pavlov, Y. A. Nitsuk, Y. N. Purtov, A. S. Nasibov, and P. V. Shapkin, "Optical Absorption and Chromium Diffusion in ZnSe Single Crystals," *Semiconductors*, vol. 39, pp. 377-380, 2005.

[121] A. Gallian, V. V. Fedorov, J. Kernal, S. B. Mirov, and V. V. Badikov, "Laser oscillation at 2.4 μm from Cr^{2+} in ZnSe optically pumped over Cr ionization transitions," presented at Advanced Solid State Photonics, Austria, 2005.

[122] K. Graham, V. V. Fedorov, S. B. Mirov, M. E. Doroshenko, T. T. Basiev, Y. V. Orlovskii, V. V. Osiko, V. V. Badikov, and V. L. Panyutin, "Pulsed mid-IR Cr^{2+}:ZnS and Cr^{2+}:ZnSe lasers pumped by Raman-shifted Q-switched neodymium lasers," *Quantum Electronics*, vol. 34, pp. 8-14, 2004.

[123] A. Sennaroglu, U. Demirbas, A. Kurt, and M. Somer, "Concentration dependence of fluorescence and lasing efficiency in Cr2+:ZnSe lasers," *Optical Materials*, 2006 in press.

[124] V. E. Kisel, V. G. Shcherbitsky, N. V. Kuleshov, V. I. Konstantinov, V. I. Levchenko, E. Sorokin, and I. T. Sorokina, "Spectral kinetic properties and lasing chracteristics of diode-pumped Cr^{2+}:ZnSe single crystals," *Optics and Spectroscopy*, vol. 99, pp. 663-667, 2005.

[125] A. V. Podlipensky, V. G. Shcherbitsky, N. V. Kuleshov, V. P. Mikhailov, V.I.Levchenko, V. N. Yakimovich, L.I.Postnova, and V.I.Konstantinov, "Pulsed laser operation of diffusion-doped Cr^{2+}:ZnSe," *Optics Communications*, vol. 167, pp. 129-132, 1999.

[126] A. V. Podlipensky, Shcherbitsky, V. G., Kuleshov, N. V., Levchenko, V. I., Yakimovich, V. N., Mond, M., Heumann, E., Huber, G., Kretschmann, H., Kück, S., "Efficient laser operation and continuous-wave didode pumping of Cr^{2+}:ZnSe single crystals," *Applied Physics B*, pp. 253-255, 2000.

[127] S. B. Mirov, V.V.Fedorov, K. Graham, I. S. Moskalev, V.V.Badikov, and V.Panyutin, "Erbium fiber laser-pumped continuous-wave microchip Cr^{2+}:ZnS and Cr^{2+}:ZnSe lasers," *Optics Letters*, vol. 27, pp. 909-911, 2002.

[128] B. Henderson and G. F. Imbush, *Optical spectroscopy of inorganic solids*. Oxford: Clarendon Press, 1989.

[129] R. C. Powell, *Physics of solid-state laser materials*. New York: Springer-Verlag, 1998.

[130] V. E. Kisel, V. G. Shcherbitsky, N. V. Kuleshov, V. I. Konstantinov, L. I. Postnova, L. I. Levchenko, E. Sorokin, and I. T. Sorokina, "Emission lifetime measurements and laser performance of Cr:ZnSe under diode pumping at 1770 nm," presented at Advanced Solid-State Photonics, Santa Fe, New Mexico, USA, 2004.

[131] U. Hömmerich, I. K. Jones, E. E. Nyein, and S. B. Trivedi, "Comparison of the optical properties of diffusion-doped polycrystalline Cr:ZnSe and Cr:CdTe windows," *Journal of Crystal Growth*, vol. 287, pp. 450-453, 2006.

[132] A. Sennaroglu, U. Demirbas, S. Ozharar, and F. Yaman, "Accurate determination of saturation parameters for Cr^{4+}-doped solid-state saturable absorbers," *Journal of Optical Society of America B*, vol. 23, pp. 241, 2006.

[133] A. V. Podlipensky, Shcherbitsky, V.G., Kuleshov, N.V., Mikhailov, V.P., "Cr^{2+}:ZnSe and Co^{2+}:ZnSe saturable-absorber Q switches for 1.54-μm Er:glass lasers," *Optics Letters*, vol. 24, pp. 960-962, 1999.

[134] V. G. Shcherbitsky, S. Girard, M. Fromager, R. Moncorge, N. V. Kuleshov, V. I. Levchenko, V. N. Yakimovich, and B. Ferrand, "Accurate method of the measurement of absorptioncross sections of solid-state saturable absorbers," *Applied Physics B*, vol. 74, pp. 367-374, 2002.

[135] R. D. Stultz, V. Leyva, and K. Spariosu, "Short pulse, high-repetition rate, passively q-switched Er:yttrium-aluminum-garnet laser at 1.6 microns," *Applied Physics Letters*, vol. 87, pp. 241118, 2005.

[136] T.-Y. Tsai and M. Birnbaum, "Q -Switched 2- μm lasers by use of a Cr^{2+}:ZnSe saturable absorber," *Applied Optics*, vol. 40, pp. 6633-6637, 2001.

[137] F. Z. Qumar and T. A. King, "Passive q-switching of Tm-silica fibre laser near 2 μm by a Cr^{2+}:ZnSe saturable absorber crystal," *Optics Communications*, vol. 248, pp. 501-508, 2005.

[138] M. P. Frolov, Y. V. Korostelin, V. I. Kozlovsky, A. I. Landman, and Y. P. Podmar'kov, "Efficient laser operation from Cr^{2+}:ZnSe crystals produced by seeded physical vapor transport method," presented at Lasser Optics 2003: Solid State Lasers and Monlinear Frequency Conversion, 2003.

[139] V. I. Kozlovsky, Y. V. Korostelin, A. I. Landman, Y. P. Podmar'kov, and M. P. Frolov, "Efficient lasing of a Cr^{2+}:ZnSe crystal grown from a vapour phase," *Quantum Electronics*, vol. 33, pp. 408-410, 2003.

[140] W. J. Alford, G. J. Wagner, A. C. Sullivan, J. A. Keene, and T. J. Carrig, "High-Power and Q-Switched Cr:ZnSe Lasers," *OSA TOPS, Advanced Solid-State Photonics*, vol. 83, pp. 13-17, 2003.

[141] A. Zakel, G. J. Wagner, A. C. Sullivan, J. F. Wenzel, W. J. Alford, and T. J. Carrig, "High-brightess, rapidly tunable Cr:ZnSe lasers," presented at Advanced Solid State Photonics, Vienna, Austria, 2005.

[142] J. A. Caird, L. G. DeShazer, and J. Nella, "Characteristics of Room-Temperature 2.3-μm Laser Emission from Tm^{3+} in YAG and $YAlO_3$," *IEEE Journal of Quantum Electronics*, vol. QE-11, pp. 874-881, 1975.

[143] E. Sorokin and I. T. Sorokina, "Tunable diode-pumped continuous-wave Cr^{+2}:ZnSe laser," *Applied Physics Letters*, vol. 80, pp. 3289-3291, 2002.

[144] W. Koechner, *Solid-State Laser Engineering*, vol. 1, 4 ed. New York: Springer, 1996.

[145] K. L. Schepler, R. D. Peterson, P. A. Berry, and J. B. McKay, "Thermal effects in Cr^{2+}:ZnSe thin disk lasers," *IEEE Journal of Selected Topics in Quantum Electronics*, vol. 11, pp. 713-720, 2005.

[146] A. D. Lieto and M.Tonelli, "Development of a cw polycrystalline Cr^{2+}:ZnSe laser," *Optics and Lasers in Engineering*, vol. 39, pp. 305-308, 2001.

[147] A. Sennaroglu, A. O. Konca, and C. R. Pollock, "Continuous-Wave Power Performance of a 2.47 μm Cr^{2+}: ZnSe Laser: Experiment and Modeling," *IEEE Journal of Quantum Electronics*, vol. 36, pp. 1199-1205, 2000.

[148] M. Mond, D. Albrecht, H. M. Kretschmann, E. Heumann, G. Huber, S. Kück, V. I. Yakimovich, V. G. Shcherbitsky, V. E. Kisel, and N. V. Kuleshov, "Erbium Doped Fibre Amplifier Pumped Cr^{2+}:ZnSe Laser," *Phys. Stat. Sol.*, vol. 188, 2001.

[149] I. S. Moskalev, V. V. Fedorov, and S. B. Mirov, "Multiwavelength mid-IR spatially-dispersive CW laser based on polycrystalline Cr^{2+}:ZnSe," *Optics Express*, vol. 12, pp. 4986-4992, 2004.

[150] R. D. Peterson and K. L. Schepler, "1.9 μm-fiber-pumped Cr:ZnSe Laser," presented at Advanced Solid-State Photonics, Vienna, Austria, 2005.

[151] P. F. Moulton, "An Investigation of the Co:MgF_2 Laser System," *IEEE Journal of Quantum Electronics*, vol. 21, pp. 1582-1595, 1985.

[152] L. L. Gordley, B. T. Marshall, and D. A. Chu, "LINEPAK: Alogorithms for modeling spectral transmittance and radiance," *J. Quant. Spectrosc. Radiat. Transfer*, vol. 52, pp. 563-580, 1994.

[153] A. Sennaroglu, "Continuous-wave thermal loading in saturable absorbers: theory and experiment," *Applied Optics*, vol. 36, pp. 9528-9535, 1997.

[154] A. Sennaroglu, "Analysis and optimization of lifetime thermal loading in continuous-wave Cr^{4+}-doped solid-state lasers," *Journal of Optical Society of America B*, vol. 18, pp. 1578-1586, 2001.

[155] A. Sennaroglu, "Effect of thermal lensing on the mode mathcing between pump and laser beams in Cr^{4+}:forsterite lasers: a numerical study," *Journal of Physics D: Applied Physics*, vol. 33, pp. 1478-1483, 2000.